COMPUTER SIMULATIONS OF Li-Mn-O LAYERED-SPINEL COMPOSITE NANOARCHITECTURES.

A dissertation presented

By

HLUNGWANI DONALD

To

The Department of Physics

In fulfilment of the requirements for the degree of

Master of Science

In the subject of

Physics

Faculty of Science and Agriculture

School of Physical and Mineral Sciences

University of Limpopo (Turfloop campus)

South Africa

Supervisor: Prof. P.E. Ngoepe

Co-supervisor: Dr. R.S. Ledwaba

December 2020

Declaration

I declare that the thesis hereby submitted to the University of Limpopo for the degree of Masters has not been previously submitted by me for a degree at this or any other university, that it is my own work both in design and execution, and that all materials contained herein have been duly acknowledged.

Mr D. Hlungwani

Signature: 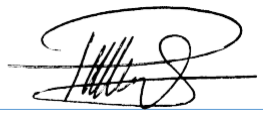

Student Number: 201428754 Date 24/11/2020

Dedication

This work is dedicated to

My supportive mother

Florah Chabangu

My supportive father

Freddy Hlungwani

My late sister

Evah Hlungwani

My brothers

Bongani Hlungwani
Dzunisani Hlungwani

My younger sisters

Nkateko Hlungwani
Tinyiko Hlungwani

Acknowledgements

First and foremost I would like to thank God for His Mercy and Grace. I am where I am today because of him. I would like to express my sincere gratitude to my supervisor Prof P.E Ngoepe for affording me an opportunity to work on this riveting and cutting-edge research project and also for his continual support and exposure to different research techniques. I would also like to thank my co-supervisor Dr R.S Ledwaba for her guidance, patience, support and inspiration throughout this research project. She patiently taught me essential research techniques which enabled me to successfully carry out this project. I also thank my family for their support, love and understanding. I would like to also thank our research group, Materials Modelling Center (MMC) for research tools and support. I also thank Mr K.W Phoshoko and Mr K Kgatwane for their technical support. I would also like to thank the university, particularly the physics department for allowing me to register my Master's degree. I also like to extend my sincere gratitude to NRF for financial support.

Abstract

Layered-spinel composite electrodes are among the promising cathode materials for advancing lithium-ion batteries due to the reported synergistic effect, which contributes to improvement of their electrochemical performance. A vast number of studies have focused on strategies to enhance the specific capacity of layered-spinel composite cathode materials. However, limited efforts have been put into understanding the impact of structural changes incurred by the material during the discharge process. Consequently, this work is aimed at studying the discharge process of a lithium-ion battery utilising, particularly the nanoarchitectured composite Li-Mn-O layered-spinel cathode material using the simulated synthesis technique. The structural changes (electronic level and atomic level) affecting electrochemical performance as the discharge process proceeds are captured.

The electronic structure of the magnetic and non-magnetic Mn_2O_4, $LiMn_2O_4$ and $Li_2Mn_2O_4$ have been investigated. For the electronic level, the discharge process was depicted by the Mn_2O_4, $LiMn_2O_4$ and $Li_2Mn_2O_4$ spinel structures and structural changes were analysed through electronic band structures and density of states. The amorphisation and recrystallisation technique was also performed to enable the atomic-level structural analysis. Consequently, Li-Mn-O layered-spinel composite nanoarchitectures depicting different stages of the discharge process in question were generated. From the calculated density of states and electronic band structures, all the non-magnetic structures show metallic behaviour with the filling of the conduction band increasing with lithiation. The electronic structure of the magnetic Mn_2O_4 spinel structure exhibits semiconducting properties which are in line with literature. The electronic band structures and density of states (DOS) of the magnetic $LiMn_2O_4$ and lithiated-$Li_2Mn_2O_4$ reveal metallic behaviour with the Fermi level mainly comprising of spin-down states.

The discharge process was simulated by performing a chemical lithiation on the $LiMn_2O_4$ amorphous spinel structure succeeding the amorphisation process. The simulated recrystallisation was then performed on the lithiated amorphous $Li_xMn_2O_4$ spinel structures, where $1 \leq x \leq 2$. The recrystallisation process yielded multigrain

nanospheres constituting Li-Mn-O layered and spinel components confirmed by atomic structural snapshots and X-ray Diffraction (XRD) Patterns. The amorphous and crystalline states of these systems were verified by Radial Distribution Functions (RDFs) and XRD patterns. The spontaneous recrystallisation process was illustrated by configuration energy graphs indicating nucleation and crystal growth stages as the process progresses. Configuration energy graphs show that an increase in lithium content favour's the nucleation process resulting in less amount of time required for crystal growth. XRD patterns showed Mn_3O_4, $LiMn_2O_4$, and Li_2MnO_3 characteristic peaks revealing the co-existence of these components in the simulated nanoarchitectures. The Mn_3O_4 component decreases with lithium concentration and an increase in lithium concentration favour's the formation of spinel $LiMn_2O_4$ and layered Li_2MnO_3 phases. A number of crystallographic vacancy defects are observed at lower lithium concentrations and they decrease with lithiation. Suggesting that lithium atoms are occupying these sites as the discharge process progresses. Clear lithium diffusion channels are noted as the discharge process proceeds which is evinced by an increase in crystallinity with lithiation.

Table of Contents

List of tables

List of figures

CHAPTER 1

Introduction and background

Arising global environmental issues stemming from a generation of energy from non-renewable environment polluting sources have rooted more research for finding benign energy generation solutions [1, 2, 3]. Large scale systems such as electric vehicles require that the current energy storage systems be improved to increase the impact of renewable energy. To date, rechargeable lithium-ion batteries have emerged as the most promising rechargeable batteries owing to their high energy density. They have been successful in their wide range of applications especially in portable electronics [4, 5, 6, 7].

The performance of energy storage systems relies on the properties of the underlying electrode materials. To cater for the exponential technology growth together with the increasing dependency on portable electronic devices, a thorough investigation on such properties is imperative. Furthermore, the use of abundant electrode materials (lithium-manganese-oxide) could reduce the cost factor hindering the prosperity of electric vehicles and therein decreasing the emissions of CO_2 from the traditional combustion engines. As such, energy storage systems can play a vital role in addressing global environmental issues. However, its full impact requires the development of safe, durable, inexpensive, lightweight and high energy batteries [8, 9].

1.1 Evolution of lithium-ion batteries

Secondary lithium-ion batteries have gained more attention in various areas since they were commercialised in 1991 [10, 11]. Recently, due to their high energy density, they are spanning different application fields including the emerging field of hybrid electric vehicles or electric vehicles. Moreover, Tesla is the leading manufacturer of electric vehicle thus far owing to the success of lithium-ion batteries [12, 13, 14]. Key components that make up a rechargeable or secondary lithium-ion battery are cathode (positive electrode), electrolyte and anode (negative electrode). The two electrodes separated from each other by a polymer membrane are dipped into an electrolyte. This

setup allows for a converse movement of electrons and ions in the system resulting in a production of electrical energy that we use to power our devices [4].

1.1.1 Anatomy of a lithium-ion battery

A conventional lithium-ion battery configuration is shown in figure 1.1 below depicting its operation. The positive electrode traditionally consists of a lithium metal oxide [15, 16] whilst the negative electrode is traditionally made up of graphite [17, 18, 19] both immersed in a lithium salt solution such as lithium hexafluorophosphate (LiPF6) [20]. The two electrodes are separated by a porous membrane which allows lithium-ions to pass through from the cathode to the anode vice versa. As depicted in figure 1.1 below, during a discharge process, a spontaneous reaction takes place in which lithium-ions and electrons in the graphene layers (anode) move through the electrolyte and external circuit, respectively in to the cathode. For a charge process, an external voltage to enable lithium-ions and electrons to move from the cathode to the anode is applied between the two electrodes. The electrons move through the external circuit whilst the lithium-ions move through the electrolyte. The flow of electrons through the electrolyte is hindered by a porous membrane which only allows the flow of lithium-ions as shown in figure [4, 21, 22].

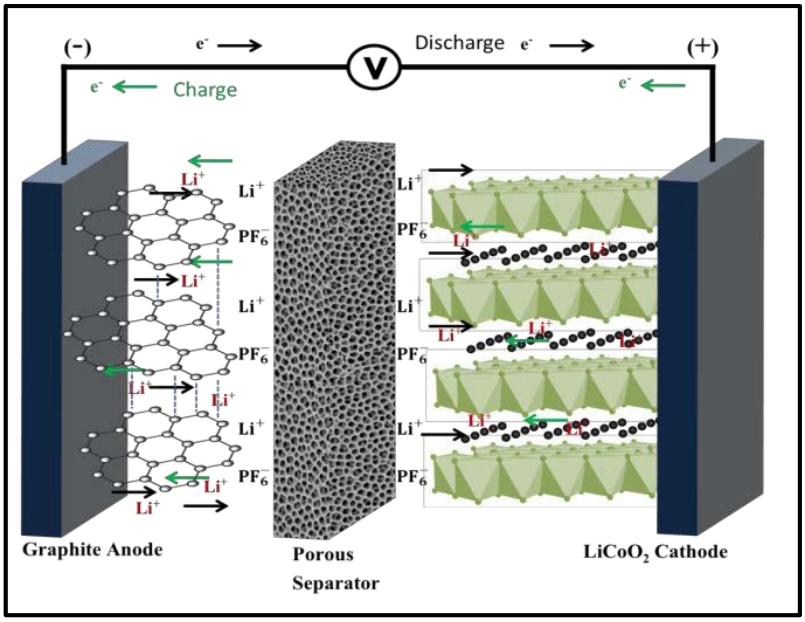

Figure 1. 1: Schematic representation illustrating the operation of a secondary lithium-ion battery. During a charging process lithium-ions move from the graphite anode through the porous membrane into the cathode and the reverse process occurs during a charge process.

1.1.2 Applications

The fact that lithium-ion batteries are light and the electronegativity of the lithium metal adds to their cell advantages over other batteries making them the ultimate preferred battery [21]. They are widely used in different domains as indicated in figure 1.2 below but mostly in portable electronic devices. The fluctuations in energy from renewable energy sources such as solar and wind require an efficient storage system to enable the design of reliable renewable energy sources [23, 24]. Lithium-ion batteries are also extensively used in this field and also in the emerging field of electric vehicles [25, 26]. Energy storage systems also play an important role in large scale systems such as smart grids to enable efficient use of electric energy generated from different sources [27, 28, 29].

Figure 1. 2: Application of Lithium-ion batteries in (a) portable electronic and in (b) large scale systems. Portable electronic consisting of smartwatches, laptops, mp3 players, smartphones, power banks, electric cigarettes and wireless keyboard and mouse and large scale system consisting of solar, wind, smart grids and electric vehicles.

1.2 Literature review

A considerable amount of research has been invested in improving lithium-ion batteries to produce an environmentally friendly, durable and an inexpensive battery. Particularly in designing efficient cathode materials as they determine the capacity and the working voltage and to date it has been reported as the most expensive component of the battery [30]. The most studied cathode materials for lithium-ion batteries include $LiCoO_2$, $LiNiO_2$, $LiFePO_4$, $LiMn_2O_4$ and $LiMnO_2$ [4, 31]. In recent studies, Li-Mn-O composite cathode materials have been considered in a quest to design affordable lithium-ion batteries due to the enhanced electrochemical properties and that manganese is more abundant than nickel and cobalt [32, 33, 34], with 20 – 48 % of manganese mined in the Kalahari manganese district of South Africa. Moreover, manganese is the 12th most abundant element in the earth's crust [35, 36]. The importance of nanostructured cathode materials have been outlined in various studies as one of the promising methods in achieving improved electrochemical properties for lithium-ion batteries [37]. Computational methods have made a significant impact in providing significant insights on the electrochemistry of promising electrode materials, particularly, atomistic potential-based approaches [38].

1.2.1 Performance of transition metal oxide cathodes

Various transition metal oxides (TMOs) have been largely studied as cathode materials for Li-ion batteries. $LiCoO_2$ is the most commonly used cathode material in commercial lithium-ion batteries in the interest of its high theoretical specific capacity of 274 $mAhg^{-1}$, good cycling stability and high discharge voltage. However, they lose capacity during deep cycling, they are expensive and thermally unstable which limits their full commercial utilisation [39]. $LiNiO_2$ is one of the promising cathode material owing to its relatively low cost as compared to $LiCoO_2$. However, one of its limitations is in large scale production which can be circumvented by methods such as heteroatoms [40] and sol-gel methods [41]. It also suffers capacity fading during cycling due to phase transition [42].

Olivine $LiFePO_4$ is one of the environmentally friendly and inexpensive cathode materials. However, it possesses a theoretical capacity of ~170 $mAhg^{-1}$ as such it is deemed as a low energy density cathode material [43]. In an attempt to reduce the cost and environmental impact induced by Co, materials such as $LiMn_2O_4$ have been looked into as a possible replacement of $LiCoO_2$. Due to the abundance of Mn,

$LiMn_2O_4$ is potentially a low-cost material. The material is environmentally friendly and possesses high thermal stability, however, it exhibits low specific capacity of ~ 120 $mAhg^{-1}$ and suffers capacity fading at elevated temperatures due to the dissolution of Mn^{2+} into the electrolyte [31]. Several methods have been employed to improve the electrochemical performance of this material such as surface coating, partial substitution of Mn with Ni [44], Cr and Co [45].

Manganese-rich layered structures have ignited interest of many researchers as a cathode material due to its high specific capacity of ~250 $mAhg^{-1}$ when cycled in the voltage range of 2.0 – 4.8 V. It was initiated that this manganese-rich layered structure exists in two phases, the trigonal $LiMnO_2$ phase with space group R-3m and the monoclinic Li_2MnO_3 with space group c2/m. The monoclinic component is believed to stabilise the trigonal structure resulting in enhanced discharge capacity. Nevertheless, not much is known on the effect of each on the electrochemical properties [43, 46]. Besides their attractive properties over other cathode materials, they exhibit some drawbacks which limit their wide usage commercially. Like many manganese cathode materials, it also suffers Mn dissolution induced by the disproportionation reaction of Mn^{3+} to form Mn^{2+} and Mn^{4+} , wherein, the Mn^{2+} dissolves in the electrolyte resulting in capacity fading [47, 48]. Moreover, a layered-to-spinel transformation was suggested and thought to be attributed to the loss of capacity and poor cycle stability during Li-ion extraction. Surface coating methods have been implemented with little success in preventing spinel formation [49]. Cationic doping in an attempt to stabilise the lithium-manganese-oxide (LMO) was not much of a success as the poor cycle stability was retained [39].

1.2.2 Layered-spinel composites

Despite the success of lithium-ion batteries as compared to other battery technologies, for various applications their energy density, capacity and cycling stability is still insufficient [32]. In an effort to improve their performance new cathode materials have been developed to meet the energy demand of technologies such as electric vehicles. Furthermore, the synergistic effect of current propitious cathode materials such as layered and spinel have been considered. The two materials have been reported to be structurally compatible by Johnson C.S et al. [50] in which they synthesised a layered (Li_2MnO_3)-spinel ($LiMn_2O_4$) composite. A specific capacity of 250 mAh/g was obtained when cycling the composite material between 5 and 2 V. Lee E.S et al. [51]

also investigated the electrochemical performance of layered-spinel composite, in which upon cycling the layered phase forms a spinel phase which is not associated with the cubic to tetragonal phase transition due to Jahn-teller distortion.

In an endeavour to reduce the observed voltage fade demonstrated by layered and spinel electrodes during prolonged cycling [52, 53, 54, 55, 56], Long B. R and core-workers [57] have synthesised a layered-layered-spinel composite electrode material, xLi_2MnO_3. $(1-x)LiMO_2$ (M=Mn, Ni). An enhanced capacity of 190 mAh/g was obtained and the observed capacity fading was minimal, this was achieved by controlling the amount of the spinel component and the operating voltage. Improved electrochemical performance (capacity, cycling stability, etc.) was also observed on a layered-layered-spinel composite on a study conducted by Kim D and co-workers [58]. In which, a $0.3Li_2MnO_3.0.7LiMn_{0.5}Ni_{0.5}O_2$ (x = 1.3; y =2.3) layered-layered-spinel composite was prepared by lowering lithium concentration in the parent layered-layered with the Mn: Ni ratio maintained as 0.65:0.35. A layered-layered-spinel composite with 6 % spinel content demonstrated enhanced cycling stability, minimal voltage fade and reduced first-cycle capacity loss.

The integration of layered and spinel components to form layered-layered-spinel and layered-spinel composite materials for use as positive electrode in lithium-ion batteries to achieve enhanced electrochemical properties has been of great interest in literature as reviewed above. This is fuelled by the structural compatibility of the layered and spinel components in which a synergistic effect is observed on the resulting composite material exhibiting high voltage and high capacity. As such, this approach can be exploited to design a high energy density lithium-ion battery with enhanced capacity retention and excellent structural stability.

1.2.3 Nanostructured lithium-ion battery electrodes

Materials with dimension at nanoscale, have been reported to exhibit enhanced or different properties to their bulk forms. Effective, portable high energy lithium-ion batteries can be realised with nanostructured electrodes owing to their alluring properties such as large surface area and short Li^+ diffusion pathways [59, 60]. Enhanced rate capabilities and high power densities desirable for large scale systems such as hybrid electric vehicles (HEVs) or electric vehicles (EVs) can be achieved by nanostructured electrodes owing to their short Li^+ diffusion pathways and better electronic conduction as compared to their bulk counterparts [61, 62]. The large

surface area possessed by nanostructured electrodes enables faster reaction kinetics due to the increased access of electroactive sites and accommodates volume expansion which inhibits structural fracture leading to improved charge/discharge rates and cycle life [63, 64].

Disadvantages of bulk materials such as low Li^+ diffusivity and the dissolution of the electrochemical active metal ion can be addressed by the engineering of nanostructured electrodes and nanoscale coating. The high-voltage $LiMn_2O_4$ spinel has been of great interest to research as a potential replacement for $LiCoO_2$ since it is inexpensive. However, its practical use is hindered by electrolyte decay and capacity fading due to disproportionation reaction of Mn mostly in the presence of HF. Nanoscale coating has been one of the solutions in improving the capacity retention of this material. Enhanced capacity retention at elevated temperatures was observed on $LiCoO_2$ coated $LiMn_2O_4$ spinel [65]. $LiCoO_2$ was also reported to allow Li^+ diffusion resulting in lower irreversible capacity [61].

Engineering of novel nanoarchitectures has proven to be one of the most effective ways for achieving better electrochemical properties required for designing high energy density and high power density lithium-ion batteries. A template of well-ordered mesoporous silica has been used to prepare low-dimensional nanostructured electrodes [66, 67]. In which, a 1D LT-$LiCoO_2$ nanowire cathode material was synthesised and its electrochemical performance was compared to the electrochemical performance of a bulk LT-$LiCoO_2$ cathode. The nanowire cathode was found to exhibit superior capacity retention than the bulk cathode. A high rate capability mesoporous $LiMn_2O_4$ was also synthesised. The mesoporous structure enables fast charge/discharge rates due to its enhanced intercalation kinetics and quick transport of lithium-ions resulting in a high power density electrode [68, 61]. A reversibly capacity of 230 $mAhg^{-1}$ was obtained on a nanowire layered $Li_{0.88}[Li_{0.18}Co_{0.33}Mn_{0.49}]O_2$ prepared by a hydrothermal reaction at 200 ^0C [69, 62]. A solid-state reaction method was also employed in the engineering of nanostructured cathode materials for lithium-ion batteries. Whereby, a micro-spherical Li_2FeSiO_4 cathode material was prepared. A discharge capacity of 153 $mAhg^{-1}$ at a rate of 0.1 C was observed on the nanostructured Li_2FeSiO_4 cathode cycled in the range of 1.5-4.6 V and such improvement was associated with its small particle size and its porous and spherical morphology [70].

1.2.4 Simulated synthesis of materials

The significance of computational simulations is undeniable in science, more especially in the energy storage sector. Due to their ability to predict, guide and provide insights in areas where traditional experiments are expensive, dangerous or difficult to perform. The impact of computational research in modelling of nanomaterials is irrefutable which was more driven by their compelling properties [71, 72]. These models are of great essence as they can aid in predicting structural properties, simulate chemical processes and in characterising materials. The evolution of core-existing structures during synthesis in experiments have made it difficult to model these kind of structures computationally. A simulated synthesis method has been developed to capture such complexities as they evolve during synthesis [73]. The method involves two successive processes, namely amorphisation and recrystallisation. The amorphisation process is necessary to facilitate the evolvement of the shape of the material and recrystallisation is essential to produce the necessary microstructural features observed experimentally.

D.C. Sayle and G.W Watson [74] employed the simulated amorphisation and recrystallisation to perform large-scale atomistic simulations of thin-film oxide interfaces. The final structures comprised of defects, reduced interfacial ion densities, dislocations and low angle rotated domains. R. Maphanga and co-workers [75] have successfully used the same method to derive microstructural models of Li-MnO_2 with microstructural features such as grain boundaries, stacking faults, dislocations and extensive micro-twining.

1.2.5 Structural description

The conventional lithium-manganese-oxygen spinel unit cell studied in this work comprises of 8 lithium atoms, 16 manganese atoms and 32 oxygen atoms. The $LiMn_2O_4$ spinel structure crystallises into a cubic structure with a space group of Fd-3m at room temperature. Lithium atoms are situated at the 8a tetrahedral sites, manganese atoms situated at the 16d octahedral sites and oxygen atoms are situated at the 32e sites forming a close-pack cubic array [76, 77]. The close-packing cubic arrays form three-dimensional lithium diffusion channels. For $LiMn_2O_4$, the 16c octahedral sites are unoccupied. However, upon lithiation of the $LiMn_2O_4$ lithium-ions start to occupy the 16c octahedral sites. The layered Li_2MnO_3 structure studied in this

work has a monoclinic crystal system with a space group of c2/m. The Li_2MnO_3 structure comprise of oxygen atoms situated at the 4i (0.219, 0,0.227) and 8j (0.254, 0.321, 0.223) lattice sites, manganese atoms situated at the 4g (0, 0.167, 0) lattice sites and lithium atoms situated at the 2b (0,1/2/, 0), 2c (0,0,1/2) and 4h (0, 0.66,1/2) lattice sites [78, 79].

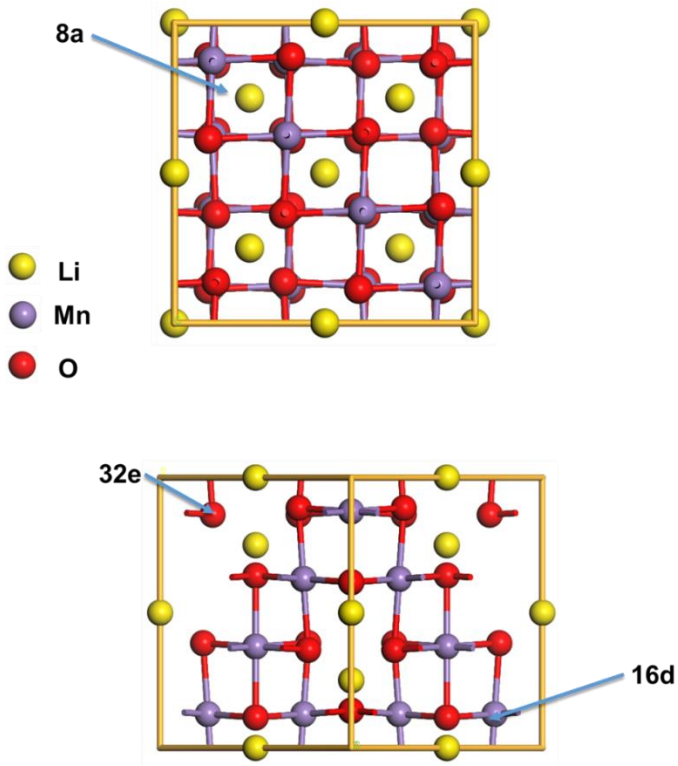

Figure 1. 3: Conventional unit cell of a cubic Fd-3m Li-Mn-O spinel. Lithium atoms (yellow) occupying 8a tetrahedral sites, manganese (blue) occupying 16 octahedral sites and oxygen (red) sitting at the 32e sites.

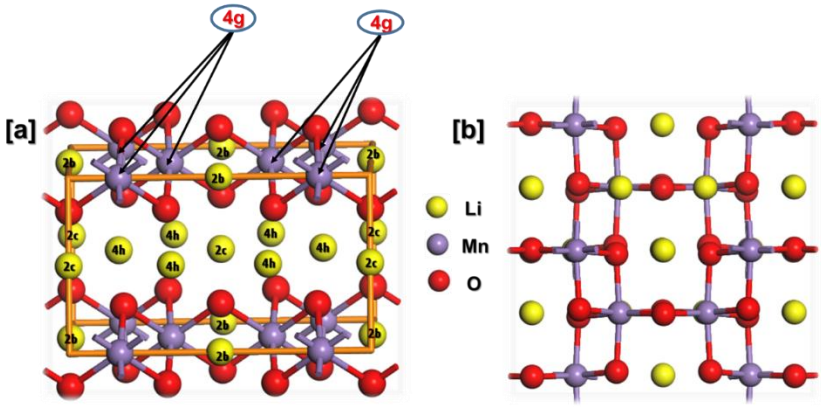

Figure 1. 4: Conventional unit cell of a monoclinic layered Li_2MnO_3 illustrating the (a) Li-Mn-O Wyckoff positions. (b) A view showing the alternating Li-O, Mn-O arrays of the Li_2MnO_3 conventional unit cell.

Table 1. 1: Structural properties of the cubic spinel $LiMn_2O_4$ and the monoclinic layered Li_2MnO_3.

Structure	$LiMn_2O_4$	Li_2MnO_3
Lattice parameters (Å)	a = 8.24	a = 4.937
	b = 8.24	b = 8.532
	c = 8.24	c = 5.030
	[80, 81]	[82, 83, 84]
Volume ($Å^3$)	559.12	202.94
	[77]	[85]
Crystal system	Cubic	Monoclinic
	[80, 81]	[78]
Space group	Fd-3m	C2/m
	[77]	[78]

Table 1. 2: Wyckoff positions and x, y and z coordinates for Li-Mn-O atoms in $LiMn_2O_4$ and Li_2MnO_3 conventional unit cells. References represented by superscripts in parenthesis.

Structure	Atom	site	x	y	z
$LiMn_2O_4$	Li	8a [a, b]	1/8 [a, b]	1/8 [a, b]	1/8 [a, b]
	Mn	16d [a, b]	1/2 [a, b]	1/2 [a, b]	1/2 [a, b]
	O	32e [a, b]	0.2634 [a, b]	0.2634 [a, b]	0.2634 [a, b]
Li_2MnO_3	Li(1)	2b [d, c]	0 [d, c]	1/2 [d, c]	0 [d, c]
	Li(2)	2b [d, c]	0 [d, c]	0 [d, c]	1/2 [d, c]
	Li(3)	4h [d, c]	0 [d, c]	0.6457 [d, c]	1/2 [d, c]
	Li(4)	4g [d, c]	0 [d, c]	0.1641 [d, c]	0 [d, c]
	Mn(1)	2b [d, c]	0 [d, c]	½ [d, c]	0 [d, c]
	Mn(2)	4g [d, c]	0 [d, c]	=y(Li(4)) [d, c]	0 [d, c]
	O(1)	4i [d, c]	0.2305 [d, c]	0 [d, c]	0.2273 [d, c]
	O(2)	8j [d, c]	0.2480 [d, c]	0.3261 [d, c]	0.2199 [d, c]

[a]Reference [86] [b]Reference [79] [c]Reference [85] [d]Reference [87]

1.3 Intentions of the study

The leading lithium-ion batteries are currently lacking in comparison with technological advancements rendering them insufficient for various applications such as electric vehicles [88, 89]. Currently used cathode materials are one of the limiting factors in realising the envisaged affordable and durable safe battery technologies with the ability to deliver high energy. Their limitations include capacity fading transpiring during cycling, inherent low operational capacities, environmental issues due to thermal instabilities, and high cost which inhibit their full utilisation in large scale systems [90, 91, 92]. Optimising the identified potential high energy density cathode materials is one of the expedient efforts in improving the current lithium-ion battery performance [89].

In a quest to meet the high demand for efficient energy storage systems, manganese-based cathode materials have been of great research interest due to their low production cost, environmental friendliness and non-toxicity, particularly spinel $LiMn_2O_4$ and layered Li_2MnO_3. However, they suffer from capacity fading during cycling [93, 94, 95]. In an attempt to optimise their performance, the two materials have been integrated into a composite material due to their structural compatibility. The composite material demonstrated superior properties as compared to the individual materials, such as structural stability, cycling performance and higher specific capacity, > 250 mAh/g. Moreover, the high capacity was ascribed to the layered phase and the better rate capability was associated with the spinel phase [96, 97, 98].

In spite of the significant improvements shown by the layered-spinel composites, their maximum utilisation requires a clear understanding of the structural changes responsible for the noted enhanced performance. Especially the exploration of the discharge process of these composites on an atomic level to yield substantial insights which will guide in the design of the required efficient high energy density lithium-ion batteries. Currently, such knowledge is still lacking in both computational and experimental arenas. Moreover, a number of studies have focused on improving the capacity of the layered-spinel composite electrodes and little is known about their operating voltage during lithium intercalation. One essential requirement of emerging technologies such as electric vehicles is high energy density which is the product of the capacity and the operating voltage. This makes the operating voltage a crucial

component to study, as it also contributes significantly to the total energy density. In this work, we are going to study the discharge process of a lithium-ion battery which utilises the Li-Mn-O layered-spinel composite cathode material, wherein atomic and electronic level structural changes affecting electrochemical performance will be scrutinised. Moreover, in a continuous study, the operating voltage of the Li-Mn-O layered-spinel composite nanoarchitectures which will be generated in this current work will be investigated using the emerging linear-scaling density functional theory code, ONETEP.

Research methodologies and techniques are one of the driving forces in finding solutions in research. They provide means of exploring new scrutiny areas which can result in valuable insights. Computational modelling approaches have made a significant impact in energy storage research. A variety of properties can now be predicted and validated with experiments from various computational methods such as semi-empirical and empirical calculations [99]. Density functional theory has made it possible to unravel electronic structures of many-body systems to predict key properties in various fields [100]. Moreover, accurate electronic properties of different materials have been deduced in a number of studies [101, 102, 103, 104]. Furthermore, macromolecular behaviour of complex systems comprising of a large number of particles can be studied in molecular dynamics (MD) [105, 106]. Moreover, MD techniques such as simulated amorphisation and recrystallisation which is capable of generating models that capture complex essential microstructural features contained in real materials which allows profound analysis and predictions have made a significant impact in unravelling structural properties of different materials [73].

In this work, the discharge process analysis will be performed at electronic and atomic level using density functional theory and molecular dynamics, respectively. Electronic structural changes affecting electrochemical performance during the discharge process will be captured at a smaller scale (< 100 atoms). The electronic structure analysis will be carried out through electronic band structures and density of states (DOS) to reveal significant changes as the discharge process proceeds. The well-researched atomistic simulation technique amorphisation and recrystallisation will be used to generate Li-Mn-O layered-spinel composite nanoarchitectures comprising of essential microstructural features at different lithium concentrations depicting different stages of the discharges process. The generated Li-Mn-O nanoarchitectures will be analysed and characterised through Radial Distribution Functions (RDFs), XRD

Patterns, configuration energy graphs and atomic level snapshots and further validated by High-resolution Transmission Electron microscopy (HRTEM) images.

The study will be carried out in the following manner. First of all, we perform convergence test on our bulk structures to obtain sufficient k-point and cut-off energy parameters to yield structures which are chemical and physical stable before we perform any property calculations. The ability of lithium-ion transfer from the cathode to the anode will then be monitored by electronic band structures and density of states diagrams which clearly captures conductivity properties of a material in question. Furthermore, Li-Mn-O layered-spinel composite nanoarchitectures will then be generated by employing the simulated amorphisation and recrystallisation to allow the atomic-level analysis of the discharge process. Moreover, the generated structures will be instrumental for exploration of various phases and crystallographic defects such as grain boundaries and point defects which exist within these structures as the discharge process proceeds. Their influence on electrochemical performance will be examined and this will aid in the design of a cathode material with better electrochemical properties. In addition, they will also allow electronic structure study and voltage profile calculations of materials that comprise of experimentally observed structural defects with ONETEP [107], which is a linear-scaling DFT code capable of handling large systems at a practical computational cost.

1.4 Outline of the study

Chapter 1 details the importance of the study, challenges, implemented improvement strategies on the current challenges and the current state of lithium-ion batteries. Structural properties of the materials in question are also reviewed and a guide on how the study will be carried out is also outlined. In chapter 2, the theoretical facets of the methods employed to carry out the study are discussed. In Chapter 3, a density functional theory study is carried out. Prediction and discussion of the electrochemical properties of the bulk Mn_2O_4, $LiMn_2O_4$ and $Li_2Mn_2O_4$ spinel structures are conducted. Chapter 4 details the generation of the Li-Mn-O nanoarchitectures using the simulated synthesis. The electrochemical lithiation of the amorphous Li-Mn-O LS nanoarchitectures is also outlined. The chapter also captures the effect of lithiation on the structural changes that affect electrochemical performance. Chapter 5 gives the conclusion and summary of the whole study. It also contains a discussion on the

impact of Li-Mn-O nanoarchitectures on lithium-ion batteries, solutions and recommendations.

CHAPTER 2

Research methodology

This chapter details the research methodology employed to carry out all the computational calculations in this study. The increase in compute power has enabled computational techniques to play an important role in explaining important properties and behaviour of various materials for different application areas [108]. This study makes use of empirical (molecular dynamics) [109] and non-empirical (quantum mechanics) [110] approaches for atomic level and electronic level calculations, respectively. Molecular dynamics is a theoretical technique which is a great tool for describing the interactions between atoms and their trajectories, wherein, essential physical and chemical properties of materials can be derived [111]. The first-principles quantum mechanics approach describes the ground states of electrons in a system without using any empirical parameters [112, 113].

2.1 Density functional theory (DFT)

Density functional theory (DFT) is a chemistry and physics method based on quantum theory which is used to study the ground-state electronic properties of a molecular or atomic system [114, 100]. In simple terms, it is a method of approximating the solution of the Schrödinger equation for a many-body system. The basis of DFT is formed by the two theorems developed by Kohn and Hohenberg [112]. The first theorem postulates that from the electron density which is a function of three spatial coordinates one can calculate ground-state electronic properties of a many-body system. This forms a basis for the approximation of a many-body system by the use of the electron density. The second theorem demonstrates that the full solution of the Schrödinger equation is the electron density that minimises the overall energy functional. As such, the ground state electron density can be obtained by minimizing the energy given that the true energy functional exists. Moreover, if the ground-state electron density is known, then all the properties for the system in question can be calculated [115]. The Kohn-Sham equation is equivalent to the Schrödinger equation and is defined as,

$$\left[-\frac{\hbar^2}{2m}\nabla^2 + V_{eff}(r)\right]\psi_i(r) = \varepsilon_i\psi_i(r), \tag{2.1}$$

whereby

$$V_{eff}(r) = V_C(r) + \mu_{xc}[\rho(r)]. \quad (2.2)$$

The ground-state electron density is equivalent to the minimum total energy of the system which is represented by these wave functions corresponding to the electron density. The total energy functional as described by Walter Kohn and Lu Jeu Sham is given as

$$E = \frac{1}{2}\sum_{occ}\varepsilon_i + U_{nn} - \frac{e^2}{2}\iint\frac{\rho(r)\rho(r')}{|r-r\prime|}drdr' + E_{xc}[\rho(r)] - \int\rho(r)\mu_{xc}dr. \quad (2.3)$$

The total electron density which is established from one-electron wave functions is resolved into one-electron densities,

$$E = E(\rho). \quad (2.4)$$

The Hartree-Fock theory is one of the simplest implementations of the ab initio methods which enabled calculations of the electronic structure of solids [116]. These methods approximate a wave function and energy for a many-body system in a stationary state by a single Slater determinant given an exact N-body wave function. The Hartree-Fock forms the basis for the implementation of methods that accurately describe the ground state electronic properties of a many-body system [117]. Electron density is a significant feature in DFT and is simply defined as the probability of finding an electron in space. A region with higher electron density implies a higher likelihood of finding an electron in that region. The electron density is a scalar quantity described by a three-dimensional grid space and is generally calculated by Fourier synthesis. The electron density at a point r in space is given as,

$$\rho = \rho(r). \quad (2.5)$$

A three-dimensional Fourier series can also be used to express electron density of a many-electron system, i.e.

$$\rho(x,y,z) = \frac{1}{V_{\text{cell}}}\sum_h\sum_k\sum_l F(hkl)\mathrm{e}^{-2\pi i(hx+ky+lz)}, \quad (2.6)$$

where $F(hkl)$ represents the structure factor. The total energy of a given physical system comprises of the contribution of the system's kinetic energy, Coulomb power and the exchange-correlation energy which describes all the many-body interactions of the contained atoms. The total equation is thus:

$$E = T_0 + U + E_{xc.}, \quad (2.7)$$

where the total kinetic energy of the system is represented by T_0.

2.1.1 Approximation methods

2.1.2.1 Local density approximation (LDA)

The simplest exchange-correlation energy approximation is one that presumes that density of the electrons can be treated the same as the electron density of a uniform gas for systems with a slight variation in density. This approximation was introduced by Kohn and Sham, wherein, at each point, the exchange-correlation resembles that of a uniform electron gas with the same density [113]. LDA is one of the extensively used pure DFT approximations to the exchange-correlation energy functional. The exchange-correlation energy of an electron assuming a homogeneous electron density gives an approximation of $E_{xc}[n(r)]$ at a given point r therefore

$$E_{xc}[n(r)] = \int \varepsilon_{xc}(r)n(r)d^3r, \tag{2.8}$$

where for a homogenous electron gas of density $n(r)$, the exchange-correlation energy per particle is given as $\varepsilon_{xc}(r)$. Moreover, the exchange-correlation potential is thus expressed as,

$$v_{xc}[n(r)] = \epsilon_{xc}[n(r)] + n(r)\frac{\delta\epsilon_{xc}[n]}{\delta n(r)}. \tag{2.9}$$

The total energy of the system is then given by

$$E[n] = \sum_i \varepsilon_i - \frac{e^2}{2}\int dr \int dr' \frac{n(r)n(r')}{|r-r'|} + \int drn(r)\epsilon_{xc}[n(r)] - v_{xc}[n(r)] \text{ [118]}. \tag{2.10}$$

LDA forms a basis in which more sophisticated exchange-correlation energy approximations can be constructed. The generalised gradient approximation is one of the advanced exchange-correlation approximations constructed from LDA [119, 120, 121].

2.1.2.2 Generalised gradient approximation

In an instant where the electron density goes through a swift change, the local density approximation (LDA) is unable to give accurate results, for instance in molecules. The Local Spin Density (LSD) approximation is one of the widely used exchange-correlation energy approximations, however, for a chemical system that necessitates accuracy of calculated energy difference, it is deemed inadequate [122, 123]. LSDA approximation to the exchange-correlation is expressed as

$$E_{xc}[\boldsymbol{n}] \approx E_{xc}^{LSDA}[\boldsymbol{n}] = \int \boldsymbol{d}^3 r n(\boldsymbol{r})\varepsilon_{xc}^{hom}\big(n\uparrow(\boldsymbol{r}), n\downarrow(\boldsymbol{r})\big), \tag{2.11}$$

where, the exchange-correlation per electron constituting the spin polarised uniform electron gas is represented by ε_{xc}^{hom}. Moreover, the spin-up and spin-down densities are denoted by $n\uparrow$ and $n\downarrow$ [124], respectively.

The generalised gradient approximation improves on the limitation of LDA by considering the gradient of the electron density, such that the exchange-correlation potential depends not solely on the electron density but also on the gradient of this density. GGA gives a better description of the atoms which results in a better structural energy difference and provides a better description of the atomic bonds. This results in the prediction of qualitative results.

2.1.2 Plane-wave pseudopotential method

In order to calculate with high accuracy the variational self-consistent solution of the density functional theory, a plane-wave pseudopotential method can be used. In a plane-wave pseudopotential technique, a plane-wave basis is coupled with a pseudopotential technique to describe an orbital of a crystal. The contribution to this pseudopotential is explicitly from valence electron rather than also from the inert core electrons.

2.1.3.1 Plane-wave basis set

Wave functions are the core base objects in quantum chemistry and they can be represented by a linear combination of plane-wave basis set as described by Bloch's theorem [125]. The theorem states that an electronic wave function can be expressed as a discrete plane-wave basis set given by

$$\Psi_{ki}(r) = \exp[ik.r]\, f_i(r), \tag{2.12}$$

where the periodicity of the system is denoted by $f_i(r)$, and it can be expanded into discrete plane waves using a basis set, as indicated below

$$f_i(r) = \sum C_i G^{[iG.r]}, \tag{2.13}$$

where the reciprocal lattice space vectors in the sporadic lattice is denoted by G. Therefore, the electronic wave function can be represented by a summation of the plane waves as illustrated below

$$\Psi_{ki}(r) = \sum C_{i,k} + G^{[i(k+G).r]}, \tag{2.14}$$

where the plane wave coefficients $C_{i,k}$ are fully dependent on the specific kinetic energy given by,

$$\frac{\hbar^2}{2m}|K+G|^2, \tag{2.15}$$

including all plane waves with kinetic energies less than a particular specified cut-off energy (Ecut) represented as

$$\left(\frac{\hbar^2}{2\mathrm{m}}\right)|\mathrm{K}+\mathrm{G_c}|^2 \;<\; \mathrm{E_{cut}} \tag{2.16}$$

This kinetic energy cut-off can control the convergence of this expansion. A greater kinetic energy cut-off allows the inclusion of more plane waves which improves the description of the atomic orbitals. Hence, increasing the cut-off energy improves the convergence of your system resulting in reliable predictions of structural properties. For a given kinetic energy cut-off, the convergence of a system can be improved by using a denser set of k-points to improve the description of the Brillion Zone.

2.1.3.2 Pseudopotentials

The electronic wave function can be expanded by a linear basis set, however, describing the whole atom using the combination of these sets results in a complicated system. The complications are due to the need for a significant number of plane waves required to clearly describe the nucleus and the core electrons. A pseudopotential method replaces the coulomb potential term with an efficient potential which exploits the fact that physical properties of a material are more dependent on the valence electrons rather than on the core electrons. The more complex description takes into account the motions of the core electrons. However, the nucleus can be approximated by a simple approach which enables the use of plane-wave basis sets as the pseudo wave functions and can now be represented by less Fourier modes. The Pseudopotential method implemented in density functional theory has made it possible to obtain valuable insight on the chemical bonds of solids. A pseudopotential is formed on a basis that the pseudo wave functions and the potential should concur with the true wave function and with a certain potential cut-off radius outside. Furthermore, within the core region, the pseudo wave function should not contain any radial nodes. Moreover, the potential should be able to reproduce the atomic properties of the element in question, especially the inclusion of the phase shifts due to the scattering of the core region. The phase shifts arise from the angular momentum state, as such the pseudopotential should not be localised [126, 127]. Equation below shows the most general form of a pseudopotential,

$$\mathrm{V_{NL}} = \sum_{\mathrm{lm}} |\mathrm{lm}><\mathrm{V_i}<\mathrm{lm}|, \tag{2.17}$$

where V_i the angular momentum of the pseudopotential and the spherical harmonics are depicted by $|lm>$. The electronic wave function decomposes into spherical harmonics when acted upon by the angular momentum of this pseudopotential whereby each spherical harmonic is then multiplied by an appropriate pseudopotential V_i.

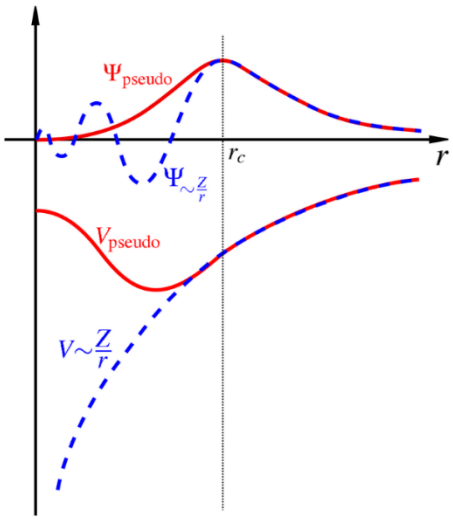

Figure 2. 1: A schematic illustration of a pseudopotential. Where the solid line indicates the all-electron potential and the dashed lines illustrating the pseudopotential with its respective valence wave function and the pseudo-wave functions [128].

2.1.3.2.1 Norm-conserving pseudopotentials

The Norm-conserving pseudopotential is one of the most used pseudopotentials in recent plane-wave electronic structure codes which attempts to simplify the electronic structure calculations by neglecting the effect of the atomic core states [129]. The approximation is an example of a non-localised pseudopotential as it uses a distinct potential for every angular momentum components of the electronic wave function. Contrary to a non-local pseudopotential, a local pseudopotential uses the same potential for each angular momentum components. Hamann, Schluter and Chiang [130] are the first developers of the norm-conserving pseudopotential and it was further advanced by Kleinman and Bylander [131]. The all-electron valence and the pseudo valence for a given reference configuration should be able to reproduce similar eigenvalues. Furthermore, for a given cut-off radius, the wave functions of the all-electron valence and the pseudo valence should agree beyond the given or chosen cut-off radius [132]. Norm-conserving is one of the widely used plane-wave potential

approximations with the ability to produce high-quality results. The first norm-conserving pseudopotential proposed in 1979 is written as:

$$\hat{V}_{ps}(r) = \sum_l \sum_m |Y_{lm} > V_{lm}(r) < Y_{lm}, \quad (2.18)$$

where the one-particle wave function is represented by Y_{lm}, the angular momentum is denoted by $\{l, m\}$ and $\hat{V}_{ps}(r)$ is the pseudopotential.

2.1.3.2.2 Ultrasoft pseudopotentials

Ultrasoft pseudopotentials was developed by Vanderbilt [133] in 1990, it improves on norm-conserving pseudopotentials by the use of a softer pseudo-wave function composed of fewer plane-waves. A lesser cut-off energy for a given plane-wave basis set can be used to perform accurate calculations. Orbitals that are tightly bound and are sharing some of its significant weight into the core region are described by a substantial number of basis set. A large number of basis set requires a higher cut-off energy. As such, to reduce the cut-off energy, the charge associated with these orbitals from the core region is truncated, this results in softer pseudo wave functions in the core region and a substantial reduction in the cut-off energy. Moreover, generalised orthogonality is introduced to achieve a pseudopotential which is as soft as possible. In which, the ultrasoft pseudopotentials require half the cut-off energy and a fewer number of plane-waves in a calculation than the norm-conserving pseudopotentials.

2.1.3 CASTEP simulation code

Cambridge Serial Total Energy Package (CASTEP) [134, 135] is a first principle density functional theory code which uses a plane-wave basis set. The code is extensively used to calculate electronic properties of crystalline solids, surfaces, molecules, etc. It provides a number of essential tools for acquiring earnest physical quantities from the ground state electronic wave function. The CASTEP code makes use of the Born-Oppenheimer approximation to approximate the man-body wave function which is made concerning the electronic coordinates of the nuclear. Bloch's theorem is also incorporated in the code which enables the use of pseudopotentials to reduce computational cost.

2.2 Molecular dynamics

Molecular dynamics is a well-known empirical method used to simulate the behaviour of a given system, such as a solid material or a solid solution. The use of molecular dynamics simulations enabled the study of atomic motion to predict and understand their structural and thermodynamic properties [136]. The behaviour of the system is controlled by the supplied energy which influences the interactions of atoms in the system. The interaction between atoms is governed by force fields or interatomic potential functions, and their atomic motions are mostly based on Newton's 2nd law of motion given by:

$$\bar{F} = m\bar{a}\,, \tag{2.19}$$

where $\bar{a}$ is the acceleration, which is dependent on the net force $\bar{F}$ and mass m. From the integration of the above equation, we can derive the velocity and variation after chosen time steps [137].

Atoms in a molecular dynamics system imitate atoms in real life by presuming a given energy function, from which the force experienced by a given atom as a consequence of other atoms in the system can be calculated given its atomic position. The motion of these atoms is described by Newton's second law which is based on the forces experienced by the atoms. The molecules in a system are regarded as an assembly of interacting classical particles in that their position is determined from the integration of classical equations. Molecular dynamics simulations give insights into the structural and dynamic properties of systems in question [138, 139]. Empirically parameterised force fields such as AMBER [140], CHARMM [141] and GROMOS [142] are some of the force fields used to describe the force experienced by atoms in a molecular dynamics system.

2.2.1 The potential model

The potential mode is an important physics concept which enables the study of particles or high energy physical systems. The potential model describes the distinction in the energy of molecules or solids based on the atomic coordinates, which is the amount of interaction energy at a given point by virtue of other points in space. It can be further understood as the probability and intensity measure of interaction [143, 144]. The more accurate and of great quality the potential model be, the more authentic the calculations be.

2.2.1.1 Buckingham potential

The Buckingham potential [145] describes the repulsion between two atoms which are not directly bonded. This repulsion originates from the Pauli Exclusion Principle [146] and van der Waals energy for a pair of atoms in question. The formula was initiated by Richard Buckingham and is given by:

$$\Phi_{ij} = A_{ij}.\exp^{\frac{r_{ij}}{p_{ij}}} - \frac{c_{ij}}{r_{ij}^{6}}, \tag{2.20}$$

where the first term is the Born-Meyer and the attraction in which the Bucking potential is added. A_{ij} , P_{ij} and C_{ij} are constants. The first term represents repulsion and the second term represent attraction with respect to interatomic distance. The Buckingham potential is the simplified version of the Lennard-Jones potential. This potential has been widely used in molecular dynamics simulations.

A short-range interaction is dependent on the separation distance and the interacting ions in which the interaction could result in a repulsive interaction or a combination of a repulsive and an attractive interaction. When the separation between two interacting ions is small allowing overlap between the electron clouds of the two ions. The resulting interaction is repulsive with contribution from the nuclear-nuclear interaction. The repulsive force stemming from an overlap in electron clouds which is due to the Pauli Exclusion Principle [146] which state that no two fermions can have the same quantum state. However, when the separation between the two ions is large, the interaction results in a small attractive force generally known as the van der Waals-London interaction. The force is due to the natural development of instantaneous dipoles on each of the interacting ions. A three-body short-range interaction can be given by:

$$\phi_{s-r} = \sum_{ij}\phi_{ij} + \sum_{ijk}\phi_{ijk} + \sum_{ijkl}\phi_{ijkl} + ..., \tag{2.21}$$

where ion pair interaction is represented by ij , and the three-body interaction is depicted by ijk .

2.2.2 Born model of ionic solids

The molecular dynamics calculations performed in this study are based on the Born model of ionic solids. A crystal lattice in a classical simulation is described by Born model of ionic solids in which the crystal lattice is assumed to be formed by a formally

charged ionic spheres extending infinitely in the crystal. The ionic interactions in the crystal lattice, take place through interatomic forces as a function of their lattice positions. The ionic spheres are regarded as point charges and their interaction energy is given by:

$$U_{ij} = \frac{1}{4\pi\varepsilon}\frac{q_i q_j}{r_{ij}} + \Phi\left(r_{ij}\right), \tag{2.22}$$

where U_{ij} is the Coulombic interaction corresponding to the electrostatic interactions between the ions and $\phi(r_{ij})$ is the short-range force. Furthermore, ε is the permittivity of the vacuum, q_i and q_j are the ionic point charges and r_{ij} is the interatomic separation between the ionic point charges.

2.2.3 Long and short-range Coulomb interactions

The interaction between ions is divided into two forms of interatomic interactions, namely, long-range electrostatic interaction and short-range interaction. The long-range electrostatic interaction forces are simply defined by:

$$\psi = \sum_{l,i,j}\frac{q_i q_j}{4\pi\varepsilon_o\left(r_{ij}+l\right)}, \tag{2.23}$$

where the charges for the ions i and j are q_i and q_j, l is the set of periodic lattice vectors of the crystal lattice and r_{ij} is the interatomic separation of i and j. Long-range electrostatic force is an electrostatic force between ion pairs in which for oppositely charged ions the force is attractive and for like charges the force between the atoms is repulsive.

2.2.4 DL_POLY simulation code

DL_POLY [147] is a molecular dynamics simulation code, capable of running segments of its code on a wide range of parallel computers of distributed memory owing to its built-in parallel algorithms. The code can simulate from small system with 100 atoms on single-processor workstation, to large systems with millions of atoms.

2.2.5 Theoretical models

All the atoms (Li, Mn and O) in the layered-spinel composite nanoarchitectures studied in this work were described by the Born approximation [148] for all the molecular

dynamics calculations performed. Moreover, the Li-Mn-O ions interact through short-range and long-range Coulomb interactions.

2.2.6 Statistical ensembles

A statistical ensemble describes the possible states (microstates) of a real system at a given time. The system can be defined by an infinite collection of microstates which are determined by the constraints imposed on the system [149]. A molecular dynamics system can be defined by a statistical ensemble in which the system's thermodynamic properties such as, temperature and pressure can be controlled. In this work, we employ two types of statistical ensembles namely, micro-canonical and canonical ensembles. A micro-canonical ensemble (NVE) in equilibrium, contains a constant number of particles (N), volume (V), and total energy (E). A trajectory of an NVE ensemble can be viewed as an exchange in potential and kinetic energy but the total energy remains conserved. A canonical ensemble (NVT) consists of a constant number of particles(N), volume (V) and temperature (T). The system can be viewed as a closed microscopic system in contact with a heat bath such that different microstates can have different energies.

2.2.7 Amorphisation and recrystallisation technique

An amorphisation process involves heating a system in a statistical micro-canonical ensemble which results in a loss of long-range order atomic arrangements. The process yields an amorphous (unstable) structure. The recrystallisation process is usually carried out in a canonical ensemble, where the energy of the microstates in the system subjected to a specific temperature is allowed to change for a given number of particles and volume. During the process, atoms occupy low energy (stable) configurations resulting in a polycrystalline or crystalline structure comprising of long-range atomic ordering [150].

The simulated amorphisation and recrystallisation technique has been widely used due to its capability to generate complex structures from which a number of properties can be obtained. The technique afforded researchers a chance to simulate structures comprising of features that are observed experimentally. Consequently, the generated structures are instrumental to insightful findings. Essential microstructural features evolve as the simulated recrystallisation process proceeds. The technique can capture microstructural features such as grain boundaries, point defects, dislocation, etc. Such

structural features are deemed essential as they affect the performance of various materials in different application areas [64].

2.3 Analytical procedure

2.3.1 Crystallographic defects

Crystals, in reality, do not have perfect regular geometric arrangement. Atoms in all materials comprise of imperfections which may result from deformation or evolve during cooling as a function of temperature or high-energy radiation. Crystals defect have a profound influence on the behaviour of a material. These defects can affect a material's properties such as mechanical, optical and electric properties [151, 152]. Crystal defect in a material can be found on a single lattice point, on a surface or along lines and they are called point defects, surface defects and line defects, respectively. Point defects include defects such as vacancies, substitution and interstitial defects, Line defects include edge dislocations and screw dislocations defects, and surface defects comprise of grain boundaries and material surface defects. All different types of crystal defects affect a material's properties differently. Point defects have a strong control on the conductivity of heat and electricity in metals. Moreover, in materials such as semiconductors, their electronic conductivity are strongly affected by substitutional point defects. Vacancy defects can facilitate diffusion of ions. The mechanical strength of a material can be strongly controlled by crystal defects [153, 154].

2.3.1.1 Point defects

Point defects are disruptions of a perfect lattice arrangement such as displacement of atoms from their lattice sites into interstitial sites. Point defects can involve one or a pair of atoms. Effects of point defects can extend to a larger area in the crystal even though it occurred on one or two lattice sites. As mentioned above, there are three main forms of point defects (vacancy, interstitial and substitutional). A point defect that occurs due to missing atom from its lattice site is called a vacancy point defect and it results in a misalignment in the atomic position of the surrounding atoms as illustrated in figure 2.2. This type of defect can form during crystallisation from molt in which some of the lattice sites as the atoms occupy their low-energy crystalline sites remain unoccupied. They can also be formed during a process which alters the shape of the crystal such as plastic forming [155, 156], wherein, atoms are displaced from their lattice sites as the new shape is formed. In a case where an atom occupies a

normally unoccupied lattice site, such a crystal defect is called interstitial point defect. An interstitial defect which generally exist in small concentrations can be as a result of an impurity atom or one of the atoms in the crystal (self-interstitial) occupying an interstitial site. In a substitutional point defect, an atom occupies a lattice site which is normally occupied by a different atom, the two atoms are usually of similar size. Other types of point defects are Frenkel defects and Schottky defects. Frenkel defects occur when an ion moves from its normal lattice position into an interstitial site, resulting in vacancy and an interstitial point defects (vacancy-interstitial). A Schottky defect occurs in a material comprising of ionic bonds where a cation and an anion are missing from their lattice positions to maintain charge neutrality.

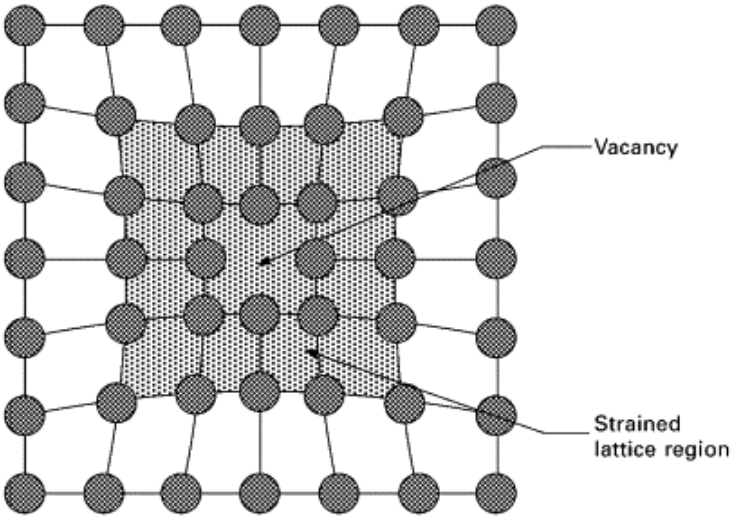

Figure 2. 2: An illustration of a vacancy point defect resulting in a high strain region denoted by the shaded area [157].

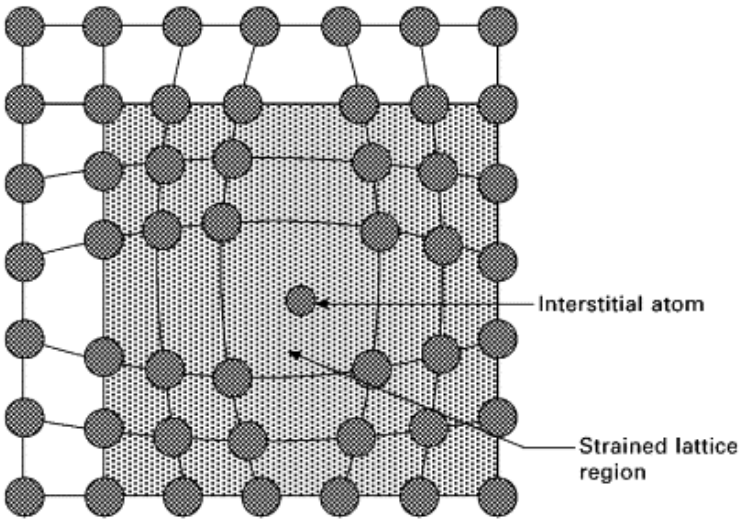

Figure 2. 3: A schematic illustration of an interstitial point defect and the lattice strain caused [157].

2.3.1.2 Line defects

Mechanical properties of a material are mainly influenced by line defects such as dislocations. Properties such as ductility and deformability are strongly influenced by line defects [158]. In a line defect, a perfect atomic arrangement is disturbed along a given lattice plane in the crystal. They are called line defects since they can be described in terms of their width and length. They can be formed during plastic forming and also during crystallisation. Strong metals comprise of a significant number of line defects and low-strength metals contain a lower concentration of line defects [159, 160].

2.3.1.3 Surface defect

Most materials comprised of many crystal grains joined together by grain boundaries which are surface defects. Materials comprising of single grains are rarely found in reality [161, 162]. The crystal grains contained in a polycrystalline material are oriented in different directions to each other. The atoms contained in single grains exhibit long-range atomic ordering. Grain boundaries discontinue the motion of line defects such as dislocation. As such, they also control mechanical properties of materials, particularly, metals. There are two types of grain boundaries, namely a low-angle boundary and a high-angle boundary. A low-angle boundary is formed when two crystal are oriented similarly but not the same and a high-angle boundary is formed when two crystals have distinct orientations [163, 164].

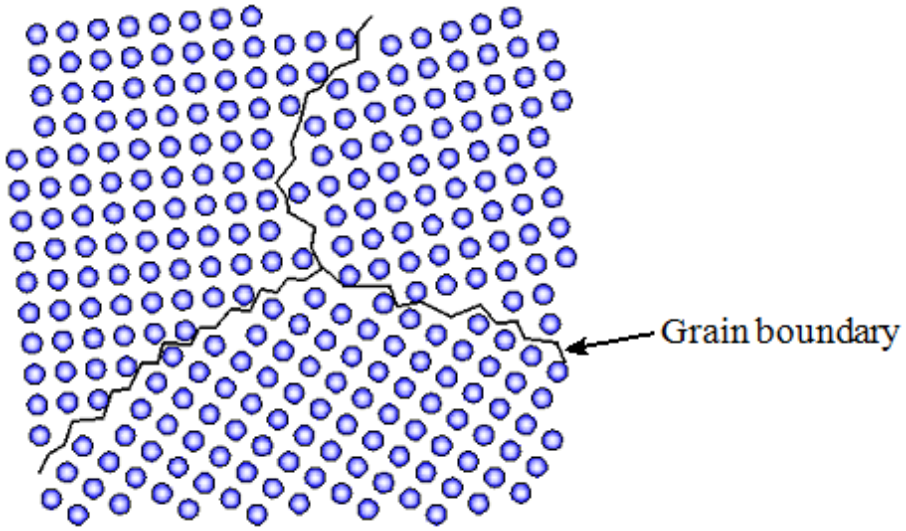

Figure 2. 4: Demonstration of a crystalline comprising of grain boundary surface defect.

2.3.2 Radial distribution function

A radial distribution function (RDF) defines the probability of finding an atom located at a distance r away from a reference atom in a crystal system. RDF varies base on the type of material, as such solids, liquids and gases will demonstrate distinct RDF graphs. RDF graphs detail the distribution of atoms from which a phase of a material can also be deduced. A length of a chemical bond between the reference atom and target atom can be obtained from an RDF graph. Following that, the RDF peaks denote the nearest neighbour distance such that the first RDF peak denotes a bond length of the atomic interaction in question. In a liquid, the average density at any point in the liquid is the same for any other point in the entire system, and it is called a bulk density. However, the density from a reference point to another point in the system uniquely defines the system. The coordination number $n_{ij}(r)$ is defined as by,

$$n_{ij}(r) = 4\pi\rho \int_{r\min}^{r\max} r^2 G(r) dr \,, \tag{2.24}$$

where density is given by the number of atoms N in the system per given volume V $\rho = \frac{N}{V}$ and the probability of finding an atom located at a distance r from a reference atom [165, 166].

2.3.3 X-ray diffraction pattern

X-ray diffraction pattern (XRD) indicates the intensity of a scattered X-rays and their respective diffraction angles (2thetha). An x-ray diffraction pattern can be used to determine the atomic and molecular structure of a crystal. The diffraction angles (peak positions) and their respective intensities provide qualitative information about a crystal structure of material. Furthermore, useful information such as lattice constants of a material in question can be determined from the XRD pattern. Crystals with long-range atomic ordering show clear diffraction peaks [167, 168]. Small crystal with their crystal sizes ranging below 100 nm show broad XRD peaks. This is explained by Scherrer equation [169] defined by,

$$\langle L \rangle = \frac{K\lambda}{\beta cos\theta}, \tag{2.25}$$

where λ the wavelength of the incident x-ray is, $< L >$ is the dimension of the particle in the direction perpendicular to the reflecting plane, β is the peak width. A calculated XRD pattern is compared to available recorded XRD patterns of known materials to

identify material in question. Information such as morphology and crystal phases can be obtained from an XRD pattern. Furthermore, the crystallinity, structural defects and the average grain size can also be deduced.

CHAPTER 3

Electronic structure of the magnetic and non-magnetic Li-Mn-O spinel structures: Mn_2O_4, $LiMn_2O_4$ and $Li_2Mn_2O_4$.

This chapter gives a full discussion and analysis on the electronic structural changes of $Li_xMn_2O_4$ ($1 \leq x \leq 2$) which has a major influence on the movement of electrons during the discharge process. The Mn_2O_4, $LiMn_2O_4$ and $Li_2Mn_2O_4$ delineate some of the crucial stages that the material undergoes during the discharge process. Structural properties such as lattice parameters and volume are monitored during Li^+ insertion/extraction as their significant changes such as volume expansion/contraction may result in poor rechargeability due to mechanical failure [170, 171, 172]. Density of states (DOS) and electronic band structures will be calculated in order to reveal the electronic structure of Li-Mn-O spinel and its conductivity as a function of lithium content. The Fermi level which defines the highest occupied states at absolute zero temperature described by DOS and electronic band structures will aid in understanding the electronic properties of the material in question. Non-spin and spin polarised electronic properties calculations will be performed in order to consider the non-magnetic and magnetic Li-Mn-O spinel structures which will be done by disregarding and regarding the effect of the intrinsic angular momentum of the Li-Mn-O atoms.

3.1 Structural analysis of Mn_2O_4, $LiMn_2O_4$ and $Li_2Mn_2O_4$

This section presents structural analysis of the Mn_2O_4, $LiMn_2O_4$ and $Li_2Mn_2O_4$. The delithiated-Mn_2O_4 is formed by a topotactic removal of lithium atoms from $LiMn_2O_4$ resulting in an Fd-3m cubic structure [173, 174] as depicted in figure 3.1. A significant number of lithium atoms can be intercalated topochemically into this structure, wherein the Mn^{4+} ions gets reduced into Mn^{3+} ions with lithium insertion [175]. Lithiation of $LiMn_2O_4$ into $Li_2Mn_2O_4$ in this work retains the Fd-3m space group and the cubic crystal structure. However, experimentally it has been observed that lithium insertion into $LiMn_2O_4$ reduces the cubic symmetry into tetragonal I41/amd symmetry [176]. Manganese (16d octahedral sites) and oxygen (32e sites) atoms reside in the same lattice positions in the spinel structures discussed here. Lithium atoms occupy 8a

tetrahedral sites when x is between 0 and 1 in $Li_xMn_2O_4$ ($0 \leq x \leq 2$) and starts occupying the 16c octahedral sites when x is between 1 and 2. In the Mn_2O_4 spinel structure, vacant Li intercalation sites are both the 8a tetrahedral sites and 16c octahedral sites. As lithium atoms are intercalated into this system (Mn_2O_4) they start by occupying the 8a tetrahedral sites. However, Li intercalation from $LiMn_2O_4$ ($1 \leq x \leq 2$) results in hopping of lithium atoms from 8a tetrahedral sites into 16c octahedral sites [177, 178, 76] as indicated in figure 3.1.

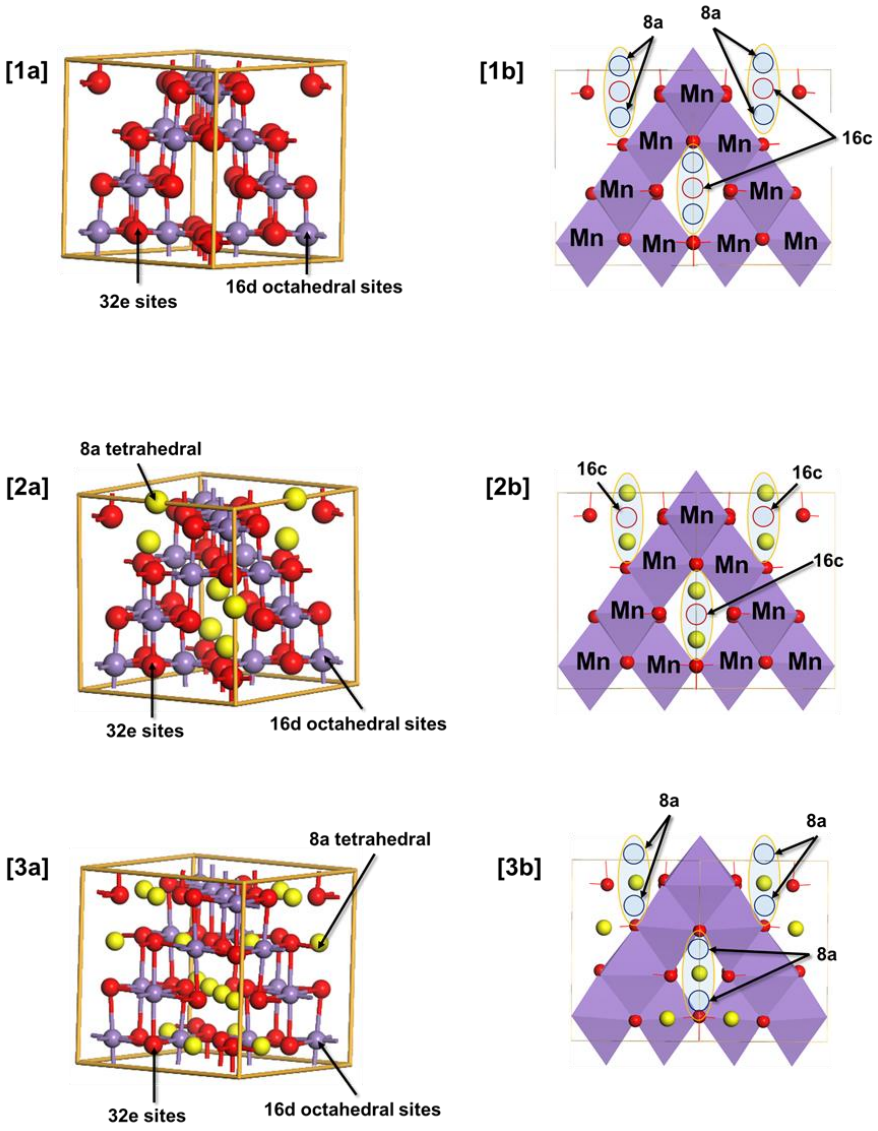

Figure 3. 1: Fd-3m cubic spinel conventional unit cells and their respective Li lattice sites (8a tetrahedral and 16c octahedral): (a) Mn_2O_4, (b) $LiMn_2O_4$ and (c) $Li_2Mn_2O_4$ cubic spinel $LiMn_2O_4$. Lithium (yellow) atoms in $LiMn_2O_4$ occupy the 8a tetrahedral sites and the 16c octahedral sites in $Li_2Mn_2O_4$. In all the spinel structures depicted in this figure, manganese (blue) atoms occupy 16d octahedral sites and oxygen (red) atoms occupy the 32e sites.

3.2 Computational details

The first-principles electronic structure calculations based on density functional theory are performed under the (GGA) exchange-correlation function with the Perdew Burke Ernzerhof (PBE) [179] exchange-correlation functional. The basis set of the electronic wave functions are approximated by the ultrasoft pseudopotentials as implemented in the CASTEP code. Consequently, the atomic interactions of Li, Mn and O in Li-Mn-O spinel were described [133]. A plane wave function with energy of 800 eV was sufficient to describe the electronic orbitals of Li-Mn-O spinel structures studied in this work. The Brillouin zone is sampled by a 4x4x4 Monkhorst pack k-mesh sampling scheme. The atomic positions of all the Li-Mn-O spinel structures in question were fully relaxed using the Broyden-Fletcher-Goldfarb-Shanno (BFGS) algorithm. A 0.05 eV/Å and 0.1 eV force and stress convergence tolerances were used, respectively. The ground-state wave functions are computed using the density mixing electronic minimiser with the Pulay mixing scheme as adopted in CASTEP. The magnetic moments in the spin polarised structures were arranged in a ferromagnetic ordering. In which, the magnetic moments of all the manganese ions (Mn^{3+} and Mn^{4+}) were aligned in the same direction in all the structures (Mn_2O_4, $LiMn_2O_4$ and $Li_2Mn_2O_4$). Generally, the total magnetic moments of the ferromagnetic conventional Li-Mn-O spinel unit cells can be represented as $S = 8 \times S_a + 8 \times S_b$, where S_a and S_b are the total magnetic moments of Mn^{4+} ($t_{2g}^3 e_g^0$) and Mn^{3+} ($t_{2g}^3 e_g^1$) respectively.

3.2.1 Cut-off energy and k-mesh convergence test

In order to obtain a ground-state electronic structure of Li-Mn-O spinel structure, a cut-off energy and k-mesh convergence test was performed and the results of the test are shown in figure 3.2 and 3.3 below. Figure 3.1 shows non-spin polarised and spin polarised total energy and cut-off energy plot for cubic $LiMn_2O_4$ spinel structure, respectively. The two graphs show a similar trend and both start converging from the cut-off energy of 400 eV. However, in order to obtain profound predictions, cut-off energy of 800 eV was chosen for the plane wave functions and it was sufficient to describe the electronic structure of $LiMn_2O_4$ as evinced by the generated results which are comparable to experimental results. The spin polarised $LiMn_2O_4$ converged to a lower total energy than the non-spin polarised $LiMn_2O_4$. This alludes that the spin polarised calculation may give a better description of $LiMn_2O_4$ which is closer to experiments as compared to the non-spin polarised calculations. The chosen cut-off

energy was then used to perform the non-spin and spin polarised k-mesh convergence test calculations depicted in figure 3.3. In which, the total energy is plotted against k-mesh for non-spin polarised and spin polarised cubic $LiMn_2O_4$ spinel in the figure. The curves of the graphs depicted in the figure show a great resemblance. A similar behaviour to the cut-off energy is also noted, the spin polarised $LiMn_2O_4$ structure also converges to a lower energy than the non-spin polarised $LiMn_2O_4$ structure.

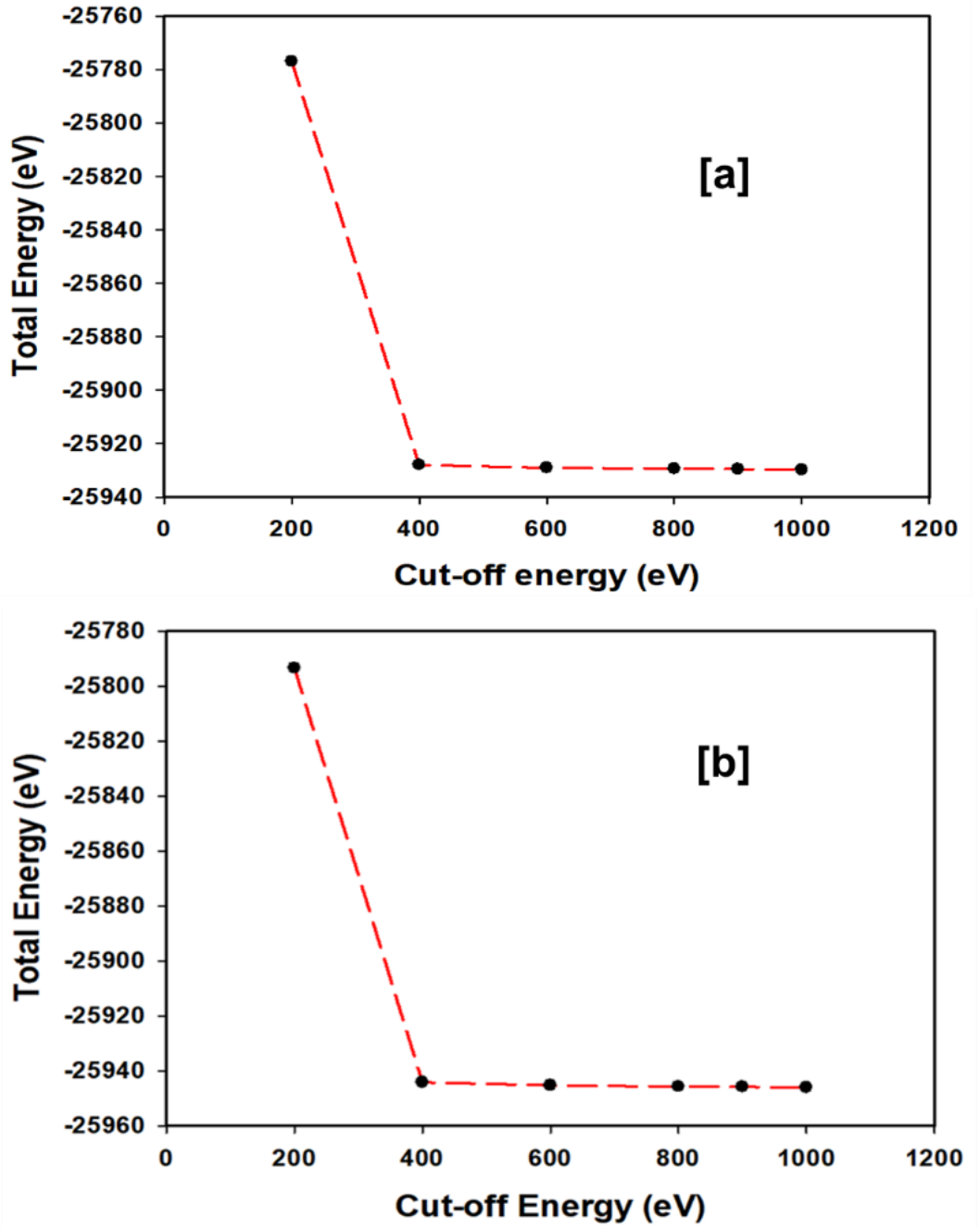

Figure 3. 2: Total energy and cut-off energy plot for (a) non-spin and spin polarised (b) $LiMn_2O_4$ spinel structure. An infinitesimal change in the total energy is noted from the cut-off energy of 400 eV.

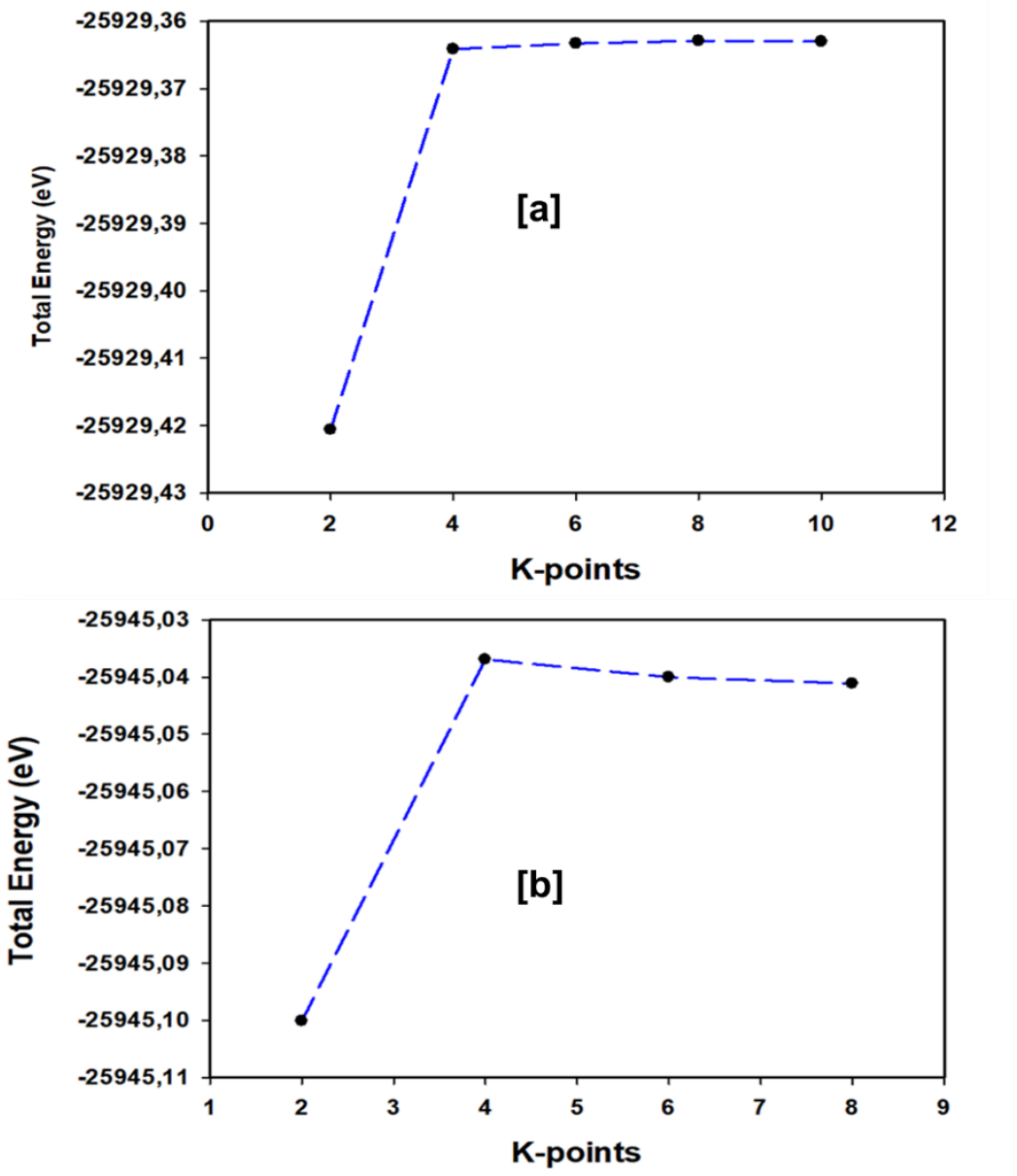

Figure 3. 3: Total energy and cut-off energy plot for (a) non-spin and spin polarised (b) k-mesh convergence test. 1, 2, 3 etc. in the x-axis denotes 111, 222, 333 k-points, respectively. A minimal decrease in the total energy of $LiMn_2O_4$ is observed from 4x4x4 k-mesh represented by 4.

3.3 Structural properties

Table 1 shows the structural properties of spinel structures studied in this work. First-principles DFT calculations have been performed to optimise the geometry of the Li-Mn-O spinel structures and resulted in cubic Li-Mn-O spinel structures with a space group of Fd-3m. The lattice parameters of the non-spin polarised Mn_2O_4 are smaller than those of the $LiMn_2O_4$ and this is consistent with the noted trend in literature [173, 180]. Lattice parameters of the spin polarised Mn_2O_4 and $LiMn_2O_4$ are 8.305 and

8.298, respectively which shows a different trend from the latter. The lattice parameters of spin polarised $LiMn_2O_4$ are closer to experimental values than the lattice parameters of the non-spin polarised $LiMn_2O_4$ indicating that the spin polarised calculation can give more profound results of $LiMn_2O_4$ than the non-spin polarised calculations. The Mn_2O_4 structure is well described by the non-spin polarised calculations. Since the non-spin polarised calculations results in lattice parameters that are closer to the experimental value than the spin polarised calculations for the Mn_2O_4 structure as indicated in table 3.1. A cubic $Li_2Mn_2O_4$ spinel was obtained which is different from the experimental observed tetragonal structure. The volumes of the spinel structures in questions were also calculated. The volume of the spin polarised $LiMn_2O_4$ and $Li_2Mn_2O_4$ show good agreement with the experimental values. The volume of the non-spin polarised Mn_2O_4 is in line with the experimental value than the volume of the spin polarised.

Table 3. 1: Structural properties of spin and non-spin polarised Fd-3m cubic Mn_2O_4, $LiMn_2O_4$ and $Li_2Mn_2O_4$ spinel structures. Volume is per formula unit. Exp represents the column for corresponding experimental results.

	Structure	Non-spin polarised	Spin polarised	Exp
Lattice parameters (Å)	Mn_2O_4	8.169	8.305	8.03 [173]
Volume (Å^3)		68.15	71.60	66.36 [181]
Lattice parameters (Å)	$LiMn_2O_4$	8.175	8.298	8.248 [182]
Volume (Å^3)		68.28	71.43	70.15 [183]
Lattice parameters (Å)	$Li_2Mn_2O_4$	8.151	8.231	7.84 [184]
Volume (Å^3)		67.68	69.70	69.89 [185]

3.4 Density of states (DOS) and electronic band structure analysis

This section provides a brief discussion on the density of states of spin polarised and non-spin polarised Mn_2O_4, $LiMn_2O_4$ and $Li_2Mn_2O_4$ spinel structures. The changes in the electronic structure of spinel as a function of lithium concentration will be investigated which are of fundamental importance as they determine a material's physical and chemical properties, i.e. conductivity. The total and partial density of states for non-spin and spin polarised structures have been calculated. In order to obtain more explicit information on the contribution of magnetic moments on the electronic structural changes of the Li-Mn-O spinel structures, minority and majority density of states for the spin polarised structures were also examined.

3.4.1 Non-spin polarised DOS electronic structure calculation

The electronic structure of the non-spin polarised Mn_2O_4 cubic spinel is examined. Figure 3.4 shows the total and partial density of states (DOS) for non-spin polarised Mn_2O_4 with the Fermi level represented by zero energy. The plotted DOS are in the energy range between -21 eV and 21 eV, which captures states that are occupied by valence electrons as they are responsible for physical and chemical properties of the material. Consequently, the calculated total DOS for the non-spin polarised Mn_2O_4 spinel structure denoted by figure 3.4 (a), shows that this material exhibit a metallic behaviour. This can be seen from the overlapping valence band and conduction band as illustrated in the figure. The valence band and the conduction band are denoted by total DOS peak between -1.1 eV and 1.2 eV with DOS of approximately 94 1/eV. Atomic contributions to the metallic nature of this material are captured by the DOS depicted in figure 3.4 (b-c), wherein, the Mn 3d states are the most occupied states in the valence band and a few of the O 2p states are observed in the valence band, which indicates that the metallic behaviour of this material stems mostly from the Mn 3d transition metal orbitals. The non-bonding peak located between -20 and -17.1 eV is dominated by the O 2s orbitals with DOS which are approximately 80 1/eV as it can be seen in figure 3.4 (b). Furthermore, the contribution of Mn 3d states is negligible in the above mentioned non-bonding peak. The hybridisation of Mn-O is depicted by the

peak between -8 and -2 eV near the Fermi level, with the O 2p orbital showing the most contribution and Mn 3d orbital also showing significant contribution.

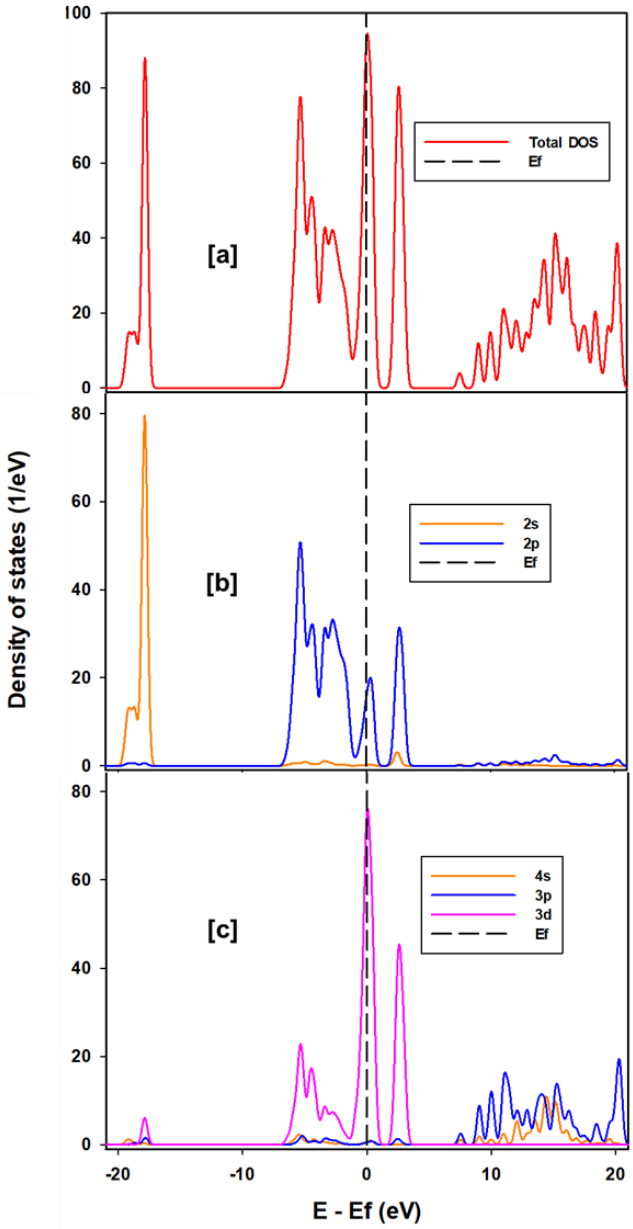

Figure 3. 4: Total and partial DOS for non-spin polarised Mn_2O_4. The dotted line represents the Fermi level.

Figure 3.5 shows the total and partial DOS for non-spin polarised $LiMn_2O_4$ spinel structure from which we can infer that the material exhibit a metallic behaviour. This can be seen from the Fermi level which cuts the peak between -1.5 and -1.0 eV in the middle. Figure 3.5 (b-c) shows atomic contributions to the plotted total DOS. The Mn 3d orbitals contribute significantly at the Fermi level. The contribution of lithium atoms in the energy range between -21 and 1 eV is negligible. Furthermore, the O 2s and O 2p states are dominant in the DOS peaks located between -21 and -17.4 eV and -6.8

and 0.9 eV, respectively. Moreover, a considerable contribution of the Mn 3d states on the peak situated between -21 and -17.4 eV is observed. Hence, the electronic structure of $LiMn_2O_4$ is similar to the electronic structure of the Mn_2O_4 spinel structure.

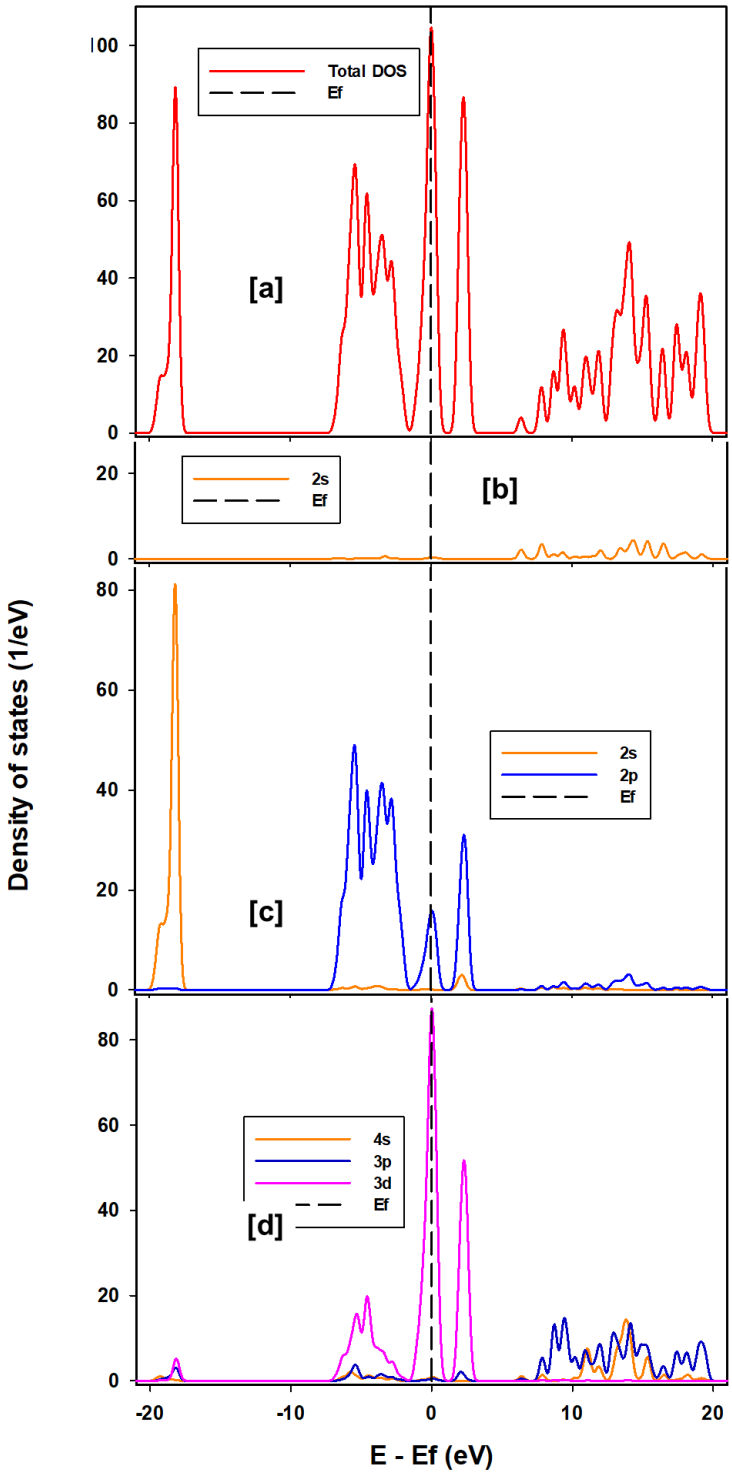

Figure 3. 5: Calculated total and partial DOS for non-spin polarised $LiMn_2O_4$. The dotted line represents the Fermi level.

The non-spin polarised $LiMn_2O_4$ spinel structure DOS calculated in this work are compared with the DOS of $LiMn_2O_4$ spinel structure from literature calculated by H.

Berg, et al [186] as illustrated in figure 3.6 below. Consequently, from both DOS plots illustrated in the figure, a metallic behaviour is observed which is indicated by an overlap of the valence band and the conduction band. Furthermore, a similar DOS shape is also observed in the plots. Moreover, the peak indicating the Mn-O hybridisation is located approximately between -7.1 and -1.5 eV on both plots. This demonstrates good agreement between the DOS calculated in this work and the DOS calculated by H. Berg and co-workers [186].

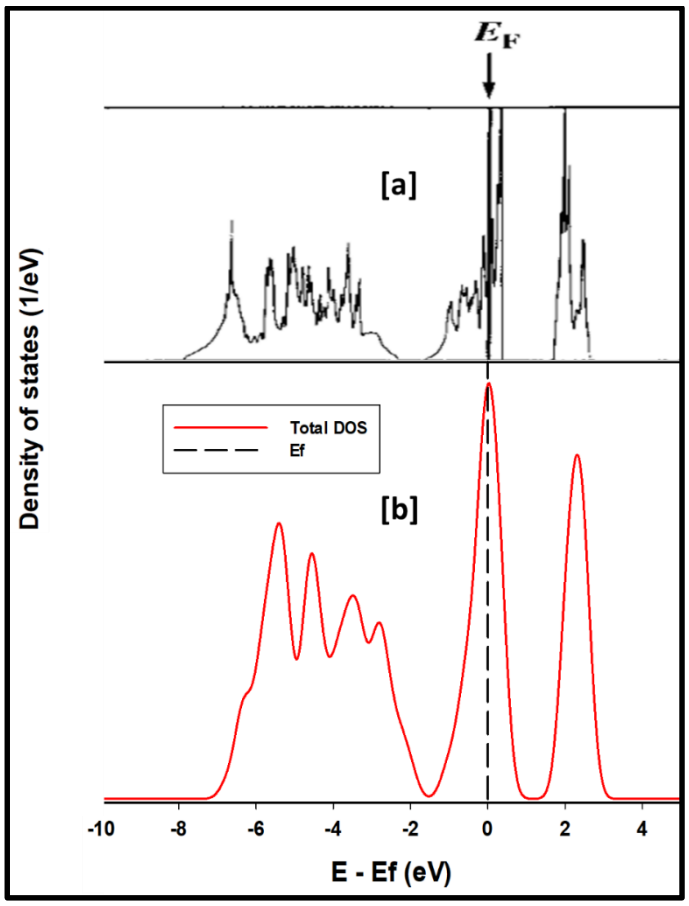

Figure 3. 6: Comparison of (a) non-spin polarised $LiMn_2O_4$ DOS calculated in this work and $LiMn_2O_4$ DOS calculated by H. Berg, et al. [186].

The electronic structure of the non-spin polarised $Li_2Mn_2O_4$ spinel is also examined from the plotted DOS illustrated in figure 3.7 below. The total and partial DOS have been plotted to give explicit information on the electronic structure of this material. An intense non-bonding peak dominated by the O 2s states, is noted from the partial DOS and is observed around -21 and -18 eV in the total DOS. A negligible contribution from the Li 2s states is observed in the energy range between -21 and 0 eV. Similar to the non-spin polarised Mn_2O_4 and $LiMn_2O_4$ DOS, the hybridisation of Mn-O in the $Li_2Mn_2O_4$ is represented by the DOS peak located between -7.7 and -1.9 eV in the total DOS.

This is can be observed from the partial DOS in the figure. Furthermore, from the resulting atomic contribution denoted by total DOS we can conclude that the material exhibit a metallic behaviour which is indicated by the overlapping valence band and conduction band.

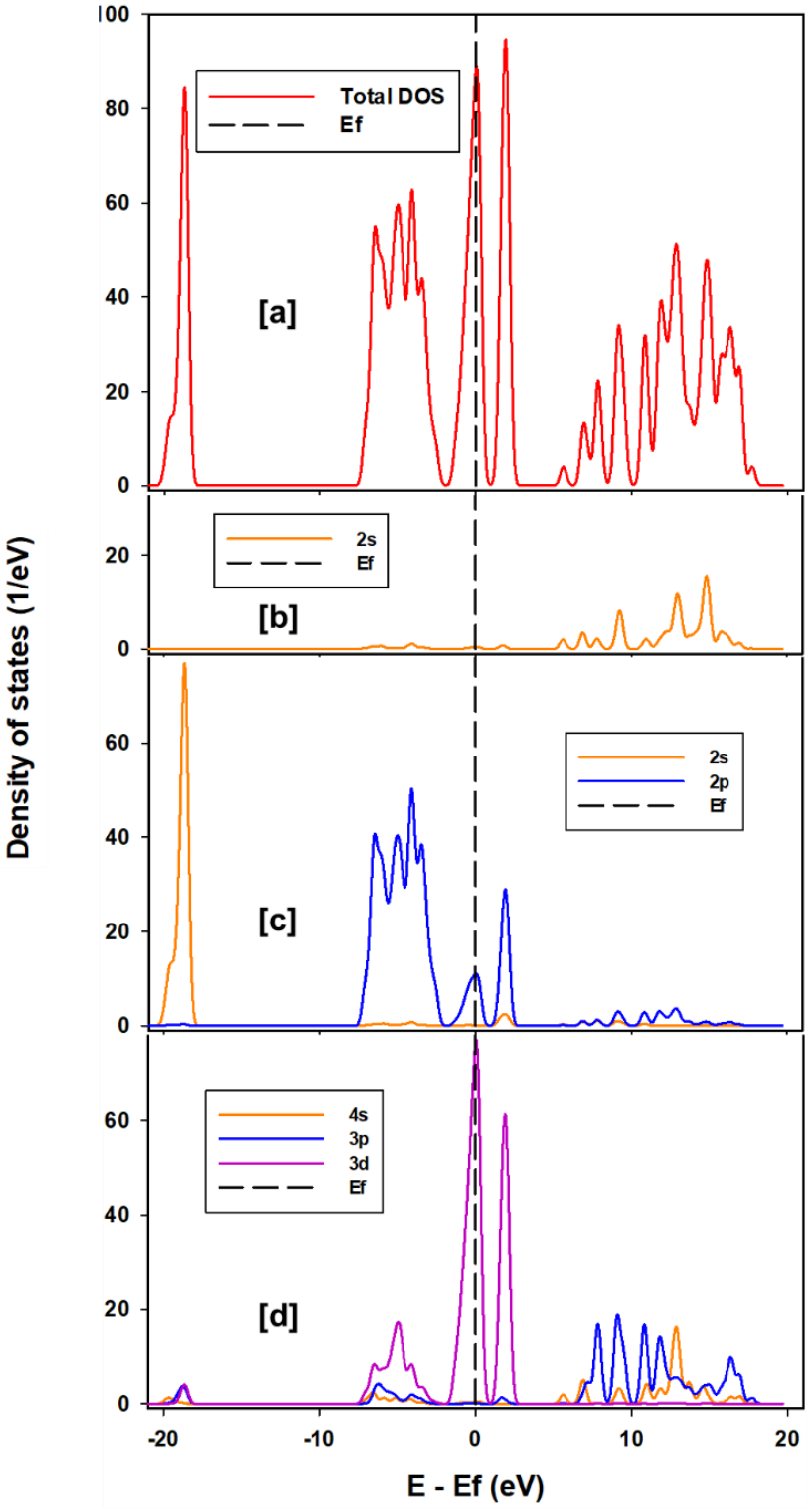

Figure 3. 7: Total and partial density of states (DOS) for the non-spin polarised $Li_2Mn_2O_4$. The Fermi level is at zero.

Figure 3.8 shows the comparison of the total DOS calculated in this work with DOS obtained from literature calculated by H. Berg and co-workers [186]. In the energy range of -10 and 4 eV, wherein, three characteristic peaks having the same general shape are observed in both plots. A metallic nature of the non-spin $LiMn_2O_4$ can be inferred from both plots. Hence, the DOS of $LiMn_2O_4$ calculated in this work resemble that calculated by H. Berg and co-workers [186].

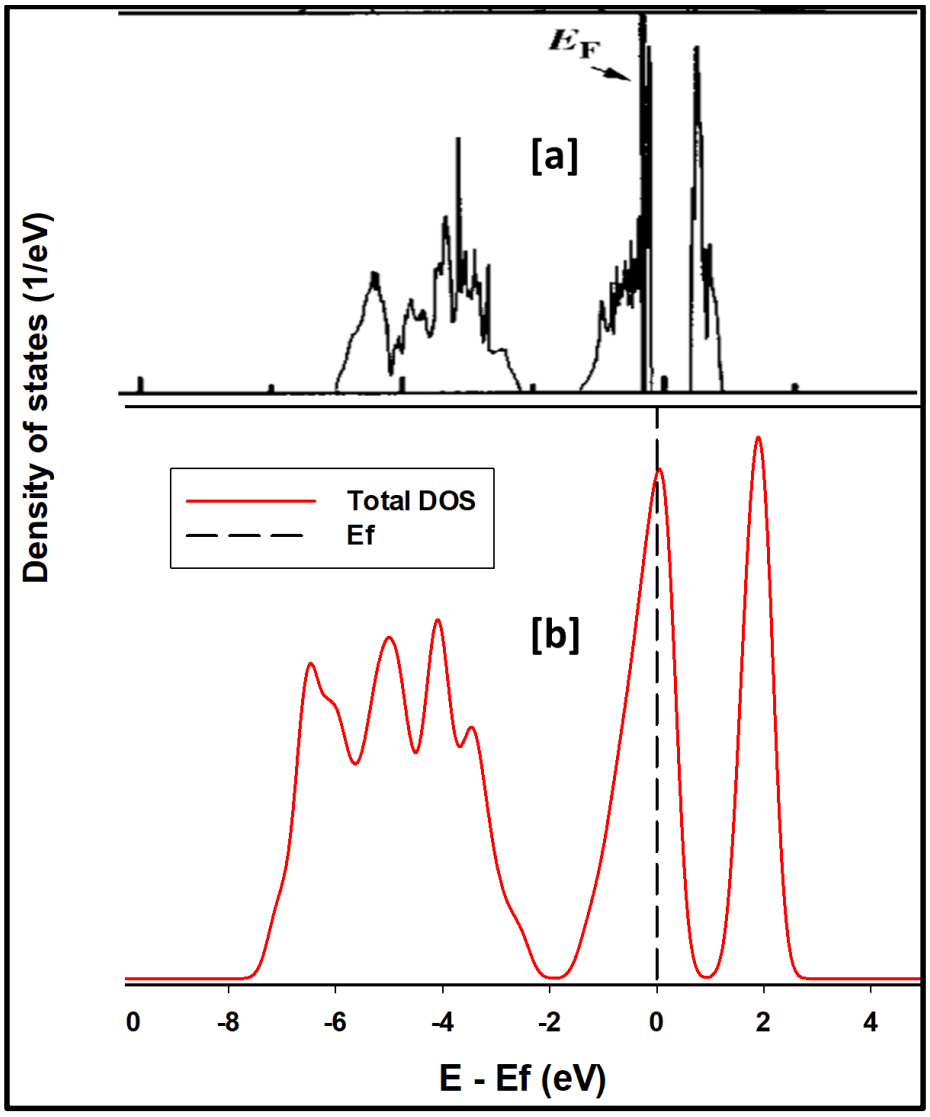

Figure 3. 8: Comparison of the total density of states of $Li_2Mn_2O_4$ from (a) other experiments (a) [186] and (b) from this work.

The electronic structure of the $Li_xMn_2O_4$ spinel was further unravelled by the electronic band structures illustrated in figure 3.9. Different energy bands from which electrons can exist are indicated by the blue lines and are captured in the energy range between -1.5 and 1.5 eV. The figure shows the electronic band structure of Mn_2O_4, $LiMn_2O_4$ and $Li_2Mn_2O_4$, from which we observed a metallic behaviour indicated by the

overlapping of the valence band and the conduction band. This is in line with the calculated DOS in figure 3.4 (a), 3.5 (a) and 3.7 (a). A shift in the Fermi level with lithium concentration is observed from the calculated band structures.

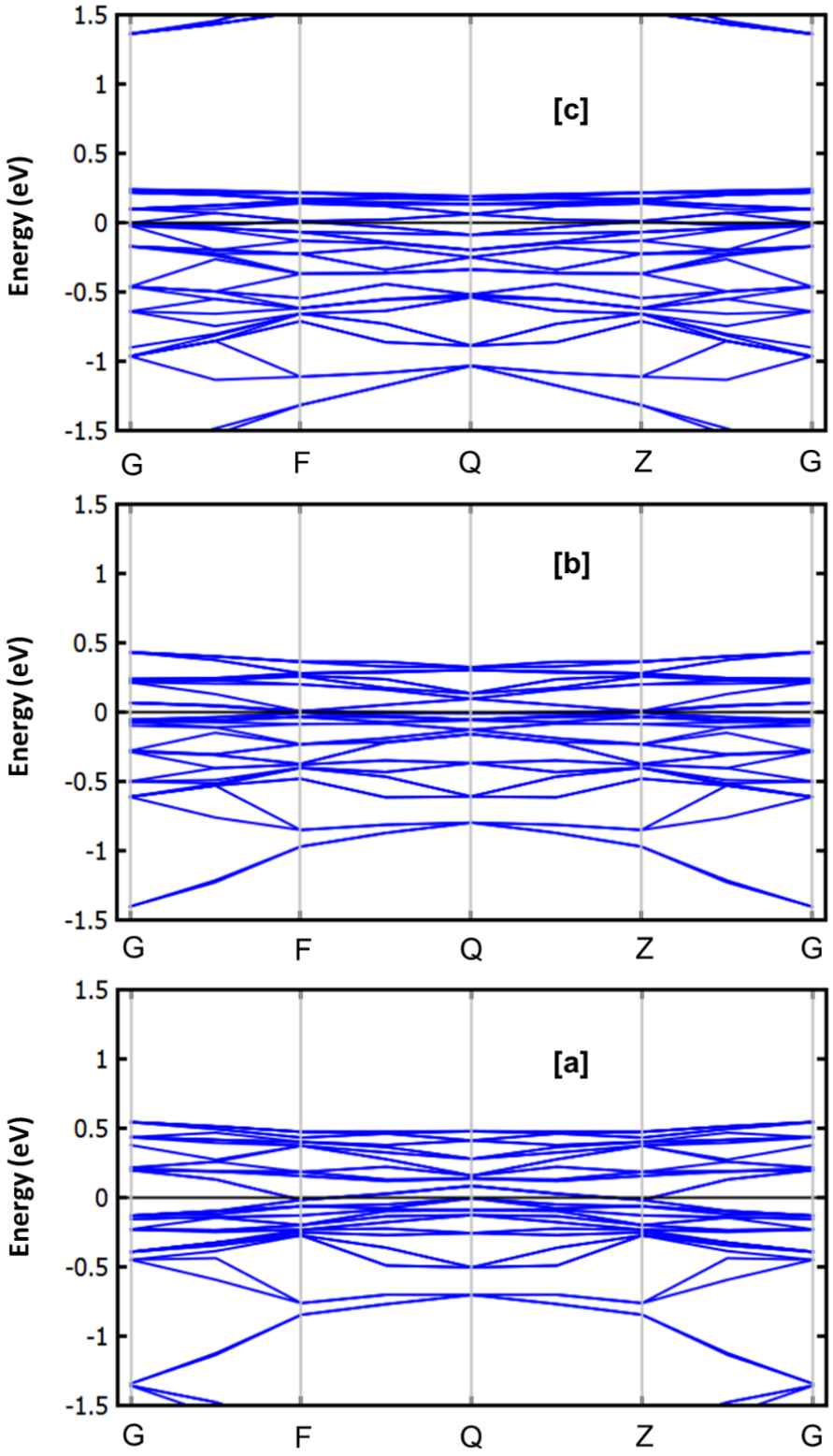

Figure 3. 9: Illustration of electronic band structure of the non-spin (a) Mn_2O_4, (b) $LiMn_2O_4$ and (c) $Li_2Mn_2O_4$.

3.4.2 Spin polarised DOS electronic structure calculation: Mn_2O_4, $LiMn_2O_4$ and $Li_2Mn_2O_4$

Spin polarised electronic DOS calculations and electronic band structures for Mn_2O_4, $LiMn_2O_4$ and $Li_2Mn_2O_4$ have been performed. Figure 3.10 shows the total and partial DOS for the spin polarised Mn_2O_4 spinel structure. Semi-conducting behaviour is observed from the calculated DOS, which is evinced by a band gap of ~0.65 eV in the total DOS presented in the figure. Furthermore, the Fermi level lies on a sharply decreasing curve denoting the valence band of the material which is almost completely filled. Moreover, the conduction band lies above the Fermi level which indicates that it is unoccupied. The O 2p and Mn 3d states denoted by the total DOS peak located between -6 eV and 0.5 eV represents the Mn-O hybridisation. Consequently, the O 2p states are dominant in this energy region. Similar to the non-spin polarised calculated spinel (Mn_2O_4, $LiMn_2O_4$ and $Li_2Mn_2O_4$) DOS above, the non-bonding peak situated between -18 and -16 eV in the total DOS of Mn_2O_4 is mainly due to the O 2s states.

The calculated total and partial DOS for the spin polarised $LiMn_2O_4$ spinel structure illustrated in figure 3.11 below shows metallic behaviour which is evinced by the overlapping of the valence band and conduction band. The Fermi level lies on an increasing curve denoting the O 2p and Mn 3d orbitals which are located between -0.8 and 1.6 eV. The majority states in the valence band and conduction band are from the Mn 3d states. Analogous to the DOS of the non-spin polarised $LiMn_2O_4$, the contribution of Li 2s is negligible in the energy range between -21 and 0 eV. Moreover, the O 2p orbitals are dominant in the peak located between -8 and -0.8 eV in the total DOS which represent the chemical bond between manganese and oxygen in the spinel structure.

Figure 3.12 presents the total and partial DOS of spin polarised $Li_2Mn_2O_4$, wherein, a similar electronic structure to the spin polarised $LiMn_2O_4$ is observed. The total and partial DOS plot shows metallic behaviour indicated by the overlapping of the valence band and conduction band. Moreover, the Fermi level lies on an increasing DOS peak denoting the O 2p and Mn 3d states, which is similar to the calculated DOS of the spin polarised $LiMn_2O_4$. Furthermore, the contribution of the Li 2s orbital in the energy range between -21 and 0 eV is negligible. An intense non-bonding peak located approximately between -21 eV and -18 eV originate from the O 2s orbital. A strong hybridisation of the O 2p orbital and Mn 3d orbital denoting the bond between oxygen

atoms and manganese is noted around -8 eV to 2.8 eV. Hence, the electronic structures of the spin polarised $LiMn_2O_4$ and $Li_2Mn_2O_4$ spinel structure shows similar features.

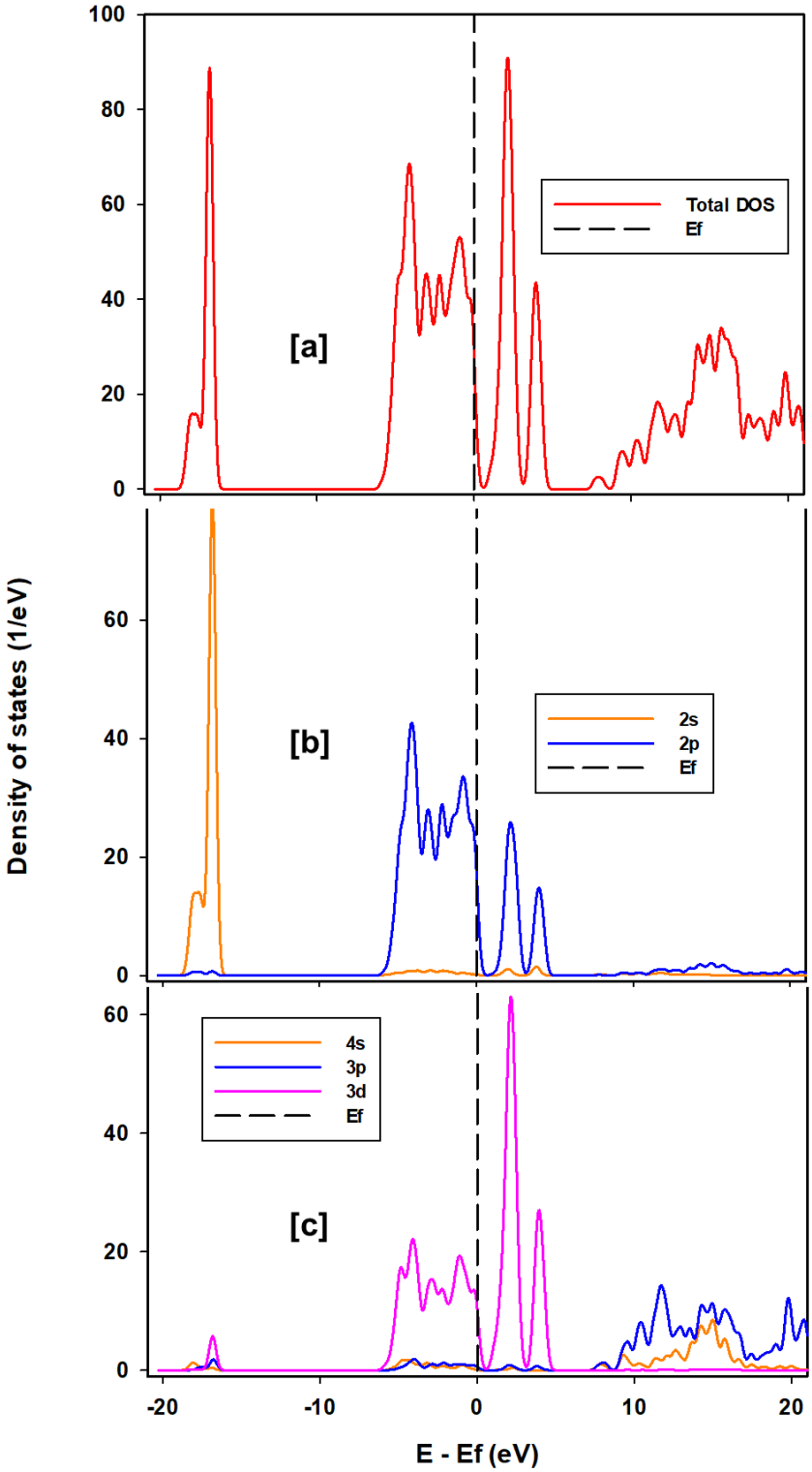

Figure 3. 10: Total and partial DOS for the spin polarised cubic spinel Mn_2O_4. (a) Represent the total DOS, (b) Represents contribution to the total DOS by O atoms and (c) represents the contribution to the total DOS by Mn atoms.

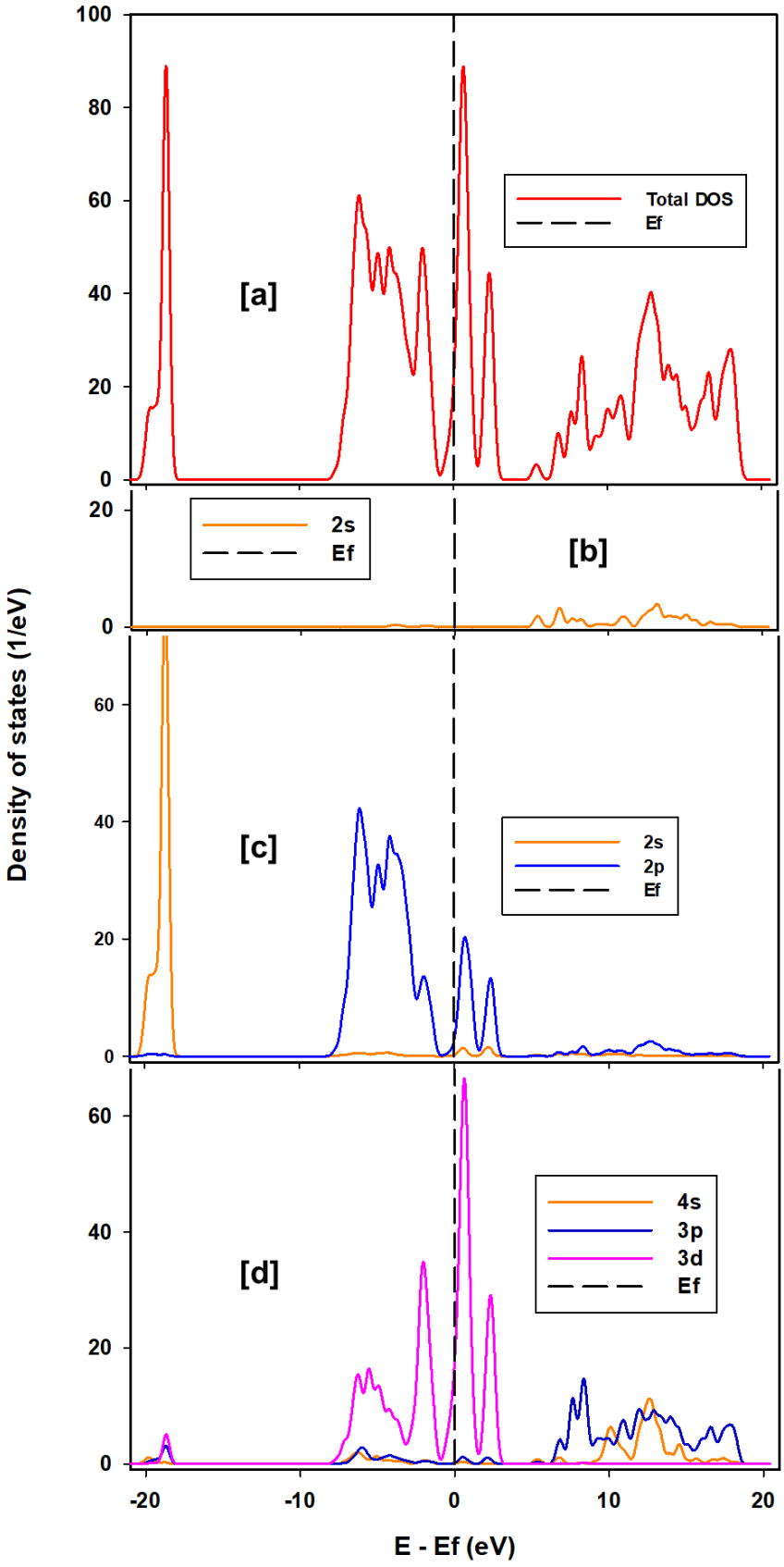

Figure 3. 11: Total and partial density of states (DOS) for spin polarised cubic spinel $LiMn_2O_4$. (a) Total DOS, (b) contribution from Li atoms, (c) depicts contribution from O atoms and (d) depicts contribution from Mn atoms.

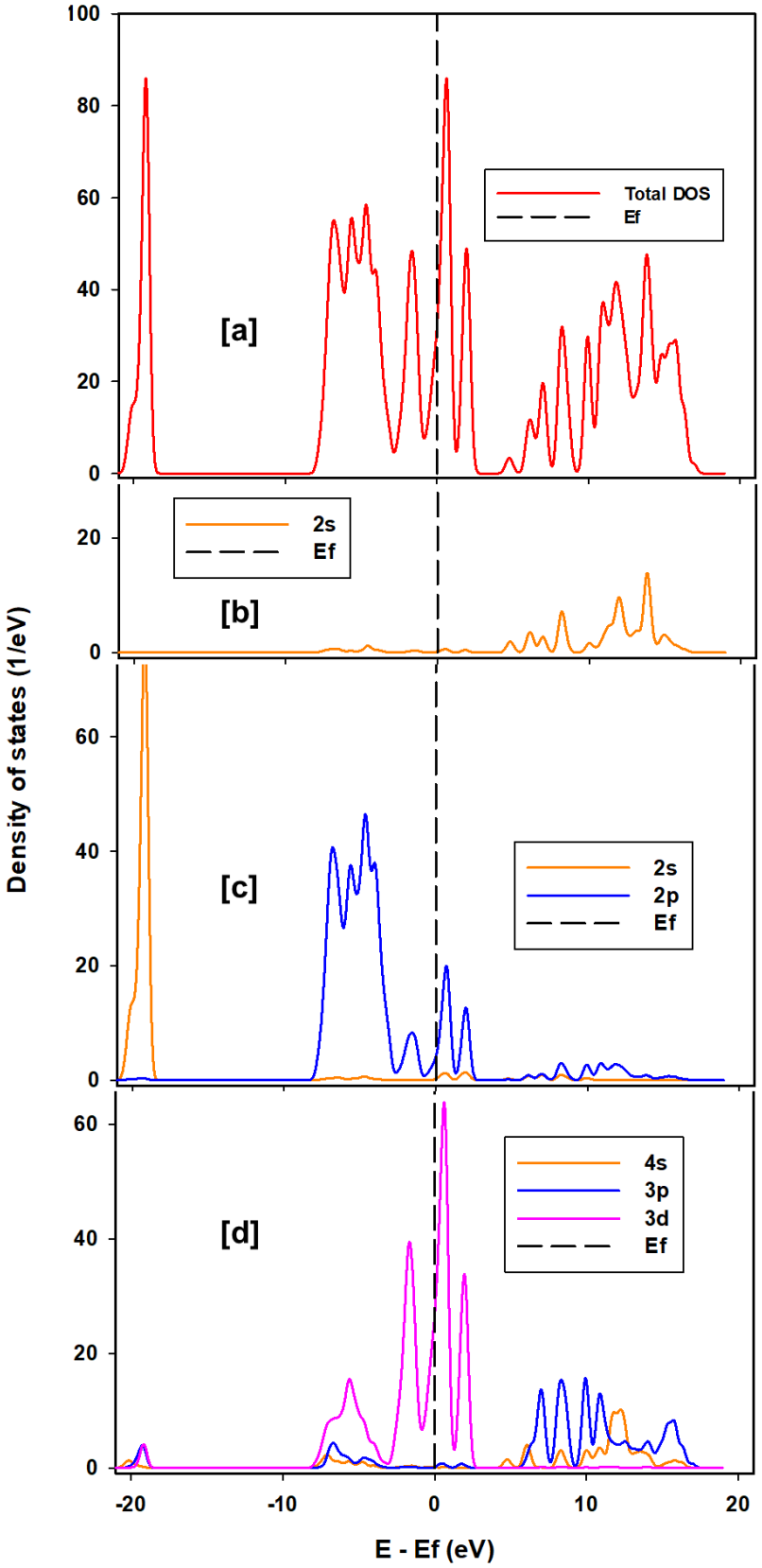

Figure 3. 12: Total and partial density of states (DOS) for spin polarised cubic spinel $Li_2Mn_2O_4$. (a) Total DOS, (b) depicts contribution from Li atoms, (c) depicts contribution from O atoms and (d) depicts contribution from Mn atoms.

The total spin polarised DOS of Mn_2O_4, $LiMn_2O_4$ and $Li_2Mn_2O_4$ are shown in figure 3.13 below to illustrate the effect of lithiation on the electronic structure of these compounds. Figure 13.13 (a) shows the semiconducting Mn_2O_4 spinel structure, figure 13.13 (b-c) shows the conducting $LiMn_2O_4$ and $Li_2Mn_2O_4$ spinel structures. The same general shape is observed in the total DOS $LiMn_2O_4$ and $Li_2Mn_2O_4$ in the energy range between -8 and 5 eV which is different from Mn_2O_4. A peak shift into lower energy level is noted, which is indicated by the peak located between -0.80 and -2.6 in $LiMn_2O_4$ and between -8.3 and -2.8 in $Li_2Mn_2O_4$. The two peaks above the Fermi level are located between 0.5 and 4.7 eV, -0.9 and 3.1 eV, and -1.0 and 2.6 eV in Mn_2O_4, $LiMn_2O_4$ and $Li_2Mn_2O_4$, respectively, which indicates a peak shift into lower energy levels.

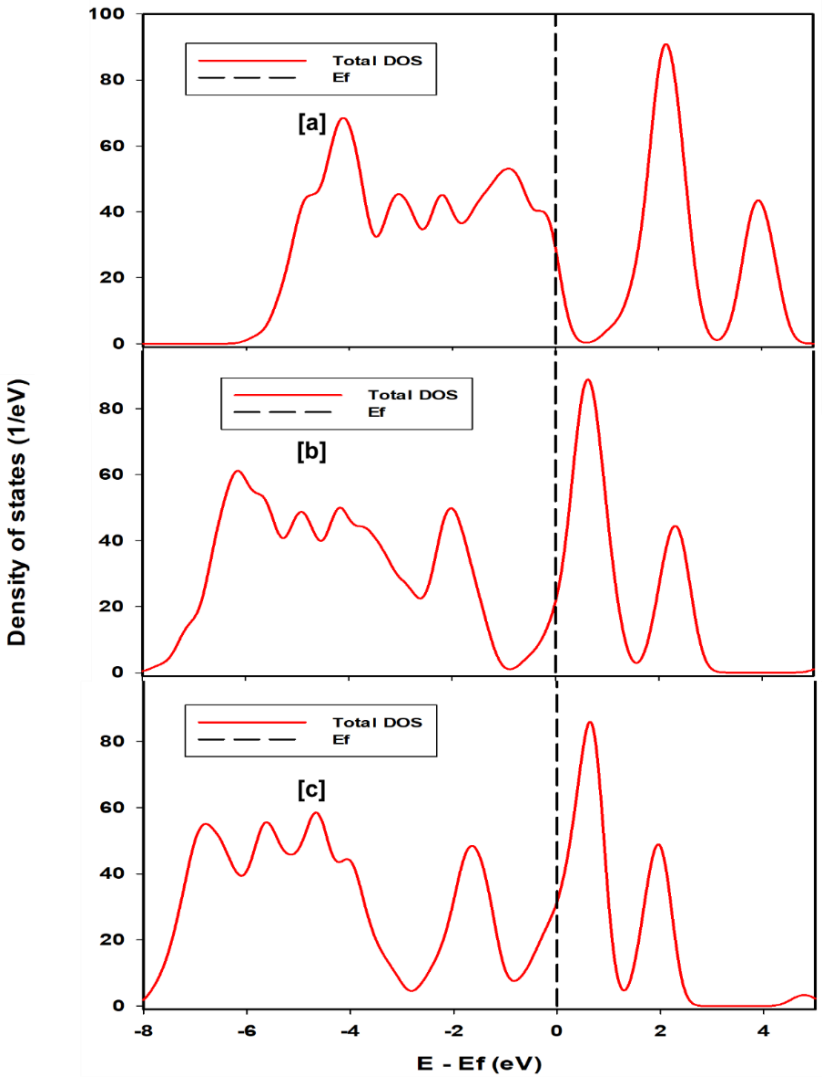

Figure 3. 13: Total density of states curves of spin polarised (a) cubic spinel Mn_2O_4, (b) cubic spinel $LiMn_2O_4$ and (c) cubic spinel $Li_2Mn_2O_4$. This figure illustrates the effect of lithiation on electronic properties.

The projected total spin-up and spin-down DOS in figure 13.14 gives explicit details on the contribution of electrons with spin-up and spin-down configurations to the electronic structure of the magnetic spinel structures. The spin-up states in the valence band of the Mn_2O_4 are dominant and nearly completely filled. The t_{2g} and e_g orbitals for the spin-down electronic configurations are empty together with the e_g orbitals for the spin-up electronic configurations. In both $LiMn_2O_4$ and $Li_2Mn_2O_4$, the high energy e_g orbitals are empty for both spin-up and spin-down electronic configurations whilst the t_{2g} orbitals with spin-up electrons are fully occupied for electrons with spin-up electronic configurations. Furthermore, the t_{2g} orbitals with spin-down electronic configurations are partially filled for electrons with spin down electronic configurations.

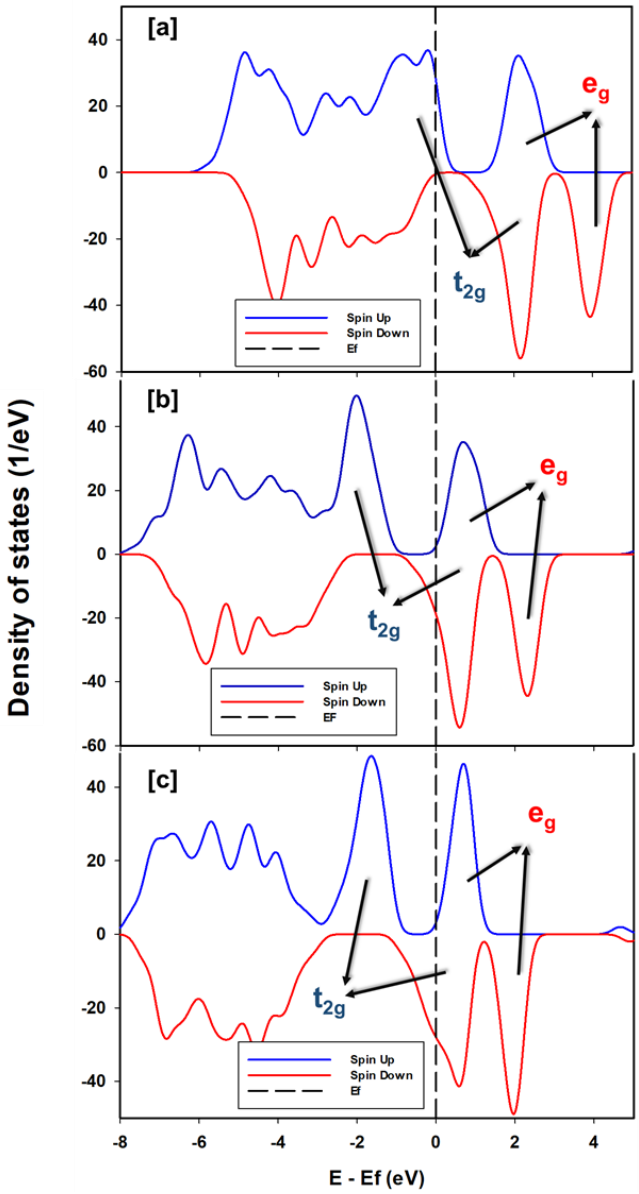

Figure 3. 14: Spin-up and spin-down total density of states for spin polarised (a) cubic spinel Mn_2O_4, (b) cubic spinel $LiMn_2O_4$ and (c) cubic spinel $Li_2Mn_2O_4$.

Electronic band structures for spin polarised Mn_2O_4, $LiMn_2O_4$ and $Li_2Mn_2O_4$ have been calculated to further unravel their magnetic electronic properties. Since conduction properties are attributed to high energy bands only bands between -21 eV to 21 eV are shown for the Mn_2O_4 and bands between -45 eV to 21 eV are shown for the $LiMn_2O_4$ and $Li_2Mn_2O_4$ in figure 3.15 above. A bandgap of 0.746 eV between the valence band and the conduction band on the band structure of the Mn_2O_4 denoted by figure 3.15 (a) is observed, which circumstantiate the density of states depicted in figure 3.10a, 3.13a and 3.14a. A metallic behaviour is also observed in the band structures of $LiMn_2O_4$ and $Li_2Mn_2O_4$ which is in line with the calculated DOS in figure 3.13 (a) and (b).

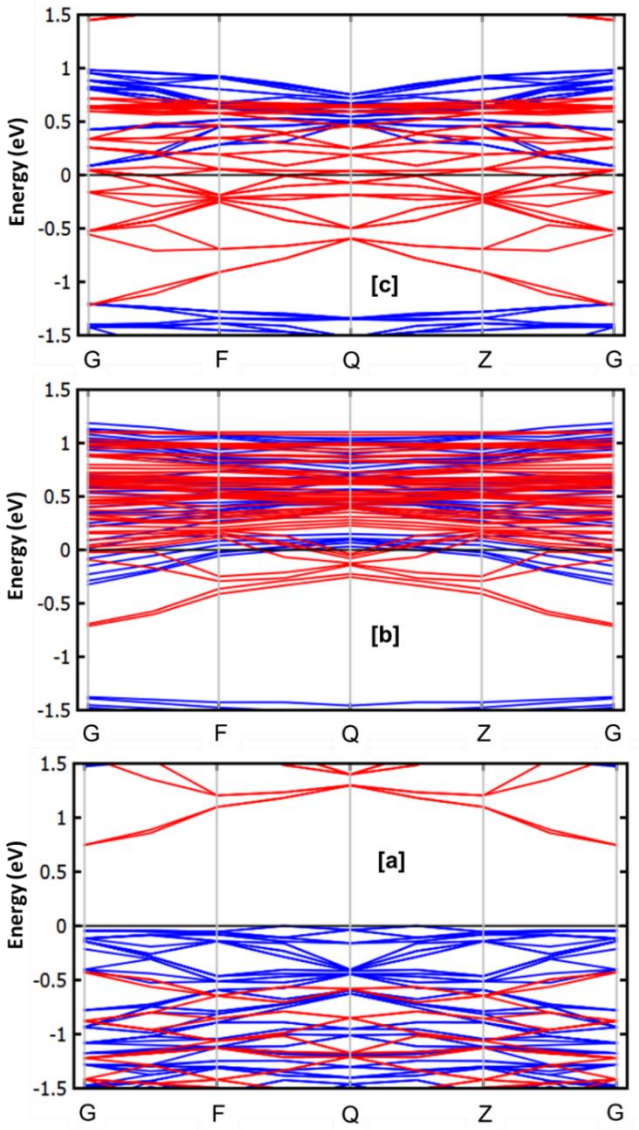

Figure 3. 15: Show the electronic band structure of spin polarised (a) Mn_2O_4, (b) $LiMn_2O_4$ and (c) $Li_2Mn_2O_4$. Blue lines represent spin-down bands and red lines represent spin-up bands.

3.5 Discussion

The non-spin polarised DOS and electronic band structures reveals good conducting properties which are in good accord with literature for the spinel structures studied in this chapter. The effect of lithiation on non-spin polarised spinel $LiMn_2O_4$ is noted by a peak shift towards the conduction band from Mn_2O_4 to $Li_2Mn_2O_4$. Moreover, this is evidenced by the peak located between -1.15 eV and 1.10 eV for Mn_2O_4, between -1.50 eV and 0.96 eV for $LiMn_2O_4$ and -1.84 eV and 0.88 eV for $Li_2Mn_2O_4$ in figure 3.4 (a), 3.5 (a) and 3.7 (a). Accordingly, this indicates that the empty states in the Mn_2O_4 are occupied as lithium atoms are intercalated into this structure. The valence and conduction band shift to lower energy levels suggest that the amount of energy required for an electron to hop into the conduction band becomes minimal with lithiation. Moreover, the electronic band structures indicate that the conduction band becomes filled as lithium-ions are intercalated, which is also indicated by the Fermi level shift towards the conduction band as illustrated in figure 3.9.

The DOS of the magnetic Li-Mn-O spinel structures in figure 3.10, 3.11, 3.12 and 3.13 exhibit different electronic properties to the non-magnetic DOS in figure 3.4 (a), 3.5 (a) and 3.7 (a) above. The valence band of the Mn_2O_4 spinel structure is almost full and a bandgap of ~0.65 eV is observed. This alludes that for the electrons in the valence band to jump to the conduction band and become “free electrons” they require energy which is greater than ~0.65 eV. Ouyang C.Y and colleagues [187] found a bandgap of about 1 eV for this material. Furthermore, conduction takes place in the peak between ~0.8 eV and ~3.0 eV as illustrated in figure 3.10 (a) and 3.13 (a). The Fermi level lies above a pseudogap of ~0.17 eV which is between the two peaks located between ~-2.6 eV and -1.05 eV, and -0.35 eV and 1.47 eV on the DOS of $LiMn_2O_4$ shown in figure 3.11 (b) and 3.13 (b). An overlap between the valence band and the conduction band is noted which indicates good conducting properties on both $LiMn_2O_4$ and $Li_2Mn_2O_4$ spinel structures.

The spin-up and spin-down DOS in figure 3.14 gives explicit information on the conduction of the spinel structures studied in this work. The e_g orbitals are empty for both the spin-up and spin-down states which substantiate the presence of only Mn^{4+} manganese ions in the Mn_2O_4 spinel structure. Upon lithiation, some of the spin-down states of the t_{2g} orbitals and the spin-up states of the e_g orbitals are occupied demonstrating an average manganese valence of 3.5^+. This is in good accordance

with the findings of Bo Xu and Shirley Meng [188]. The highest occupied states at the Fermi level of $LiMn_2O_4$ and Mn_2O_4 are the spin-down states which is in line with the electronic band structures shown in figure 3.15

CHAPTER 4

Simulating the discharge process of Li-Mn-O layered-spinel composite nanoarchitectures.

In this chapter, a molecular dynamics simulation is used to model Li-Mn-O layered-spinel (LS) composite nanoarchitectures depicting different stages of the discharge process. The simulated Li-Mn-O LS composite nanoarchitectures enables a thorough investigation of structural changes that influence electrochemical performance. The generation of the Li-Mn-O LS nanoarchitectures using the simulated amorphisation and recrystallisation technique [73] is captured. The simulated recrystallisation is essential for introducing complex structural features that are observed experimentally, such as grain boundaries, dislocations, point defects, co-existing crystal structures. Moreover, this gives the modelled models a commensurable significance with materials from experiments. Structural analysis of the discharge process will be carried out using atomic level snapshots, radial distribution functions (RDFs) and XRD patterns.

4.1 Method

Simulations in this chapter are carried out using the molecular dynamics (MD) DLPOLY simulation code [189], in which the model is represented infinitely in space by a three-dimensional periodic boundary conditions. The Li-Mn-O atoms of the systems studied in this work interact via the long-range Coulomb interactions and short-range parameterised interactions based on the Born Model of the ionic solids [190]. The interatomic potentials used are obtained from literature [75]. Atomic configurations used to prepare the ideal spinel 4x4x4 $LiMn_2O_4$ supercell for the simulated synthesis with minimum energy were computed with the METADISE [191] code. The Li-Mn-O LS nanocomposites are synthesised using the simulated amorphisation and recrystallisation (A&R) [73] techniques.

Radial distribution functions (RDFs) are employed to determine the distribution of atoms in the nanospheres in order to deduce their amorphous and crystalline states. Material studio program is also used to visualize the atomic arrangements of the synthesised nanospheres. The crystal structures formed after recrystallisation are

characterised using the XRD patterns. The process of nucleation and crystal growth during the simulated amorphisation and recrystallisation is monitored through a plot of configuration energy graphs against time.

4.1.1 Input structures

The METADISE [191] code was used to generate the optimised $LiMn_2O_4$ supercell (figure 4.1 b), which is formed by an agglomeration of conventional bulk spinel $LiMn_2O_4$ unit cells (figure 4.1 a). The $LiMn_2O_4$ supercell comprises of 512 lithium atoms, 1024 manganese atoms and 2048 oxygen atoms. In a process to model the Li-Mn-O LS nanocomposites observed experimentally, the 3584 atoms supercell is amorphised using the NVE ensemble. Electrochemical lithiation is performed using a lithium insertion program to generate Li-Mn-O LS nanocomposite with different lithium concentrations. The lithiated structures are then recrystallised using the NVT ensemble. A time per step of 0.0005 ps, steps of 500 000, equilibration of 5000, radius cutoff of 10 Å and Ewald precision of 1d-5 were used for amorphisation. For recrystallisation, 0.003 ps timesteps, 5 000 000 steps, equilibration of 5 000, radius cutoff of 10 Å, and 1d-2 Ewald precision were employed.

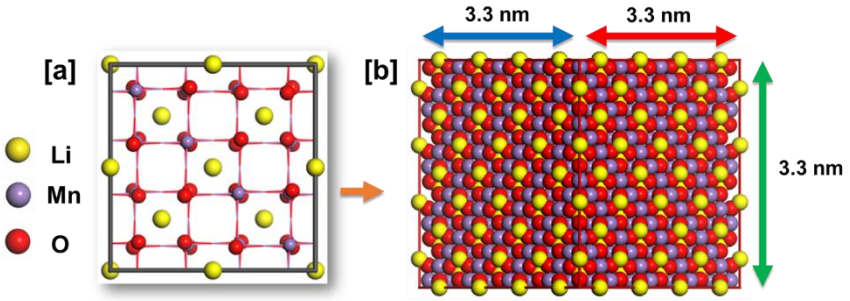

Figure 4. 1: The construction of the 3584 atoms $LiMn_2O_4$ supercell. (a) $LiMn_2O_4$ conventional unit cell and (b) a 3584 atoms $LiMn_2O_4$ supercell formed by the integrated conventional unit cells. Yellow sphere represents lithium atoms, blue spheres represents manganese atoms and red spheres represent oxygen atoms.

4.2 Simulated amorphisation

In this section, we discuss the molecular dynamics (MD) simulated amorphisation of a 3584 atoms spinel $LiMn_2O_4$ structure. The process is equivalent to the combustion in a combustion chamber of Liquid-phase flame spray pyrolysis which facilitates the formation of molten metal-oxide nanoparticles [192, 193]. Figure 4.2 below shows the

effect of temperature on the amorphisation process of a 3584 atoms bulk $LiMn_2O_4$ spinel structure. The atoms start vibrating about their lattice positions upon the applied temperature of 500K indicating an increase in kinetic energy of the system as captured by the microstate depicted by figure 4.2 (a). An increase in temperature from 500K to 1000K result in distortion of the cubic shape of the material as the movement of the atoms increases due to the increased kinetic energy. A temperature of 1500K was sufficient to amorphise the bulk $LiMn_2O_4$ supercell into a desired spherical shape. An increase in temperature from 1500K to 2000K ignites a rapid atomic movement in the 1500K Li-Mn-O nanosphere which results in a distortion of its spherical shape. The microstate depicted by the snapshot in figure 4.2 (c) is similar to the molten metal-oxide nanoparticles in [192, 193], which evince the success of the amorphisation process.

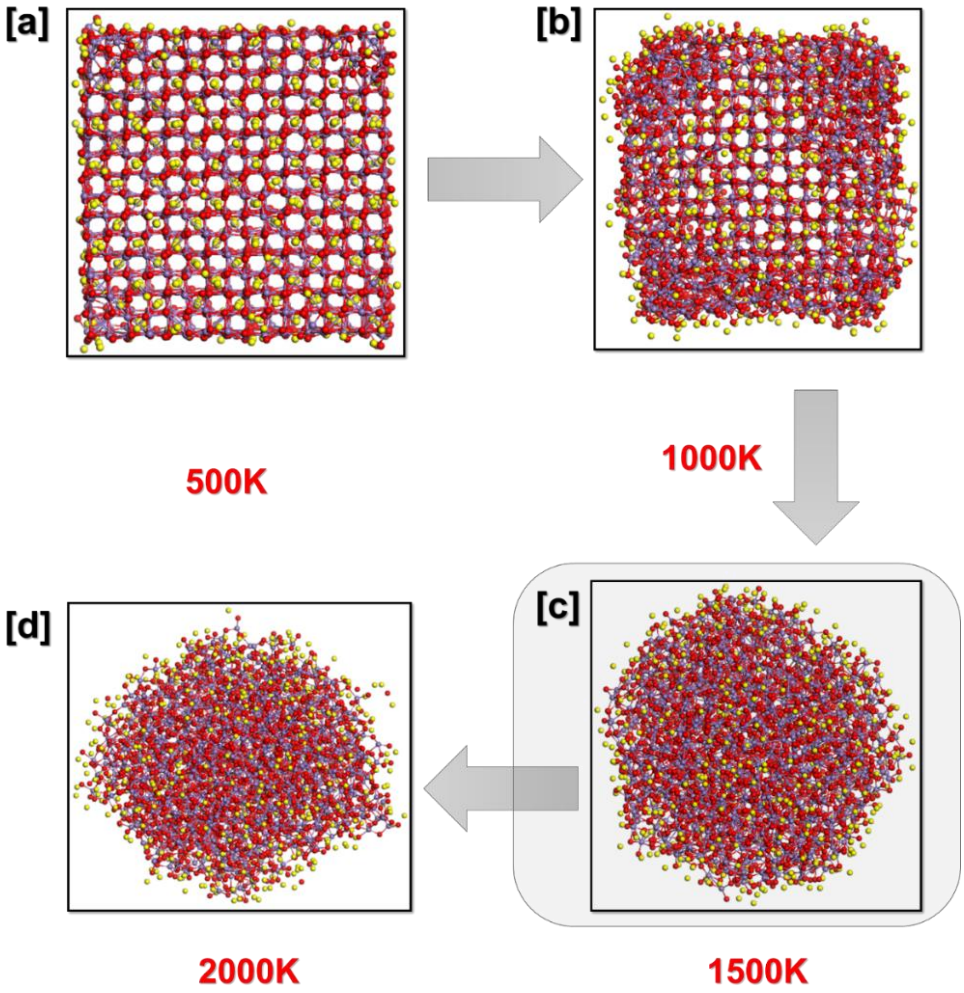

Figure 4. 2: Simulated amorphisation of a 3584 atoms $LiMn_2O_4$ at different temperatures. (a) 500K, (b) 1000 K, (c) 1500K and (d) 2000 K.

Figure 4.3 further illustrates the effect of temperature on the amorphisation of a 3584 atoms spinel $LiMn_2O_4$ supercell through RDF functions and atomic level snapshots. The radial distribution functions (RDFs) in figure 4.3 depicts the distribution of atoms within a radius of 10 Å around a given reference atom. The amorphous state of the desired Li-Mn-O nanosphere in figure 4.2 (c) is confirmed by broad RDF peaks as illustrated in figure 4.3 (c).

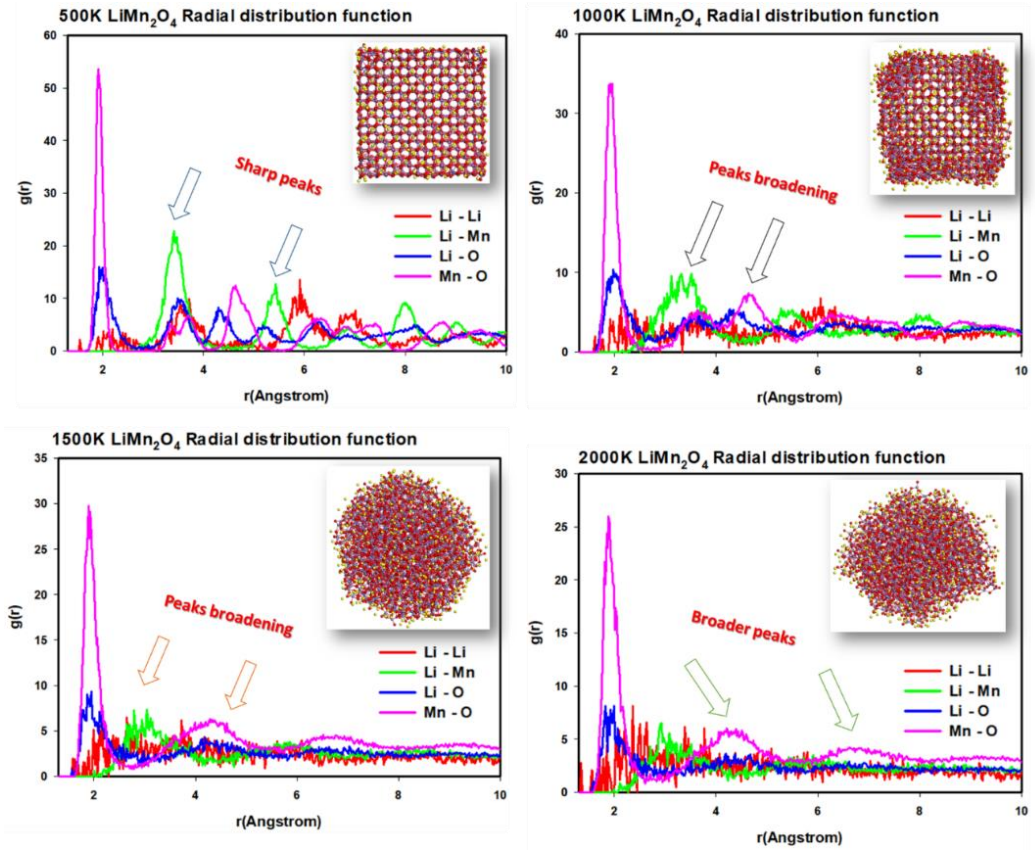

Figure 4. 3: Calculated Li-Li, Li-Mn, Li-O and Mn-O RDFs for amorphous $LiMn_2O_4$. The interatomic separation is measured in Å.

4.3. Simulated recrystallisation process

The simulated recrystallisation technique of lithiated Li-Mn-O composite nanoarchitectures is discussed. Furthermore, lithiation of the amorphous 3584 atoms Li-Mn-O nanosphere into different amorphous Li-Mn-O nanospheres depicting different stages of the discharge process is also discussed. The recrystallisation process is explored through RDF graphs, atomic level snapshots and configuration energy graphs. Li-Mn-O components formed after the recrystallisation process are characterised using XRDs and atomic level snapshots.

4.3.1 Li-intercalation from amorphous $LiMn_2O_4$ to amorphous $Li_2Mn_2O_4$

The amorphous $LiMn_2O_4$ nanosphere presented in figure 4.4 (a) was fully lithiated into amorphous $Li_2Mn_2O_4$ nanosphere as illustrated in figure 4.4. The inserted 512 lithium atoms are evenly distributed in the amorphous $LiMn_2O_4$ nanosphere following its spherical shape. The inserted lithium atoms occupy random vacant positions in the structure irrespective of the interatomic forces between the atoms. Figure 4.5 shows RDFs for the (a) amorphous $LiMn_2O_4$ nanosphere and the fully lithiated (b) amorphous $Li_2Mn_2O_4$, which demonstrates the distribution of Li atoms with respect to manganese (Li-Mn) atoms and O (Li-O) atoms. RDF peaks for the amorphous $Li_2Mn_2O_4$ nanosphere are less broad than the RDF peaks of the amorphous $LiMn_2O_4$. Moreover, this indicates high probability of finding lithium atoms with respect to manganese and oxygen atoms. Furthermore, at ~1.5 Å in the figure, a distinct RDF peak of the amorphous $Li_2Mn_2O_4$ is noted which indicates a high probability of finding close Li-Mn and Li-O interactions in the amorphous $Li_2Mn_2O_4$ structure than in the amorphous $LiMn_2O_4$ structure. RDF graphs of all the lithiated amorphous Li-Mn-O nanospheres are shown in figure 4.6 below. The “noise” Li-Li RDF peaks displayed in the figure decreases with lithium intercalation connoting an increasing in clustering of lithium atoms around the system. Li-Mn and Li-O peaks broaden with lithium intercalation indicating that the inserted lithium atoms increases disorder in the system. Mn-O RDF peaks are the same in all the amorphous Li-Mn-O nanospheres.

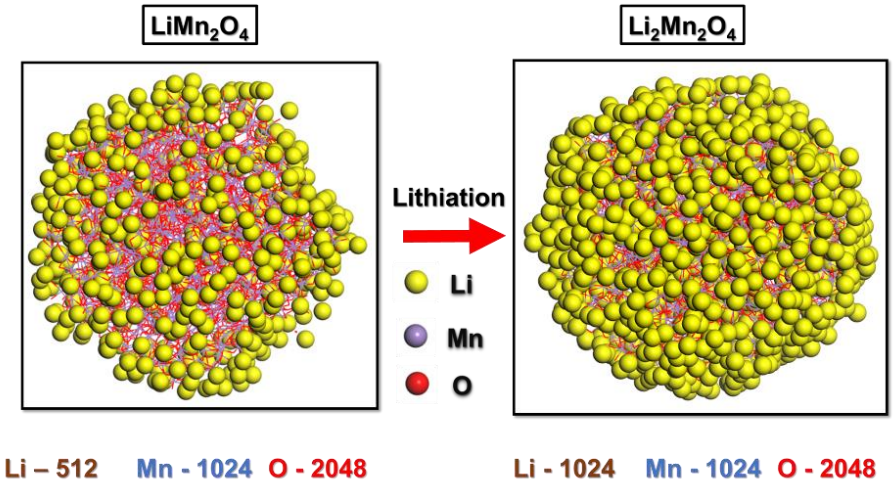

Figure 4. 4: An illustration of lithiation on the amorphous ideal spinel $LiMn_2O_4$ to the amorphous lithiated-$Li_2Mn_2O_4$. (a) Amorphous Ideal spinel $LiMn_2O_4$ nanosphere and the (b) Amorphous Lithiated-$Li_2Mn_2O_4$ spinel nanospheres.

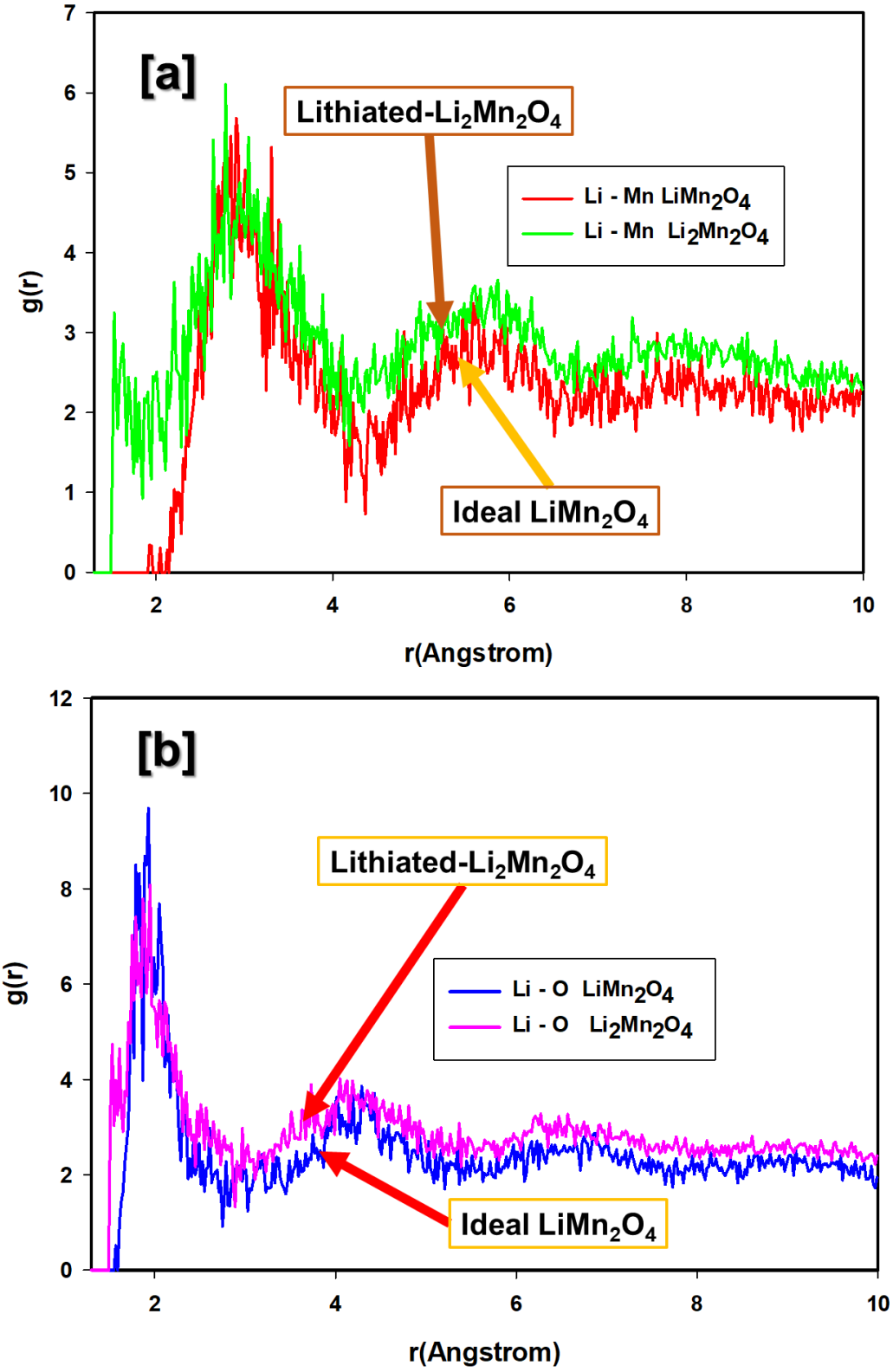

Figure 4. 5: RDFs for the ideal spinel $LiMn_2O_4$ and the lithiated-$Li_2Mn_2O_4$ spinel depicting the increase in probability of finding lithium atoms with lithiation. (a) Lithium manganese interactions (Li-Mn) and (b) Lithium oxygen interactions (Li-O).

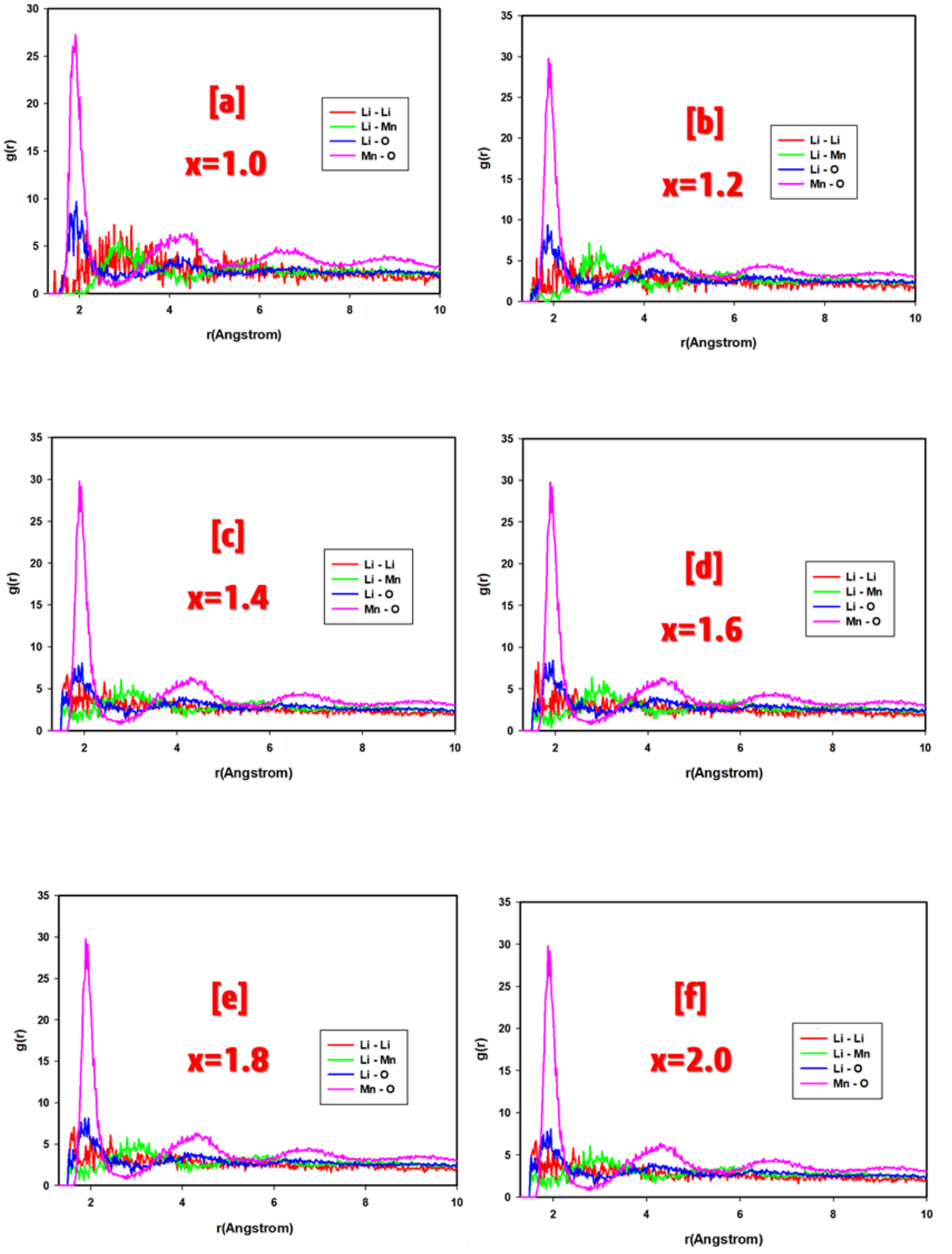

Figure 4. 6: Illustration of atomic distribution in the amorphous $Li_xMn_2O_4$ (1 < x ≤ 2) nanospheres through RDF graphs. (a) $Li_{1.0}Mn_2O_4$, (b) $Li_{1.2}Mn_2O_4$, (c) $Li_{1.4}Mn_2O_4$, (d) $Li_{1.6}Mn_2O_4$, (e) $Li_{1.8}Mn_2O_4$, and (f) $Li_{2.0}Mn_2O_4$. The Li-Li, Li-Mn, Li-O and Mn-O interactions were considered.

4.3.2 Recrystallised Li-Mn-O composite nanoarchitectures

In this section we discuss the results of the recrystallised Li-Mn-O layered-spinel composite nanoarchitectures synthesised computationally using the simulated recrystallisation. Figure 4.7 shows the atomic snapshots of these composite nanoarchitectures. The crystallinity of these nanoarchitectures is also examined by RDFs graphs illustrated in figure 4.8. The simulated recrystallisation process is monitored by plotting the configuration energy of these structures with time as the process proceeds, which is depicted in figure 4.9. The layered and spinel components formed at different lithium concentrations are examined using XRD patterns shown in figure 4.10.

The simulations yielded multi-grained polycrystalline nanospheres with grain-boundaries except for $Li_{1.6}Mn_2O_4$. In addition, the orientation and number of the crystal grains contained in these structures vary with lithium concentrations. Furthermore, $Li_{1.0}Mn_2O_4$, $Li_{1.2}Mn_2O_4$, $Li_{1.3}Mn_2O_4$, $Li_{1.4}Mn_2O_4$, $Li_{1.7}Mn_2O_4$, $Li_{1.8}Mn_2O_4$, $Li_{1.8}Mn_2O_4$ and $Li_{2.0}Mn_2O_4$ comprise of two grains separated by a grain boundary which recrystallised in different orientations. Conversely, $Li_{1.1}Mn_2O_4$ and $Li_{1.5}Mn_2O_4$ comprise of three crystal grains that are oriented differently. All the crystal grains that make up the simulated Li-Mn-O nanospheres comprise of well-ordered atomic arrangements as illustrated in figure 4.7, which shows successful recrystallisation.

RDF graphs depicting the average distribution of atoms in the recrystallised Li-Mn-O layered-spinel composite nanoarchitectures have been calculated and are shown in figure 8. Lithium-lithium (Li-Li), lithium-manganese (Li-Mn), lithium-oxygen (Li-O) and manganese-oxygen (Mn-O) atomic interactions were considered. Well-defined RDF peaks showing the probability of finding an atom at a given distance are observed on the RDF plots. Consequently, explicit sharp peaks with high amplitudes which are attributed to crystalline structures are noted on all the RDF plots in figure 4.7. Furthermore, the long sharp peaks indicate the existence of well-ordered arrangement of atoms in these structures which is in line with the atomic snapshots depicted in figure 4.7. The RDF peak separation distance, uniquely defines a lattice structure of a material. Subsequently, the first RDF peak depicts the bond length of the atomic interaction in question.

In all the RDFs of the recrystallised composite nanoarchitectures, the first RDF peak indicating the chemical bond length of Mn-O and Li-O is depicted at ~1.9 and ~1.95 Å,

respectively. Moreover, the first peak for Li-Mn and Li-Li interactions is depicted at ~2.8 and 2.87 Å, respectively. Furthermore, the Mn-O peak is the most intense peak in all these structures, showing a well-resolved long peak which connotes that manganese and oxygen atomic interaction constitutes a well-ordered atomic arrangement than any other atomic interactions in these structures. Crystalline structures are characterised by long-range structural ordering. The well-defined RDF peaks of the recrystallised Li-Mn-O layered-spinel composite nanoarchitectures extends beyond the first and the second peaks substantiating the crystallinity as revealed by the atomic snapshots in figure 7. These long-range order peaks are observed from ~1.90 Å to ~9.19 Å in all the structures.

The simulated recrystallisation process was captured by configuration energy graphs calculated as a function of time in figure 4.9. In an amorphous system, atoms are arranged in an unstable high energy atomic arrangement. The canonical ensemble employed for the simulated recrystallisation process allows the system to exchange energy with the environment at a constant temperature affording the atoms a chance to realise their low energy crystalline lattice arrangements. The recrystallisation process is started by a small group of atoms arranging in a low energy configuration forming a new phase. This process is called nucleation which is depicted by the first energy plateau in the configuration graphs depicted in figure 4.9. Subsequently, nearby atoms attach into the newly formed nucleus in established lattice positions, allowing the nucleus to grow into a large crystal. Hence, the decrease in energy from the first energy plateau into the second energy plateau showing crystal growth. The configuration energy graphs are in good agreement with the calculated RDF graphs and atomic snapshots of the recrystallised nanoarchitectures as they illustrate successful recrystallisation. Accordingly, this is indicated by the second energy plateau showing no further change in the energy in all the recrystallised nanoarchitectures. The first configuration energy plateau depicting the nucleation stage is noted to decrease with an increase in lithium concentration. This implies that the addition of lithium atoms into the system favours the nucleation process resulting in a minimal time taken to grow the newly formed nuclei to a critical size sufficient to allow crystal growth to take place. Multiple nuclei evolved in all the nanostructures resulting in multi-grained crystal structures with an exception of the $Li_{1.6}Mn_2O_4$ which recrystallised into a single crystal.

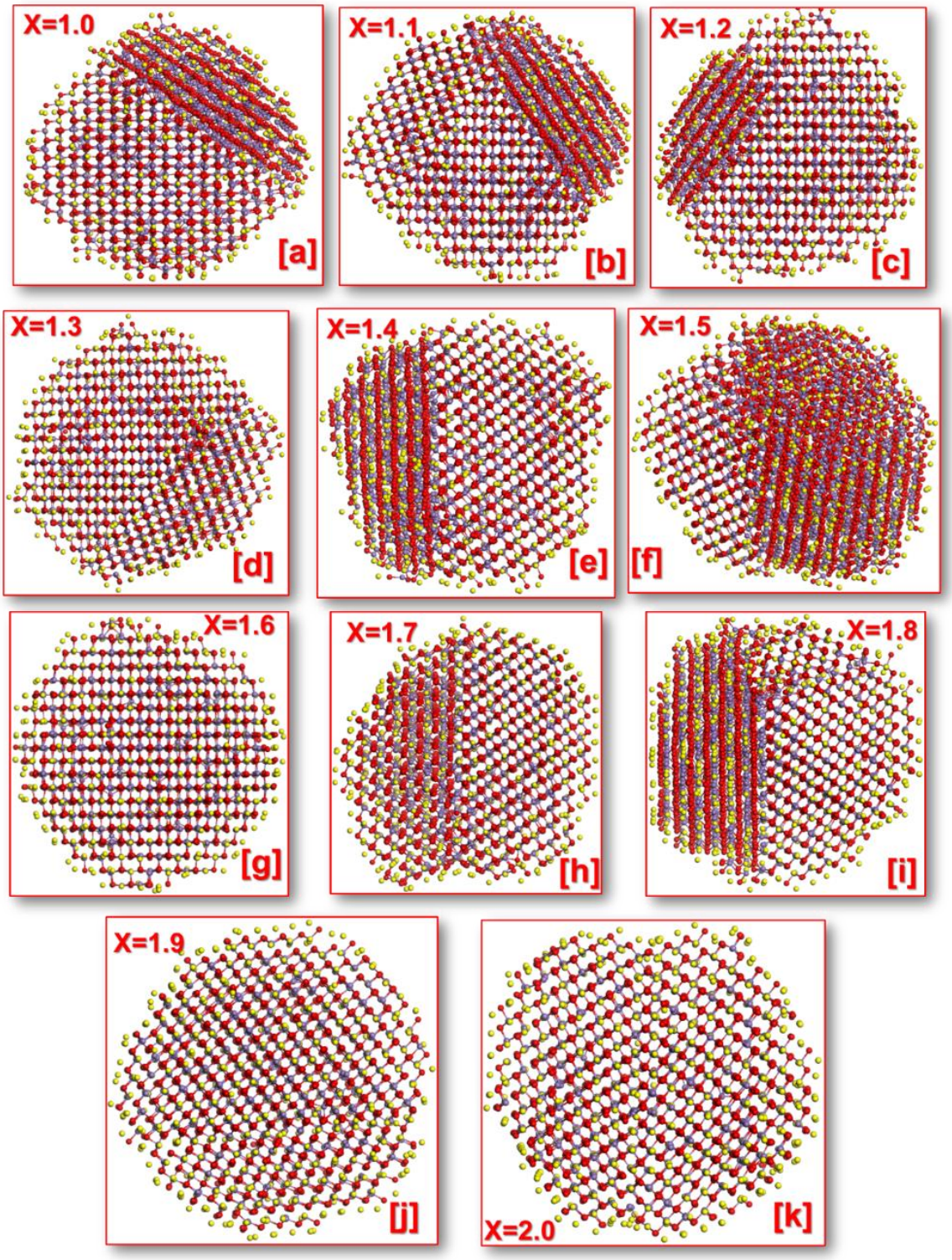

Figure 4. 7: Atomic snapshots depicting the Li-Mn-O layered and spinel comprising composite nanostructures resulting from the simulated recrystallisation. (a) $Li_{1.0}Mn_2O_4$, (b) $Li_{1.1}Mn_2O_4$, (c) $Li_{1.2}Mn_2O_4$, (d) $Li_{1.3}Mn_2O_4$, (e) $Li_{1.4}Mn_2O_4$, (f) $Li_{1.5}Mn_2O_4$, (g) $Li_{1.6}Mn_2O_4$, (h) $Li_{1.7}Mn_2O_4$, (i) $Li_{1.8}Mn_2O_4$, (j) $Li_{1.9}Mn_2O_4$ and (k) $Li_{2.0}Mn_2O_4$. The yellow, blue and red spheres represented lithium, manganese and oxygen atoms, respectively.

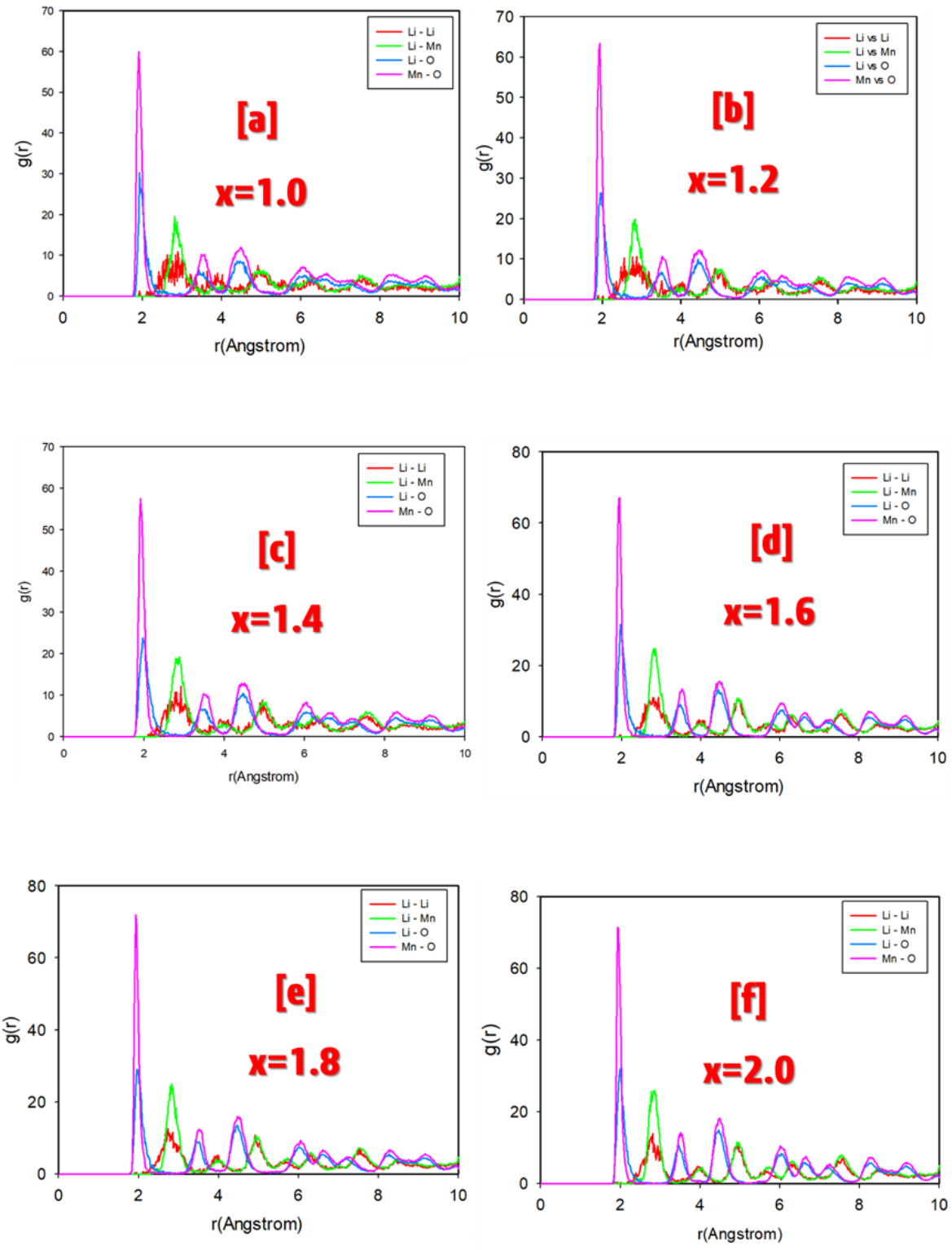

Figure 4. 8 : RDFs graphs showing sharp long peaks confirming successfully recrystallisation of the $LiMn_2O_4$ and the lithiated $Li_xMn_2O_4$ (1 < x ≤ 2) spinel nanospheres. (a) $LiMn_2O_4$, (b) $Li_{1.1}Mn2O4$, (c) $Li_{1.2}Mn_2O_4$, (d) $Li_{1.3}Mn_2O_4$, (e) $Li_{1.4}Mn2O4$, (f) $Li_{1.5}Mn_2O_4$, (g) $Li_{1.6}Mn_2O_4$, (h) $Li_{1.7}Mn_2O_4$, (i) $Li_{1.8}Mn_2O_4$, (j) $Li_{1.9}Mn_2O_4$ and (k) $Li_{2.0}Mn_2O_4$.

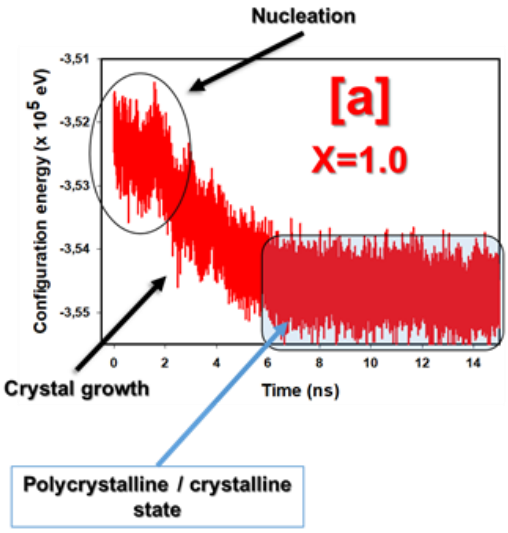
Nucleation
[a]
X=1.0
Configuration energy (x 10^5 eV)
-3,51
-3,52
-3,53
-3,54
-3,55
0 2 4 6 8 10 12 14
Time (ns)
Crystal growth
Polycrystalline / crystalline state

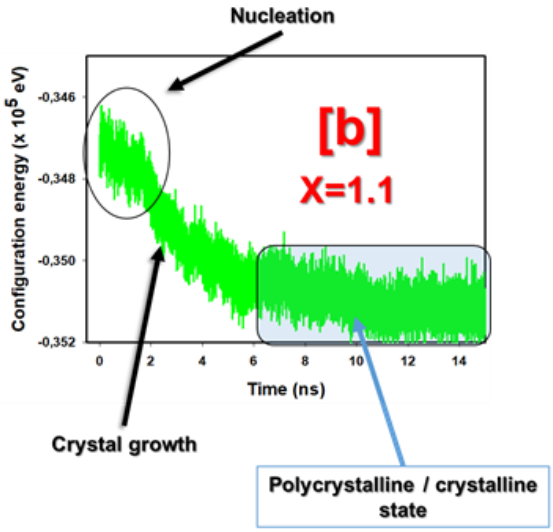
Nucleation
[b]
X=1.1
Configuration energy (x 10^5 eV)
-0,346
-0,348
-0,350
-0,352
0 2 4 6 8 10 12 14
Time (ns)
Crystal growth
Polycrystalline / crystalline state

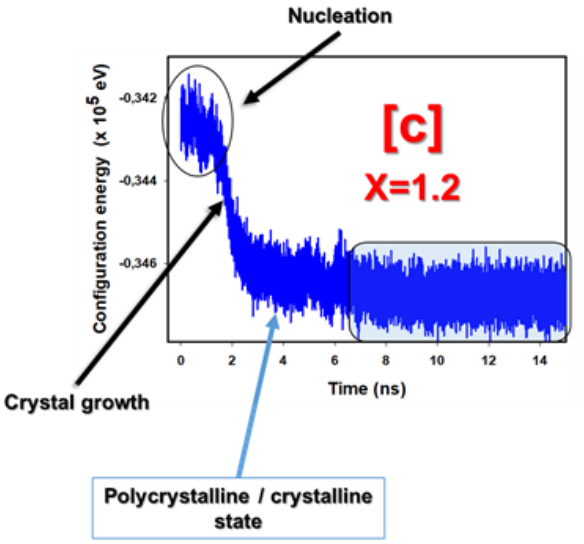
Nucleation
[c]
X=1.2
Configuration energy (x 10^5 eV)
-0,342
-0,344
-0,346
0 2 4 6 8 10 12 14
Time (ns)
Crystal growth
Polycrystalline / crystalline state

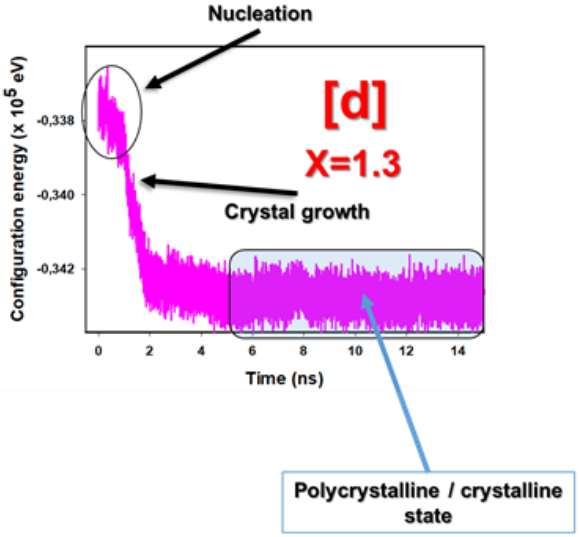
Nucleation
[d]
X=1.3
Crystal growth
Configuration energy (x 10^5 eV)
-0,338
-0,340
-0,342
0 2 4 6 8 10 12 14
Time (ns)
Polycrystalline / crystalline state

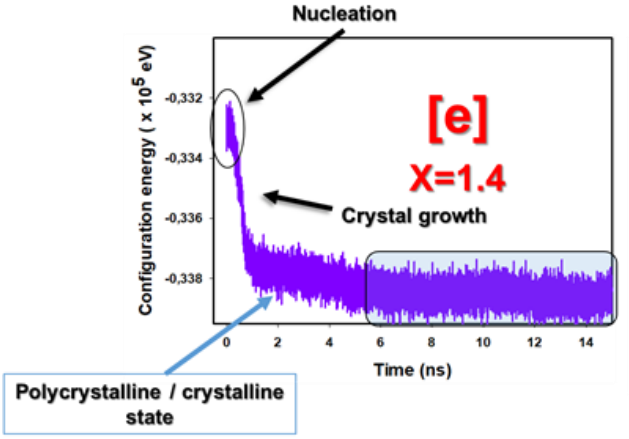
Nucleation
[e]
X=1.4
Crystal growth
Configuration energy (x 10^5 eV)
-0,332
-0,334
-0,336
-0,338
0 2 4 6 8 10 12 14
Time (ns)
Polycrystalline / crystalline state

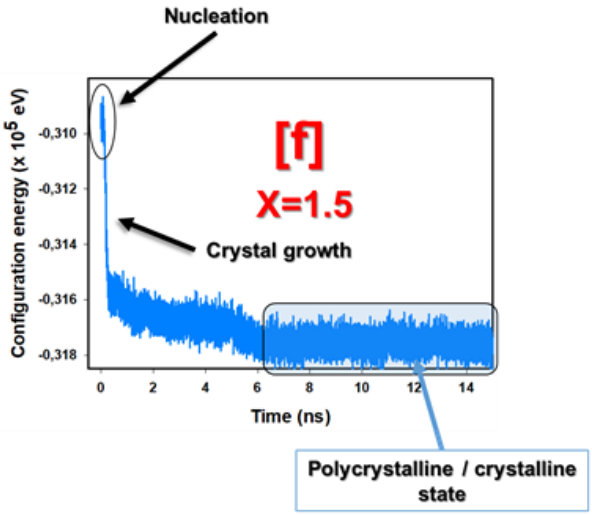
Nucleation
[f]
X=1.5
Crystal growth
Configuration energy (x 10^5 eV)
-0,310
-0,312
-0,314
-0,316
-0,318
0 2 4 6 8 10 12 14
Time (ns)
Polycrystalline / crystalline state

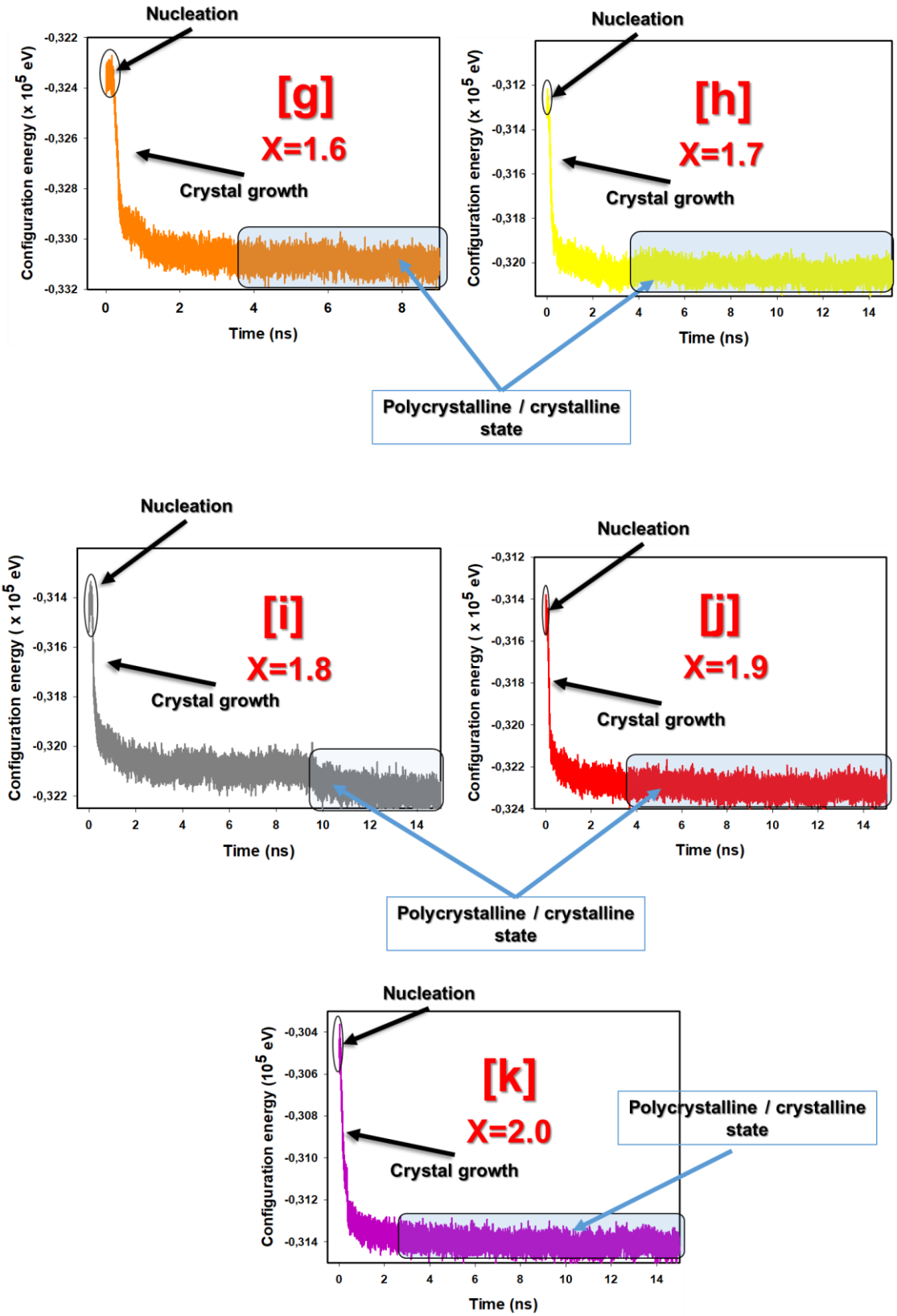

Figure 4. 9 : Configuration energy plotted against time depicting the simulated recrystallisation process for the $Li_xMn_2O_4$ ($1 \leq x \leq 2$) nanospheres. (a) $LiMn_2O_4$, (b) $Li_{1.1}Mn_2O_4$, (c) $Li_{1.2}Mn_2O_4$, (d) $Li_{1.3}Mn_2O_4$, (e) $Li_{1.4}Mn_2O_4$, (f) $Li_{1.5}Mn_2O_4$, (g) $Li_{1.6}Mn_2O_4$, (h) $Li_{1.7}Mn_2O_4$, (i) $Li_{1.8}Mn_2O_4$, (j) $Li_{1.9}Mn_2O_4$ and (k) $Li_{2.0}Mn_2O_4$.

4.3.3 Structural characterisation of the recrystallised Li-Mn-O nanoarchitectures through X-ray diffraction patterns (XRDs)

Structural characterisation of the simulated Li-Mn-O composite nanoarchitectures presented in figure 4.7 is discussed. The Li-Mn-O components encompassed in the structures are scrutinised using XRD patterns. In addition, the XRD patterns of the simulated structure are compared with XRD patterns of experimentally synthesised Li-Mn-O spinel and layered structures. Figure 4.10 presents XRD patterns for some of the recrystallised Li-Mn-O composite nanoarchitectures, captured between 10 and 60 2θ angles. Moreover, for comparison purposes only the XRD patterns for $Li_{1.2}Mn_2O_4$, $Li_{1.4}Mn_2O_4$, $Li_{1.6}Mn_2O_4$ and $Li_{2.0}Mn_2O_4$ were considered.

The simulated nanospheres are ~4.5 nm in diameter, hence some of the XRDs peaks are not well-resolved. $LiMn_2O_4$, Mn_3O_4 and Li_2MnO_3 characteristic peaks are observed in all the depicted XRD patterns confirming successful simulated synthesis of the Li-Mn-O layered-spinel composites. Figure 4.11 compares XRD patterns of the simulated Li-Mn-O layered-spinel composites with experimental Li-Mn-O layered and spinel structures. The majority XRD peaks of $LiMn_2O_4$ and Li_2MnO_3 positioned between 10 and 60 2θ angles are superimposed, however, they are distinguished by a small peak located between ~19 and 21 2θ angles for Li_2MnO_3 and a well-resolved peak located between ~58 and 60 2θ angles for $LiMn_2O_4$. In the illustrated 2θ range Mn_3O_4 comprise of XRD peaks which are superimposed with $LiMn_2O_4$ and Li_2MnO_3 XRD peaks and several distinct peaks setting it apart from the two components. Moreover, Mn_3O_4 characteristic peaks are observed between ~27 and ~34 2θ angles.

The layered Li_2MnO_3 and spinel $LiMn_2O_4$ characteristic peaks situated between ~19 and 21, and ~43 and 47 2θ angles are observed in all the simulated layered-spinel composite nanoarchitectures alluding presence of these components in all the simulated structures. The Mn_3O_4 characteristic peaks located between 27 and 34 2θ angles are more intense at low lithium concentrations, however, they decrease with lithium concentration. It is well-known that the formation of Mn_3O_4 is favoured by excess manganese oxide in a material [194]. In the XRD pattern of the single crystal $Li_{1.6}Mn_2O_4$ nanostructure we observe two peaks between ~43 and ~47 2θ which are associated with the single crystallinity of this structure.

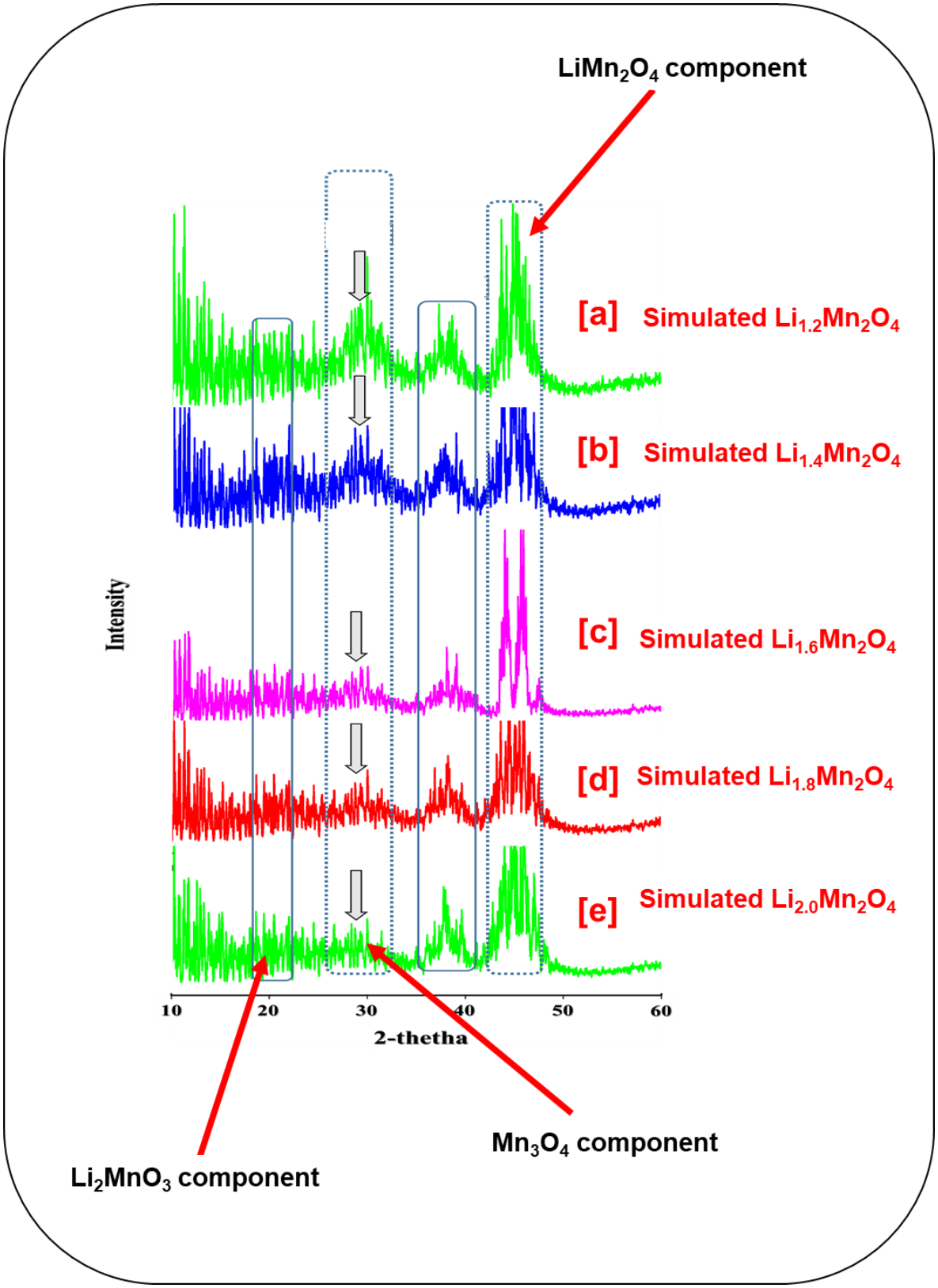

Figure 4. 10: XRD patterns of the recrystallised Li-Mn-O layered-spinel composite nanostructures depicting the layered Li_2MnO_3, and $LiMn_2O_4$ and Mn_3O_4 spinel components. (a) $Li_{1.2}Mn_2O_4$, (b) $Li_{1.4}Mn_2O_4$, (c) $Li_{1.6}Mn_2O_4$, (d) $Li_{1.8}Mn_2O_4$, (e) $Li_{2.0}Mn_2O_4$

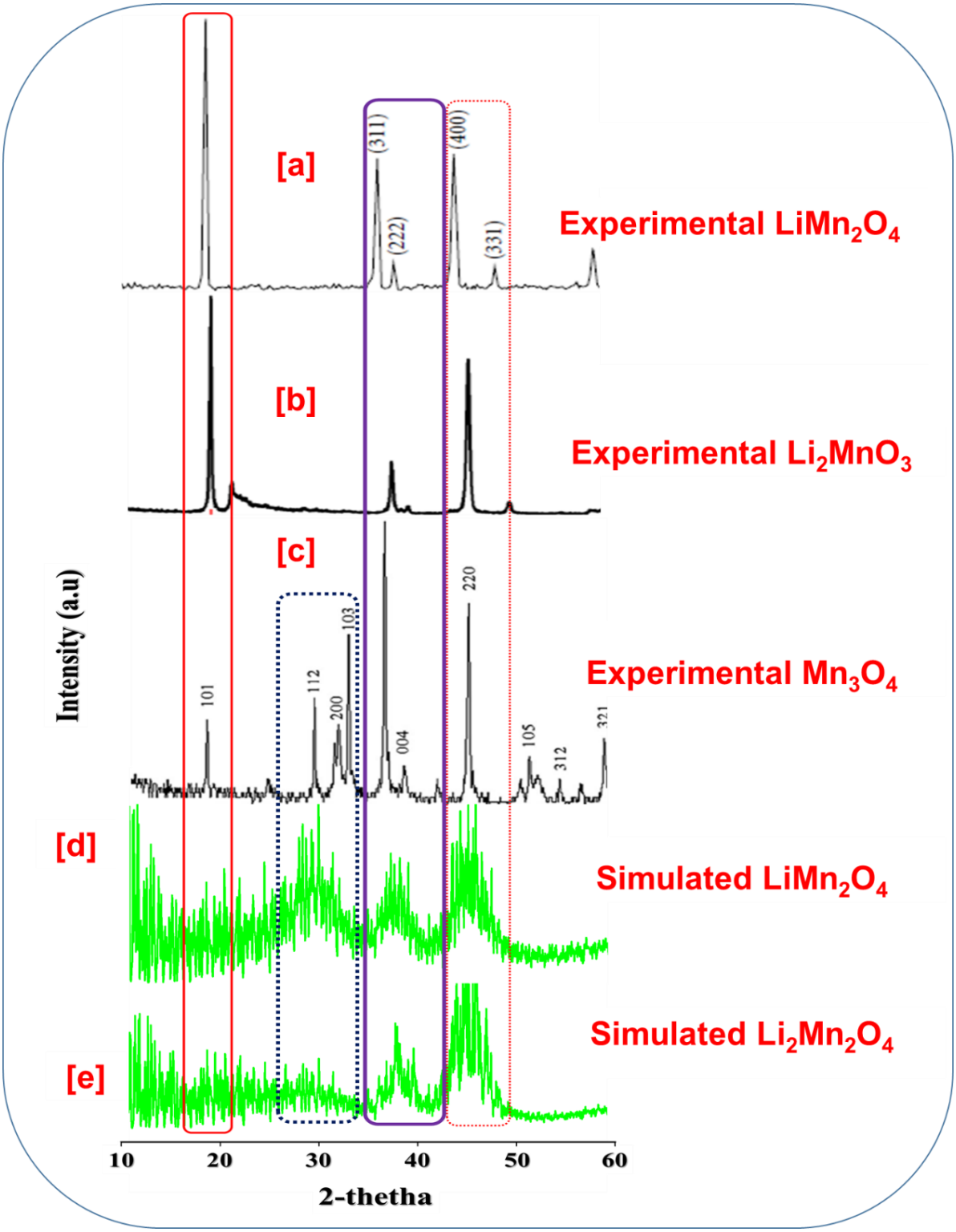

Figure 4. 11: Comparison of the simulated Li-Mn-O layered-spinel composites nanoarchitectures with experimentally synthesised Li-Mn-O layered and spinel structures through XRDs. Experimentally synthesised: (a) $LiMn_2O_4$ spinel [194], (b) Li_2MnO_3 layered [195] and (c) Mn_3O_4 spinel [196] and computationally synthesised (d) $LiMn_2O_4$ spinel and (e) $Li_2Mn_2O_4$ spinel.

4.3.4 Microstructural features of the simulated Li-Mn-O layered-spinel composite nanoarchitectures

In this section, structural characterisation of $Li_{1.0}Mn_2O_4$, $Li_{1.3}Mn_2O_4$, $Li_{1.6}Mn_2O_4$, $Li_{1.8}Mn_2O_4$ and $Li_{2.0}Mn_2O_4$ through atomic level snapshots is carried out. Microstructural features that evolve during the simulated recrystallisation process are examined. Consequently, the microstructure of $Li_{1.0}Mn_2O_4$ has been captured and illustrated by the atomic snapshots depicted in figure 4.12. A (b) portion of one of the grains contained in this nanosphere is depicted in the figure. A significant amount of spinel Mn_3O_4 is observed from this slice and is confirmed by a perfect spinel Mn_3O_4 model. The Mn_3O_4 conventional unit cell in figure 4.12 (i) c-e is viewed along the (100) plane which explicitly shows manganese atoms occupying the three-dimensional channels. Moreover, a manganese-rich defective spinel Mn_3O_4 viewed along the (110) plane and a layered Li_2MnO_3 component are observed on the sliced portion of the $Li_{1.0}Mn_2O_4$ nanosphere depicted in figure 4.12 (ii), evidence the co-existence of these components. Crystallographic defects are also observed in the $Li_{1.0}Mn_2O_4$ nanosphere as illustrated in figure 4.13. Accordingly, two uneven crystal grains connected by grain boundaries are noted in this structure. The extracted portion containing essential microstructural features, reveal the presence of point defects such as vacancy and interstitial points defects as illustrated in figure 4.13 d and e, respectively.

Figure 4.14 (i) shows a slice cut from the simulated $Li_{1.3}Mn_2O_4$ nanosphere comprising of essential microstructural features. A defective (e) layered Li_2MnO_3 signifying the formation of Li_2MnO_3 component which is in line with the (f) ideal Li_2MnO_3 model is observed on the depicted slice. Moreover, a conventional unit cell of spinel Mn_3O_4 constituting crystallographic point defects is noted. In addition, some of the normally unoccupied 16c sites in the Mn_3O_4 structure are occupied by manganese atoms denoting the presence of interstitial point defects. Furthermore, few lithium atoms are noted on the16c sites signalling a formation of the $LiMn_2O_4$ spinel component. Figure 4.14 (i) b shows the presence of $LiMn_2O_4$ spinel component in the $Li_{1.3}Mn_2O_4$ nanosphere which is comparable to the perfect $LiMn_2O_4$ model illustrated. However, this conventional unit cell comprises of manganese atoms occupying the 16c lattice sites which designate substitutional crystallographic defects. The simulated $Li_{1.3}Mn_2O_4$ nanosphere recrystallised into two grains with similar atomic orientation indicated by

the arrows in figure 4.14 (ii) a. The two grains are joined together by a grain boundary which constitutes of atoms that are aligned differently in the two grains.

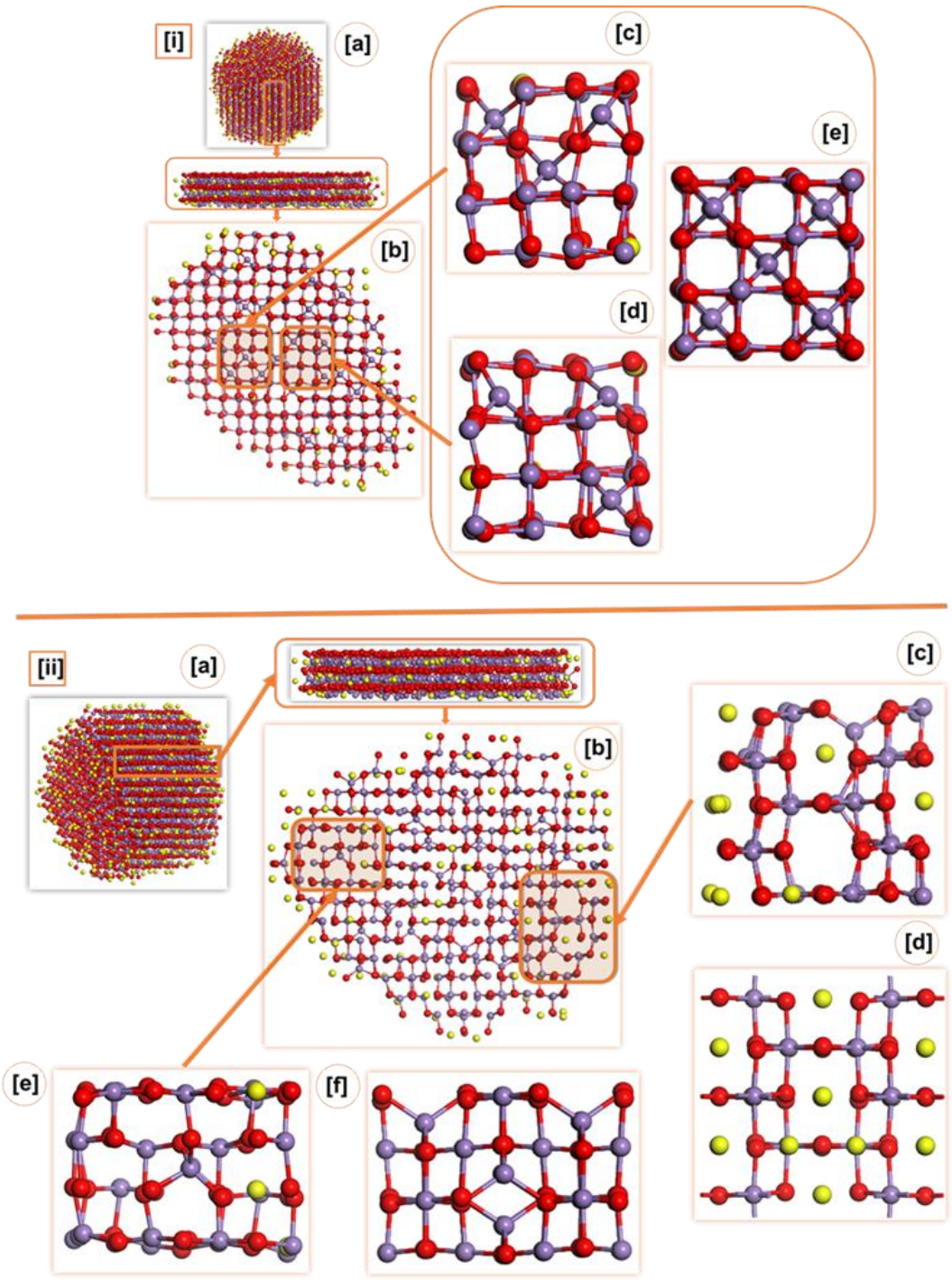

Figure 4. 12 : Depiction of microstructural features of the simulated (i) (a) $Li_{1.0}Mn_2O_4$ nanosphere showing the presence of (i) (c-d) Mn_3O_4 component viewed along the (100) plane which is compared to a Mn_3O_4 model. The simulated (ii) (e) Mn_3O_4 component is compared with a perfect (ii) (f) Mn_3O_4 model viewed along the (110) plane. The (ii) (c) layered Li_2MnO_3 component is also captured and compared with a perfect (ii) (d) Li_2MnO_3 model.

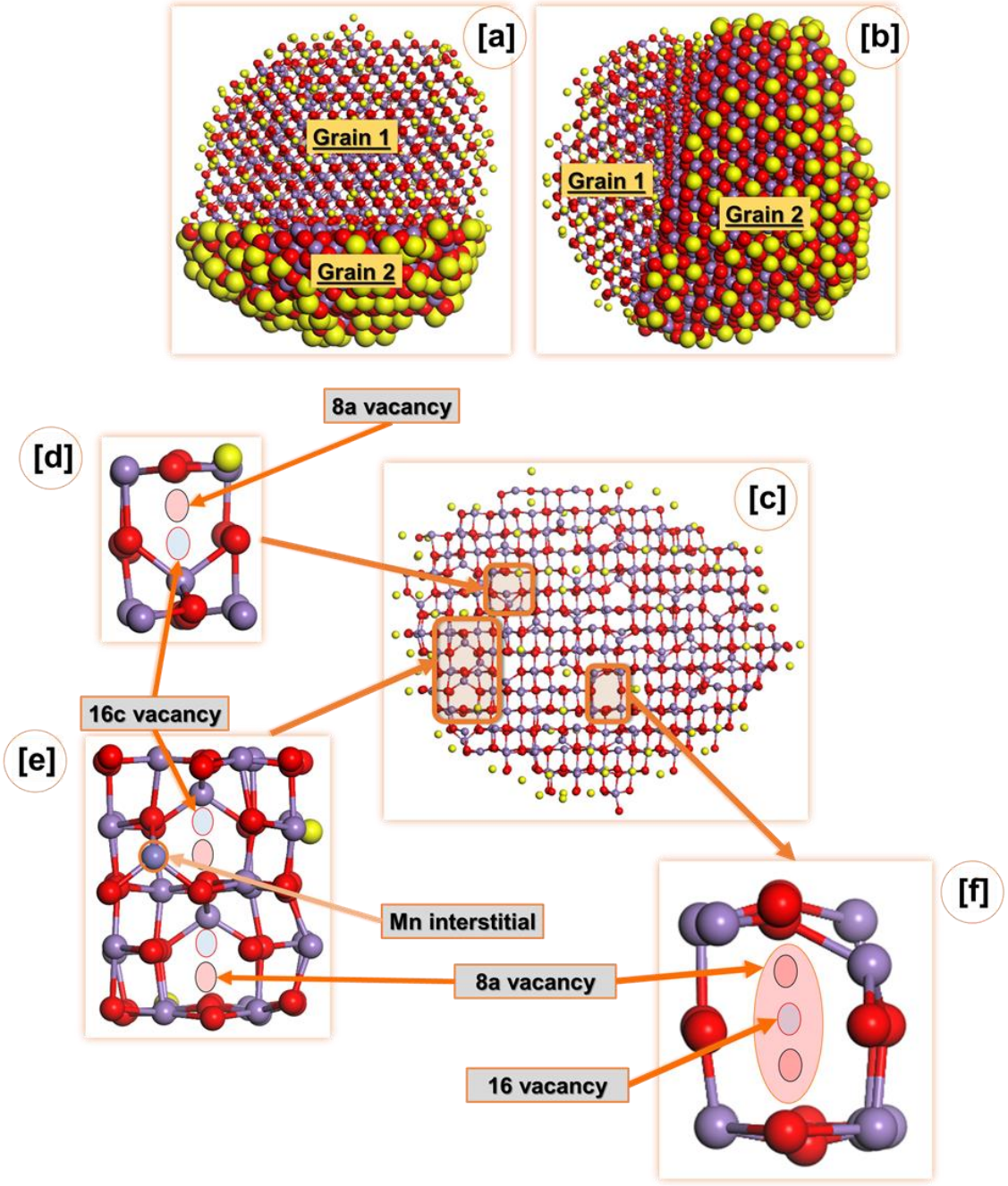

Figure 4. 13 : (a-b) Schematic illustration of crystallographic defects contained in $Li_{1.0}Mn_2O_4$ nanostructure. The two grains that make up this structure are denoted by (a) and (b). A (c) portion of the $Li_{1.0}Mn_2O_4$ nanosphere showing microstructural features present in the structure have been sliced. Point defects observed are denoted by the magnified atomic snapshots.

Figure 4.15 shows a schematic representation of microstructural features of the simulated $Li_{1.6}Mn_2O_4$ nanosphere. The nanosphere recrystallised into a single crystal, wherein, long-range atomic ordering is observed as illustrated in figure 4.15 (k - l).

Consequently, two portions extracted from this nanomaterial are depicted by (c - d) in the figure, wherein, essential microstructural features denoted were observed. Moreover, substitutional point defects are predominant in the spinel $LiMn_2O_4$ phases denoted by (b) and (f). The simulated Li-Mn-O spinel phase compare very well with the ideal Li-Mn-O spinel phases with a significant number of lithium atoms located at the 16c octahedral lattice sites. However, sporadic manganese atoms on the 16c octahedral lattice sites are also noted which shows the spinel Mn_3O_4 characteristics. Figure 4.15 (i) shows the $Li_{1.6}Mn_2O_4$ nanosphere along the (100) plane from which a number of 8a tetrahedral lattice sites on the three dimensional channels are occupied by manganese atoms and a significant number of the 8a tetrahedral channels are unoccupied. A considerable number of point defects such as (h) interstitial and (i - j) vacancy point defects are also observed on the extracted portions.

The polycrystalline $Li_{1.8}Mn_2O_4$ simulated nanosphere comprising of three unequal crystal grains showing different atomic orientations as depicted in figure 4.16 (a, h, i). In figure 4.16 (h), the grain denoted as grain 1 shows a predominant long-range atomic order. However, a different view shows the middle grain denoted as grain 2 in figure 4.16 (i) constituting long-range atomic ordering. Figure 4.16 (d) shows a slice cut from the simulated polycrystalline $Li_{1.8}Mn_2O_4$ nanosphere constituting significant microstructural features contained in this nanomaterial. Furthermore, we note the co-existence of less defective layered (b) Li_2MnO_3 and spinel (f) $LiMn_2O_4$ components which are comparable to the perfect layered Li_2MnO_3 and spinel $LiMn_2O_4$ components, respectively. Substitutional defects are dominant in both the observed conventional unit cells, particularly substitution of manganese 16d atoms by lithium atoms and substitution of lithium 16c atoms by manganese atoms in the spinel $LiMn_2O_4$ cell.

Figure 4.17 illustrates the microstructure of the (a) $Li_{2.0}Mn_2O_4$ simulated nanosphere containing substantial amount of lithium atoms. This nanomaterial crystallised into two grains with similar atomic orientations joined together by a grain boundary. Both grains denoted by (k - l) nearly shows the same long-range atomic ordering. The grain boundary depicted by (m) is noted by distinctive atomic arrangement. A few atomic layers were extracted from this nanomaterial from which the formed microstructural features were examined. Layered Li_2MnO_3 and spinel $LiMn_2O_4$ phases are observed confirming a successfully simulated synthesis of the layered-spinel composite material. Furthermore, the formed phases are confirmed by the ideal layered Li_2MnO_3 and spinel $LiMn_2O_4$ conventional unit cells. A number of substitutional defects are also

observed from which manganese atoms are substituted by lithium atoms on the 16d lattice sites.

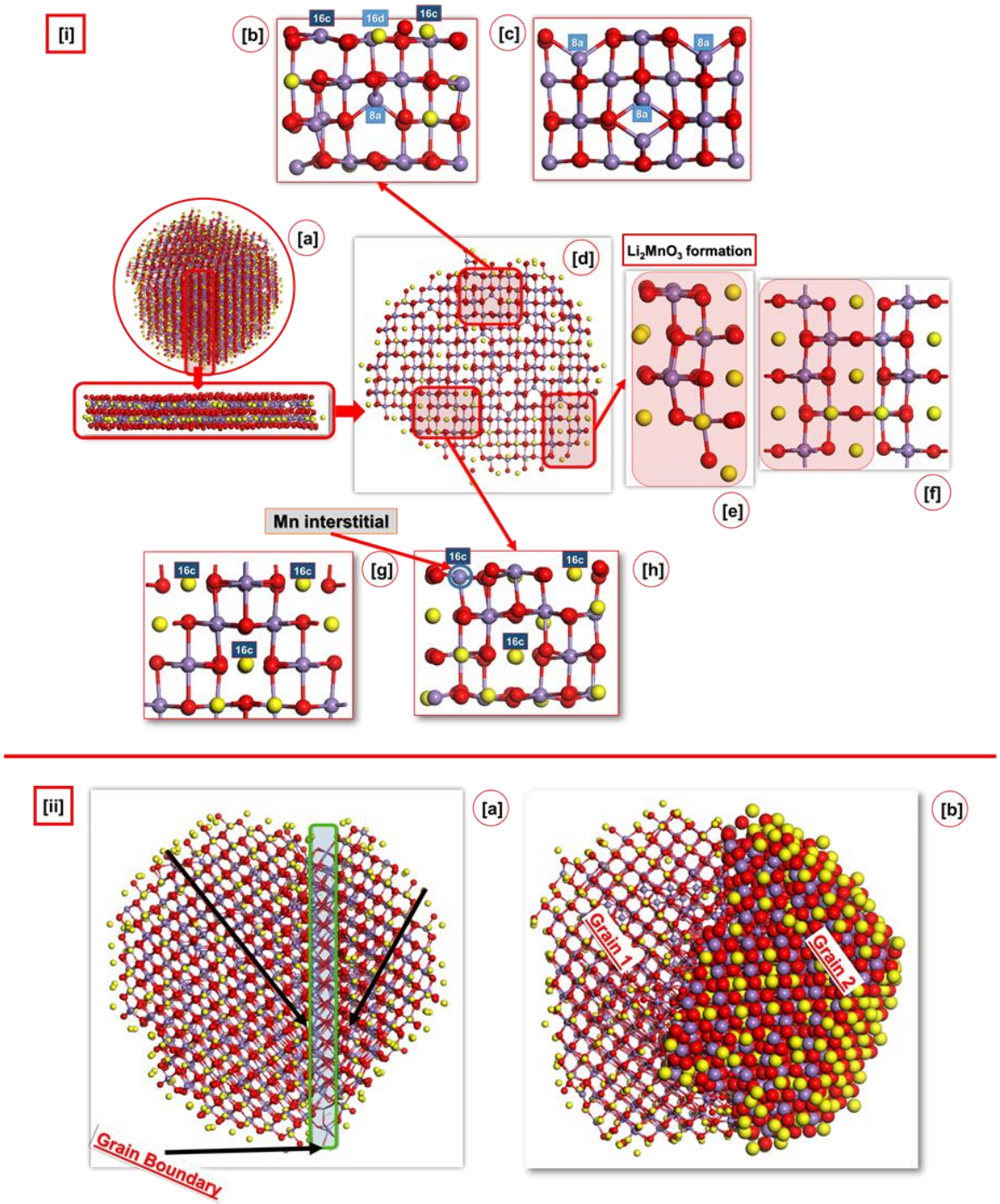

Figure 4. 14 : (i) A schematic representation of the co-existence of (b) Mn_3O_4 and (h) $LiMn_2O_4$ components in the (a) $Li_{1.3}Mn_2O_4$ simulated nanosphere. These spinel components are then compared with perfect Mn_3O_4 and $LiMn_2O_4$ models, respectively. (e) Shows the formation of Li_2MnO_3 validated by a perfect (f) Li_2MnO_3 model. (ii) (a - b) Two grains of this nanoarchitecture separated by a grain boundary.

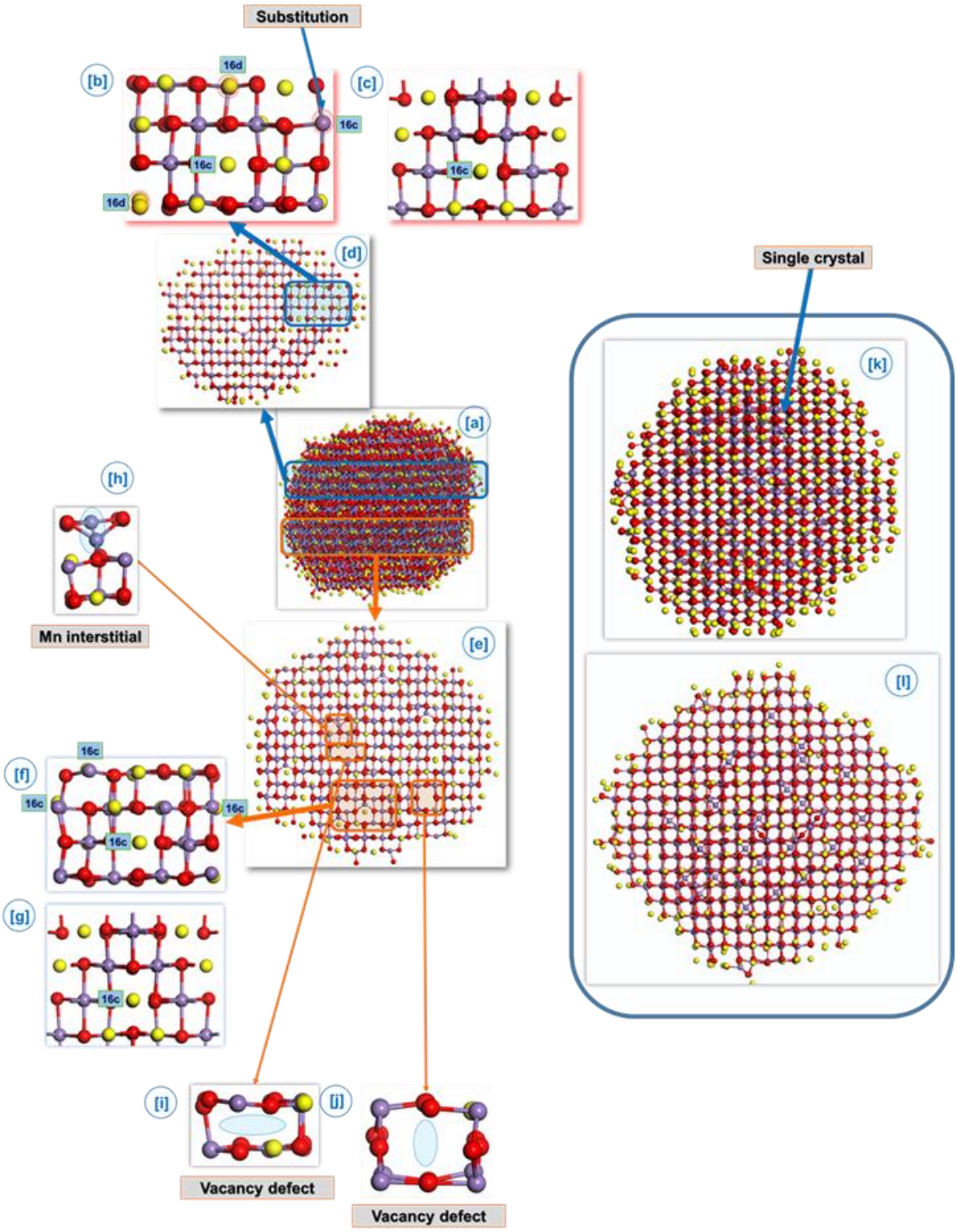

Figure 4. 15: Depicts microstructural features comprised in the crystal structure of the simulated (a) $Li_{1.6}Mn_2O_4$ nanosphere. The observed $LiMn_2O_4$ components are denoted by (a) and (f), respectively. These components are then validated by a perfect $LiMn_2O_4$ model represented by (c) and (g). Noted crystallographic defects point defects are denoted by (h - j) and the single crystalline $Li_{1.6}Mn_2O_4$ nanosphere is denoted by (k - l).

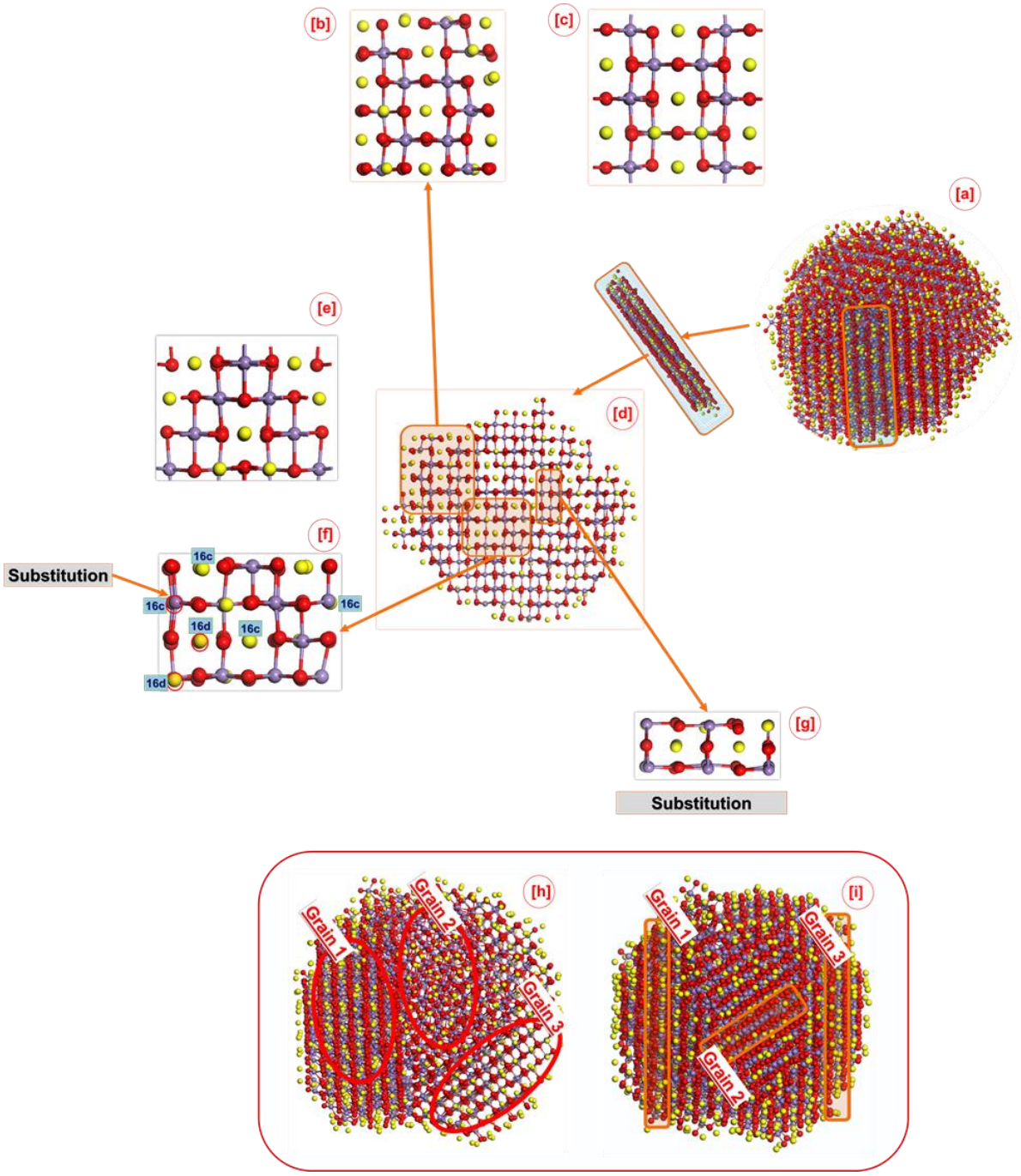

Figure 4. 16: A schematic illustration of the Li-Mn-O components that evolved during the simulated recrystallisation process in the (a) $Li_{1.8}Mn_2O_4$ nanosphere. The co-existence of layered (b) Li_2MnO_3 and spinel (f) $LiMn_2O_4$ components were observed which are compared with the perfect (c) Li_2MnO_3 and (e) $LiMn_2O_4$ models, respectively. The noted manganese and lithium substitutional point defects are denoted by (g). The three uneven grains that make-up the $Li_{1.8}Mn_2O_4$ nanosphere are denoted by (h - i).

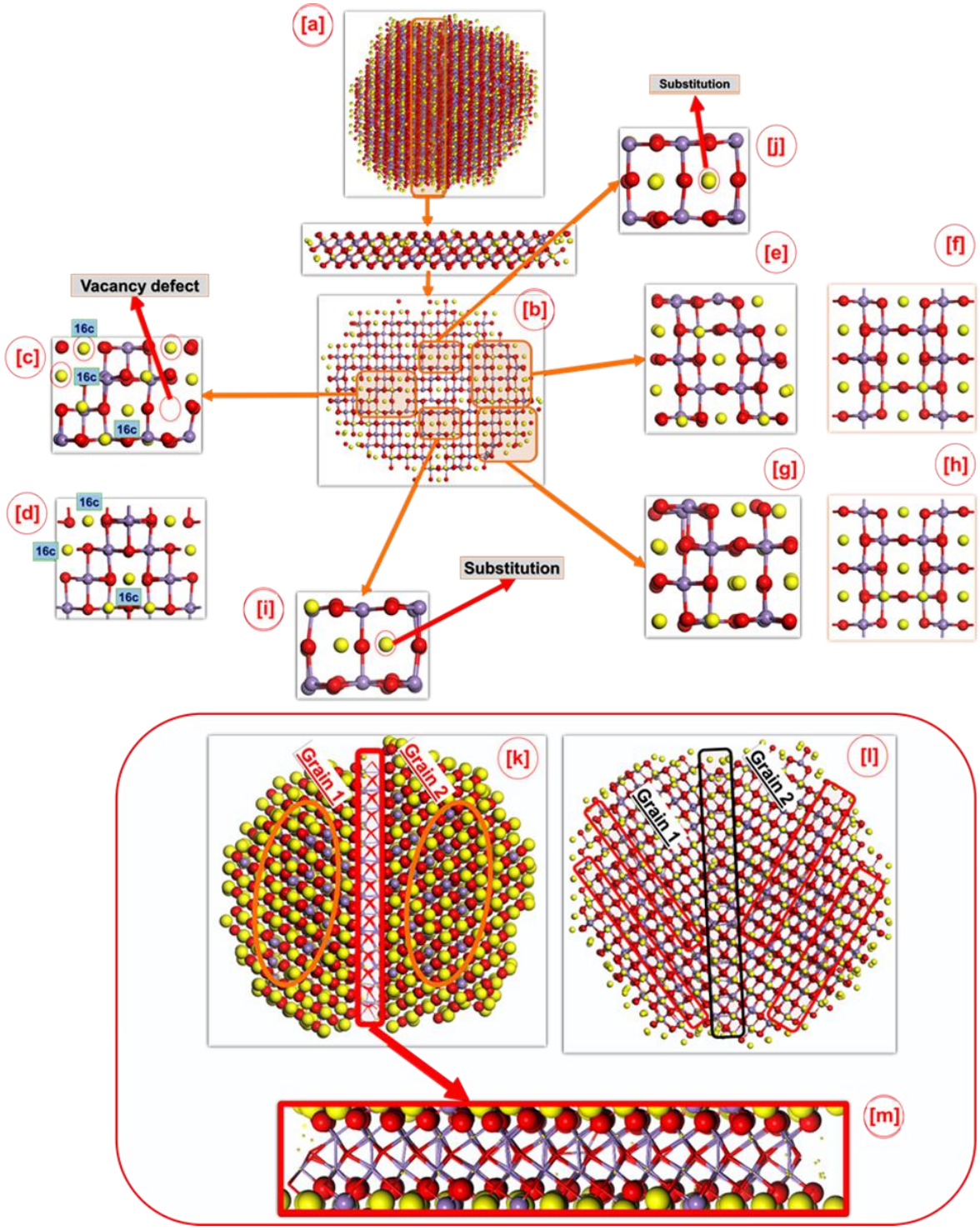

Figure 4. 17: Microstructural features of the simulated (a) $Li_{2.0}Mn_2O_4$ nanosphere. A sliced (b) portion of this nanoarchitecture comprising of spinel (c) $LiMn_2O_4$, layered (e) Li_2MnO_3 and crystallographic (I - j) point defects. The layered Li_2MnO_3 and spinel $LiMn_2O_4$ components are confirmed by their respective perfect models, (d) and (f). The two $Li_{2.0}Mn_2O_4$ crystal grains connected together by a (m) grain boundary are denoted by (k - i).

4.3.5 Crystallinity of the simulated Li-Mn-O layered-spinel composite nanoarchitectures by use of atomic snapshot and RDF graphs

Distribution of manganese and oxygen atoms in the perfect $Li_{1.0}Mn_2O_4$ spinel model and the simulated layered-spinel composite nanoarchitectures ($Li_{1.0}Mn_2O_4$, $Li_{1.6}Mn_2O_4$ and $Li_{2.0}Mn_2O_4$) is captured by the plotted Mn-O RDF graphs depicted in figure 4.18 (a - b). Moreover, figure 4.18 (b) denote RDF peaks representing the bond length of manganese and oxygen atoms in these Li-Mn-O layered-spinel systems. Furthermore, the first RDF peak of these layered-spinel systems is then compared to the first RDF peak of the perfect $LiMn_2O_4$ spinel model to aid in scrutinising the crystallinity of these structures. The three-dimensional Li-Mn-O spinel channels that facilitate the diffusion of lithium ions during a charge/discharge process are formed by manganese and oxygen atoms. Hence, the Mn-O bond length is essential in this regard. The perfect $Li_{1.0}Mn_2O_4$ structure consist of sharp RDF peaks indicating that manganese and oxygen atoms are occupying their exact ideal lattice positions. However, the RDF peaks of the simulated Li-Mn-O layered-spinel composite nanoarchitectures are slightly broad as compared to the RDF peaks of the ideal spinel structure. The addition of lithium atoms increases the crystallinity of these nanomaterials, which is evinced by a decrease in the broadening of RDF peaks as lithium concentration increase. The first Mn-O RDF peak of the simulated $Li_{1.0}Mn_2O_4$ nanomaterial is broader than the first Mn-O RDF peak of the simulated $Li_{2.0}Mn_2O_4$ nanomaterial.

Figure 4.19 shows the atomic arrangement of the simulated Li-Mn-O layered-spinel composite nanoarchitectures, (a) $Li_{1.0}Mn_2O_4$ and (b) $Li_{2.0}Mn_2O_4$. Figure 4.19 (c - d) shows magnified portions of the structures depicted in figure 4.19 (c - d), for a clear display of the atomic arrangement in these structures. The simulated $Li_{2.0}Mn_2O_4$ nanoarchitecture comprise of clear three-dimensional channels than the simulated Li-Mn-O $Li_{1.0}Mn_2O_4$ nanoarchitectures. As such, the crystallinity of the simulated Li-Mn-O composite nanoarchitectures increases with lithiation.

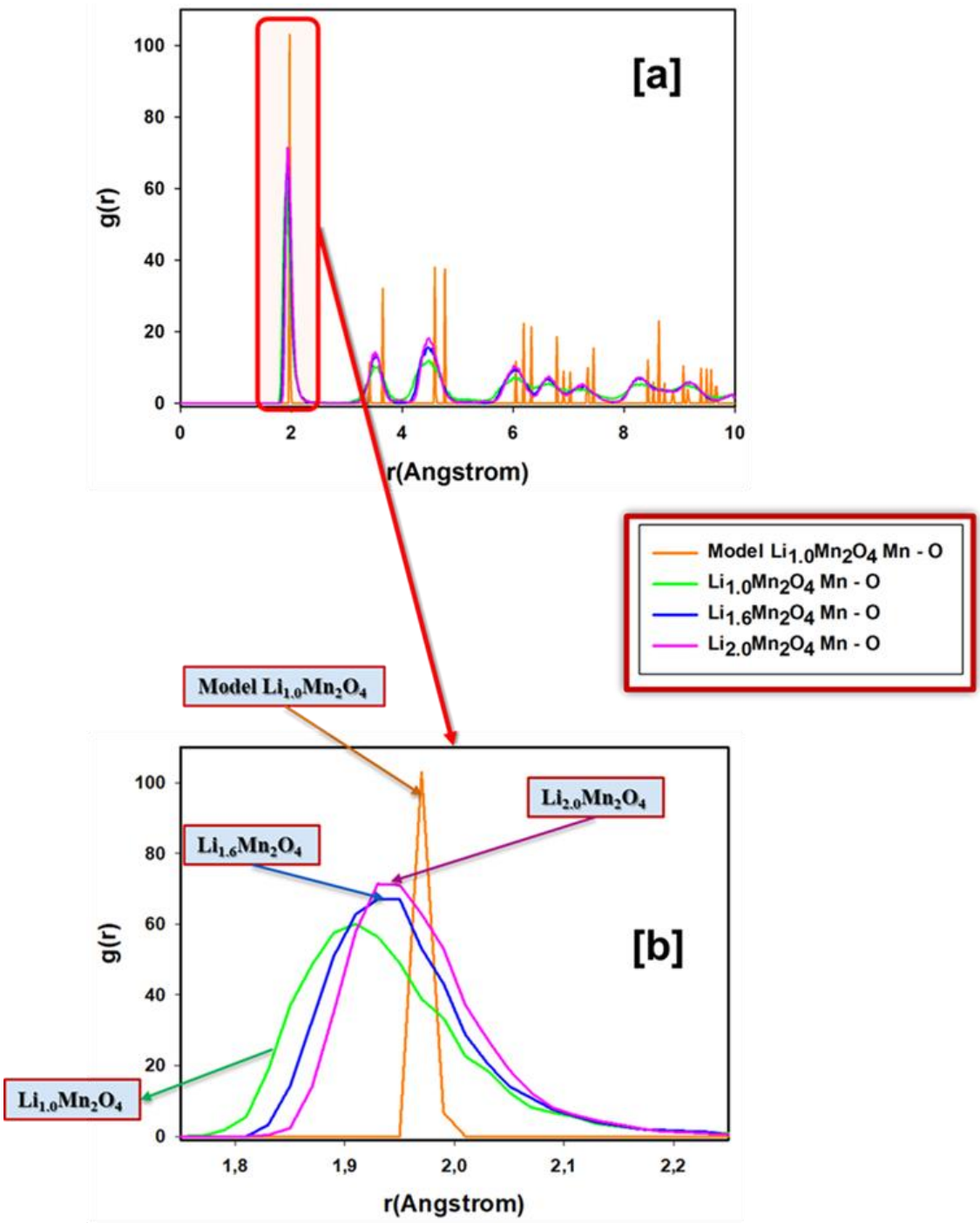

Figure 4. 18: Comparison of Mn-O RDF graphs of the perfect $Li_{1.0}Mn_2O_4$ spinel model with the simulated Li-Mn-O layered-spinel composites nanoarchitecture: $Li_{1.0}Mn_2O_4$, $Li_{1.6}Mn_2O_4$, and $Li_{2.0}Mn_2O_4$. (b) The magnified first peaks of the RDF graphs denote the Mn-O bond length.

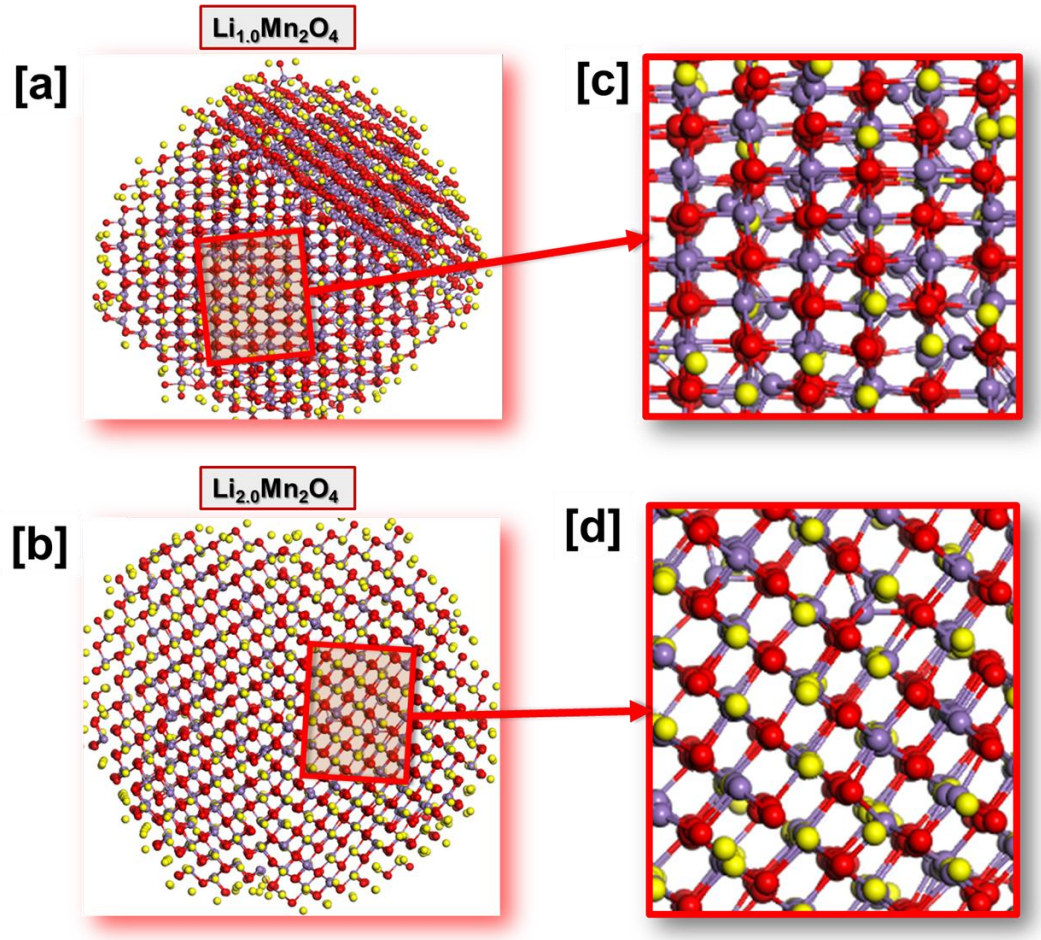

Figure 4. 19 : Comparison of the crystallinity of the simulated $Li_{1.0}Mn_2O_4$ and $Li_{2.0}Mn_2O_4$ nanoarchitectures using atomic level snapshots. (a - b) $Li_{1.0}Mn_2O_4$ and $Li_{2.0}Mn_2O_4$ simulated nanospheres, respectively. Magnified portions showing clear atomic arrangement are depicted by (c - d).

4. Discussions

In this chapter, the discharge process was simulated by generating Li-Mn-O layered-spinel composite nanoarchitectures at different lithium concentrations ($1 \leq x \leq 2$) using the simulated amorphisation and recrystallisation performed using the molecular dynamics code, DLPOLY [189]. Simulated amorphisation was carried out under the micro-canonical ensemble from which a chemical lithiation was performed. The resulting lithiated Li-Mn-O amorphous structures were then recrystallised under the canonical (NVE) ensemble. The success of the simulated amorphisation was confirmed by RDF graphs and atomic level snapshots. Furthermore, the simulated recrystallisation process was also carried out successfully as captured by atomic

snapshots, configuration energy graphs and RDF graphs. Essential microstructural features formed in all the recrystallised layered-spinel composite nanoarchitectures were inspected in order to study the discharge process. The co-existence of the layered (Li_2MnO_3) and spinel ($LiMn_2O_4$ and Mn_3O_4) in the simulated nanostructures was confirmed by atomic snapshots and XRD patterns. Moreover, a key number of crystal point defects which plays an important role in the electrochemical properties of these nanomaterials have been observed. The configuration energy graphs illustrating the simulated recrystallisation process indicates that the required time for a nucleus to reach a critical size that enables its growth decrease with lithium concentration. All the simulated Li-Mn-O layered-spinel composite nanoarchitectures recrystallised into polycrystalline nanospheres with an exception of the $Li_{1.6}Mn_2O_4$ nanosphere which recrystallised into a single crystal. A notable amount of the spinel Mn_3O_4 component is observed on the composite nanostructures with lower lithium content, i.e., $Li_{1.0}Mn_2O_4$, $Li_{1.3}Mn_2O_4$ and $Li_{1.6}Mn_2O_4$ from the calculated XRD patterns and atomic level snapshots. As the discharge process proceeds a significant number of spinel $LiMn_2O_4$ and layered Li_2MnO_3 phases are noted which indicates that lithiation favours the formation of these phases. A considerable amount of vacancy defects are observed at lower lithium concentrations and they decrease with an increase in lithium concentration. The calculated XRD patterns confirm the co-existence of Li-Mn-O layered and spinel phases in these nanoarchitectures which is in good accord with the captured atomic snapshots. However, the spinel Mn_3O_4 phase is noted to decrease as the discharge process proceeds, this is also in line with the depicted atomic snapshots from figure 4.12 to figure 4.17. Diffraction peak splitting is observed between 43 – 48 2θ angles on the XRD pattern of the simulated $Li_{1.6}Mn_2O_4$ nanosphere in figure 4.10, this is aligned with the fact that single crystals diffract the incident x-ray more than polycrystalline materials and can also indicate the reported cubic to tetragonal phase transformation observed in $LiMn_2O_4$ spinel structures [197, 198, 199].

CHAPTER 5

Conclusion and recommendations

5.1 Conclusion

Lithium-ion batteries made a substantial impact on the advancement of various technology applications due to their high energy densities, particularly in portable electronic devices. However, there is a notable increase in demand for sustainable energy due to the exponential technology growth and the need to move away from traditional energy sources to sustainable environmental friendly energy sources. This requires the development of sufficient affordable energy storage systems with the ability to power large scale systems such as electric vehicles. Lithium-ion batteries are one of the potential solutions owing to improvement of their electrochemical performance which involves the use of abundant suitable electrode materials. The reported synergistic effect of layered-spinel composite materials which resulted in a tremendous improvement on their structural stability, cycling performance and higher specific capacity, > 250 mAh/g qualifies this propitious material as a viable option in advancing lithium-ion batteries. However, there's limited information on the internal structural changes responsible for the noted enhanced electrochemical performance of these layered-spinel composites with a number of studies focusing on improvement of their specific capacity. Hence, in this study we employed the first-principles DFT studies and the well-understood simulated amorphisation and recrystallisation molecular dynamics technique to explore the electronic and atomic structure of the layered-spinel composite material as a function of lithium concentration.

The study of the non-magnetic and magnetic electronic structure of spinel $LiMn_2O_4$ carried out using the first-principles DFT code (CASTEP) provided valuable insights on the conductivity of this material. Analysis of the electronic structure was explored through electronic band structures and DOS calculations. The non-spin polarised $LiMn_2O_4$ spinel electronic structure demonstrated good conductivity in all the studied concentrations (Mn_2O_4, $LiMn_2O_4$ and $Li_2Mn_2O_4$) as evidenced by overlapping valance and conduction band notable in the calculated electronic band structures and DOS. The filling of the conduction band as lithium-ions are intercalated into this systems was

revealed by a shift in Fermi level towards the conduction band. In consideration of the reported magnetism of $LiMn_2O_4$, spin polarised electronic band structure and DOS calculations were also performed. A slight difference in the magnetic and non-magnetic electronic structure of this material was observed, with the magnetic Mn_2O_4 spinel showing a bandgap of ~0.65 eV. However, as lithium atoms are intercalated into this material, an overlap of the valence band and the conduction band is noted implying improvement in conduction of this material as the discharge process proceeds. Moreover, spin-up and spin-down electronic band structure and DOS calculations further elucidate on the conductivity of this material by further suggesting that the spin-up valence electrons are responsible for electric conduction. The non-magnetic spinel $Li_xMn_2O_4$ ($1 \leq x \leq 2$) as a function of lithium concentration exhibits good conductive properties (electrochemical properties) than the magnetic structure. The magnetic spinel structure shows good conductive properties at $Li_{1.0}Mn_2O_4$ and $Li_2Mn_2O_4$ concentrations which suggest that cycling (charging/discharging) between these concentrations will yield good electrochemical performance. Furthermore, the investigation of the structural changes as a function of lithium concentration was further carried out by performing atomistic simulations of the promising Li-Mn-O layered-spinel composite nanoarchitectures. Whereby, Li-Mn-O layered-spinel composite nanoarchitectures at different lithium concentration ($1 \leq x \leq 2$) were generated using the simulated amorphisation and recrystallisation, wherein, the success of this technique was confirmed by RDF graphs and atomic snapshots. The simulated synthesis technique was able to capture essential microstructural features which are observed experimentally and are key to performance of lithium-ion batteries. Consequently, enabling atomic-level analysis of the discharge process which is quite a challenge experimentally.

XRD patterns and atomic level snapshots were employed to characterise the formed components in the generated Li-Mn-O spinel nanoarchitectures, which confirmed the co-existence of the layered and spinel components in these nanoarchitectures. The discharge process as depicted by the generated nanoarchitectures at different concentrations was monitored and the structural changes that occur as the process proceeds were also noted. The calculated XRD patterns indicates a decrease in spinel Mn_3O_4 content with lithiation. A similar trend is also noted on the atomic snapshots. Whereby, a significant amount of spinel Mn_3O_4 ($Li_{1.1}Mn_2O_4$ and $Li_{1.3}Mn_2O_4$) is

observed, however, as the discharge process continues ($Li_{1.8}Mn_2O_4$ and $Li_{2.0}Mn_2O_4$) a considerable amount of spinel $LiMn_2O_4$ and layered Li_2MnO_3 are observed. The Mn^{2+} ions in spinel Mn_3O_4 are soluble in $LiPF_6$ salt electrolyte in the presence of residual cell water leading to capacity fading [47]. Hence, a decrease in Mn_3O_4 content due to the formation of $LiMn_2O_4$ and Li_2MnO_3 will hinder the reported structural instability caused by Mn^{2+} ions and substantially decrease the reported capacity fading due to Mn^{2+} [200, 201, 202]. A decrease in a number of vacancy defects as the discharge process proceeds was also noted alluding that lithium atoms occupy the vacant sites as the process progresses. The crystallinity also noted to increase with lithiation which results in more clear lithium diffusion channels which facilitate fast charge/discharge process suitable for large scale systems such as electric vehicles. This can be attributed to the spinel component due to its three-dimensional diffusion channels. This poses a need to tailor the amount of spinel and layered content present to achieve a high energy density and durable lithium-ion battery.

5.2 Recommendation

Future work entails investigation of average lithium intercalation voltage profiles for better insights on the electrochemical performance of the Li-Mn-O layered-spinel composite nanoarchitectures. The amount of layered and spinel content in a layered-spinel composite has significant impact on the electrochemical properties of the material.

References

[1] Maksimović M. and Forcan M., "The role of nanotechnology in revolutionizing energy sector.," *International Journal of Electrical Engineering and Computing.,* vol. 3, pp. 79-84, 2019.

[2] Petrović J. T., Mihajlović M. L., Petrović M. S., Kojić M. M., Koprivica M. R., Šoštarić T. and Filipović-Petrović L., "Fuel potential and properties of grape pomace hydrochar.," *Periodica Technologica.,* vol. 50, pp. 204-209, 2019.

[3] Alharthi Y. Z., Siddiki M. K. and Chaudhry G. M., "Renewable energy hybrid grid-connected system sensitivity analysis, integration, and system flexibility.," *International Symposium on Technology and Society.,* vol. 5, pp. 1-7, 2019.

[4] Liu C., Neale Z. G. and Cao G., "Understanding electrochemical potentials of cathode materials in rechargeable batteries.," *Materials Today.,* vol. 19, pp. 109-109, 2016.

[5] Goodenough J. B. and Kim Y., "Challenges for rechargeable Li batteries.," *Chemistry of Materials.,* vol. 22, pp. 587-587, 2009.

[6] Miyamoto K., "Atomistic analysis of electrolytes: redox potentials and electrochemical reactions in a lithium-Ion battery.," *Multiscale Simulations for Electrochemical Devices.,* vol. 1, pp. 25-25, 2020.

[7] Feng H., Chen Y. and Wang Y., "Electrochemical performance of a lithium ion battery with different nanoporous current collectors.," *Batteries.,* vol. 5, pp. 21-21, 2019.

[8] Lu L., Han X., Li J., Hua J. and Ouyang M., "A review on the key issues for lithium-ion battery management in electric vehicles.," *Journal of Power Sources.,* vol. 226, pp. 272-272, 2013.

[9] Etacheri V., Marom R., Elazari R., Salitra G. and Aurbach D., "Challenges in the development of advanced Li-ion batteries: a review.," *Energy and Environmental Science.,* vol. 4, pp. 3243-3243, 2011.

[10] Barré A., Deguilhem B., Grolleau S., Gérard M., Suard F. and Riu D., "A review on lithium-ion battery ageing mechanisms and estimations for automotive applications.," *Journal of Power Sources.,* vol. 241, pp. 680-680, 2013.

[11] Kodama T. and Sakaebe H., "Present status and future prospect for national project on lithium batteries.," *Journal of Power Sources.,* vol. 81, pp. 144-144, 1999.

[12] Berdichevsky G., Kelty K., Straubel J. B. and Toomre E., "The tesla roadster battery system.," *Tesla Motors.,* vol. 1, pp. 5-5, 2006.

[13] Eberhard M. and Tarpenning M., "The 21 st century electric car tesla motors.," *Tesla Motors.,* vol. 7, pp. 122-122, 2006.

[14] Kadam H. B. and Patil M., "Electric Car: The Future Car-A Short Review.," *Journal of Alternate Energy Sources and Technologies.,* vol. 10, pp. 28-28, 2019.

[15] Rossouw M. H., De Kock A., De Picciotto L. A., Thackeray M. M., David W. I. F. and Ibberson R. M., "Structural aspects of lithium-manganese-oxide electrodes for rechargeable lithium batteries.," *Materials Research Bulletin.,* vol. 25, pp. 173-182, 1990.

[16] Çapraz Ö. Ö., Rajput S., Bassett K. L., Gewirth A. A., White S. R. and Sottos N. R., "Controlling expansion in lithium manganese oxide composite electrodes via surface modification.," *Journal of The Electrochemical Society.,* vol. 166, pp. A2357-A2362, 2019.

[17] Simanjuntak C., Siburian R. and Marpaung H., "Properties of Mg/graphite and Mg/graphene as cathode electrode on primary cell battery.," *Heliyon.,* vol. 6, pp. 3118-3118, 2020.

[18] Xie J. D., Patra J., Rath P. C., Liu W. J., Su C. Y., Lee S. W., Tseng C. J., Gandomi Y. A. and Chang J. K., "Highly concentrated carbonate electrolyte for Li-ion batteries with lithium metal and graphite anodes.," *Journal of Power Sources.,* vol. 450, pp. 227657-227657, 2020.

[19] Liu W., Xu H., Qin H., Lv Y., Zhu G., Lei X., Lin F., Zhang Z. and Wang L., "Rapid coating of asphalt to prepare carbon-encapsulated composites of nano-silicon and graphite for lithium battery anodes.," *Journal of Materials Science.,* vol. 5, pp. 1-13, 2019.

[20] Liu J. W., Li X. H., Wang Z. X., Guo H. J., Peng W. J., Zhang Y. H. and Hu Q. Y., "Preparation and characterization of lithium hexafluorophosphate for lithium-ion battery electrolyte.," *Transactions of Nonferrous Metals Society of China.,* vol. 20, pp. 344-348, 2010.

[21] Xu K., "Nonaqueous liquid electrolytes for lithium-based rechargeable batteries.," *Chemical Reviews.,* vol. 104, pp. 4303-441, 2004.

[22] Philippe B., Hahlin M., Edström K., Gustafsson T., Siegbahn H. and Rensmo H., "Photoelectron spectroscopy for lithium battery interface studies.," *Journal of The Electrochemical Society.,* vol. 163, pp. A178-A191, 2016.

[23] Diouf B. and Pode R., "Potential of lithium-ion batteries in renewable energy.," *Renewable Energy.,* vol. 76, pp. 375-380, 2015.

[24] Poullikkas A., "A comparative overview of large-scale battery systems for electricity storage.," *Renewable and Sustainable Energy Reviews.,* vol. 27, pp. 778-788, 2013.

[25] Zou Y., Hu X., Ma H. and Li S. E., "Combined state of charge and state of health estimation over lithium-ion battery cell cycle lifespan for electric vehicles.," *Journal of Power Sources.,* vol. 273, pp. 793-803, 2015.

[26] Rahimi-Eichi H., Ojha U., Baronti F. and Chow M. Y., "Battery management system: An overview of its application in the smart grid and electric vehicles.," *IEEE Industrial Electronics Magazine.,* vol. 7, pp. 4-16, 2013.

[27] Siano P., "Demand response and smart grids-A survey.," *Renewable and Sustainable Energy Reviews.,* vol. 30, pp. 461-478, 2014.

[28] Yu X., Cecati C., Dillon T. and Simoes M. G., "The new frontier of smart grids.," *IEEE Industrial Electronics Magazine.,* vol. 5, pp. 49-63, 2011.

[29] Gao J., Xiao Y., Liu J., Liang W. and Chen C. P., "A survey of communication/networking in smart grids.," *Future Generation Computer Systems.,* vol. 28, pp. 391-404, 2012.

[30] Xu B., Qian D., Wang Z. and Meng Y. S, "Recent progress in cathode materials research for advanced lithium ion batteries.," *Materials Science and Engineering.,* vol. 73, pp. 51-65, 2012.

[31] Scrosati B., "Recent advances in lithium ion battery materials.," *Electrochimica Acta.,* vol. 45, pp. 2461-2466, 2000.

[32] Djian D., Alloin F., Martinet S., Lignier H. and Sanchez J. Y., "Lithium-ion batteries with high charge rate capacity: Influence of the porous separator.," *Journal of Power Sources.,* vol. 172, pp. 416-421, 2007.

[33] Tarascon J. M. and Guyomard D., "Li metal-free rechargeable batteries based on $Li_{1+x}Mn_2O_4$ cathodes ($0 \leq x \leq 1$) and carbon anodes.," *Journal of The Electrochemical Society.,* vol. 138, pp. 2864-2868, 1991.

[34] Xia Y., Takeshige H., Noguchi H. and Yoshio M., "Studies on an Li-Mn-O spinel system (obtained by melt-impregnation) as a cathode for 4V lithium batteries part 1. Synthesis and electrochemical behaviour of $Li_xMn_2O_4$.," *Journal of Power Sources.,* vol. 56, pp. 61-67, 1995.

[35] Singh V., Chakraborty T. and Tripathy S. K., "A review of low grade manganese ore upgradation processes.," *Mineral Processing and Extractive Metallurgy Review.,* vol. 41, pp. 417-438, 2020.

[36] Tsikos H., Beukes N. J., Moore J. M. and Harris C., "Deposition, diagenesis, and secondary enrichment of metals in the paleoproterozoic hotazel iron

formation, Kalahari manganese field, South Africa.," *Economic Geology.,* vol. 98, pp. 1449-1462, 2003.

[37] Lu Q., Chen J. G. and Xiao J. Q., "Nanostructured electrodes for high-performance pseudocapacitors.," *Angewandte Chemie International Edition.,* vol. 52, pp. 1882-1889, 2013.

[38] Islam M. S. and Fisher C. A., "Lithium and sodium battery cathode materials: computational insights into voltage, diffusion and nanostructural properties.," *Chemical Society Reviews.,* vol. 43, pp. 185-204, 2014.

[39] Nitta N., Wu F., Lee J. T. and Yushin G., "Li-ion battery materials: present and future.," *Materials Today.,* vol. 18, pp. 252-264, 2015.

[40] Ning L. J., Wu Y. P., Fang S. B., Rahm E. and Holze R., "Materials prepared for lithium ion batteries by mechanochemical methods.," *Journal of Power Sources.,* vol. 133, pp. 229-242, 2004.

[41] Wu Y. P., Wan C., Jiang C., Li J. and Li Y., "Application of sol–gel method in preparation of electrode materials of lithium ion secondary battery.," *Chin J Power Sources.,* vol. 24, pp. 112-112, 2000.

[42] Li C., Zhang H. P., Fu L. J., Liu H., Wu Y. P., Rahm E., Holze R. and Wu H. Q., "Cathode materials modified by surface coating for lithium ion batteries.," *Electrochimica Acta.,* vol. 51, pp. 3872-3883, 2006.

[43] Jarvis K. A., Deng Z., Allard L. F., Manthiram A. and Ferreira P. J., "Atomic structure of a lithium-rich layered oxide material for lithium-ion batteries: evidence of a solid solution.," *Chemistry of Materials.,* vol. 23, pp. 3614-3621, 2011.

[44] Tarascon J. M., Wang E., Shokoohi F. K., McKinnon W. R. and Colson S., "The spinel phase of $LiMn_2O_4$ as a cathode in secondary lithium cells.," *Journal of the Electrochemical Society.,* vol. 138, pp. 2859-2859, 1991.

[45] Guohua L., Ikuta H., Uchida T. and Wakihara M., "The Spinel Phases LiMyMn2-yO4 (M= Co, Cr, Ni) as the Cathode for Rechargeable Lithium Batteries.," *Journal of the Electrochemical Society.,* vol. 143, pp. 178-178, 1996.

[46] Li D., Zhang H., Wang C., Song D., Shi X. and Zhang L., "New structurally integrated layered-spinel lithium-cobalt-manganese-oxide composite cathode materials for lithium-ion batteries.," *Journal of Alloys and Compounds.,* vol. 696, pp. 276-289, 2017.

[47] Cho J., Kim T. J., Kim Y. J., and Park B., "Complete blocking of Mn^{3+} ion dissolution from a $LiMn_2O_4$ spinel intercalation compound by Co_3O_4 coating.," *Chemical Communications.,* vol. 12, pp. 1074-1074, 2001.

[48] Pistoia G., Antonini A., Rosati R. and Bellitto C., "Effect of partial Ga^{3+} substitution for Mn^{3+} in $LiMn_2O_4$ on its behaviour as a cathode for Li cells.," *Journal of Electroanalytical Chemistry.,* vol. 410, pp. 115-118, 1996.

[49] Gu M., Belharouak I., Zheng J., Wu H., Xiao J., Genc A., Amine K., Thevuthasan S., Baer D. R., Zhang J. G. and Browning N. D., "Formation of the spinel phase in the layered composite cathode used in Li-ion batteries.," *ACS Nano.,* vol. 7, pp. 760-767, 2012.

[50] Johnson C. S., Li N., Vaughey J. T., Hackney S. A. and Thackeray M. M., "Lithium–manganese oxide electrodes with layered–spinel composite structures $xLi_2MnO_3 \cdot (1-x)Li_{1+y}Mn_{2-y}O_4 (0 < x < 1, 0 \leqslant y \leqslant 0.33)$ for lithium batteries.," *Electrochemistry Communications.,* vol. 7, pp. 528-528, 2005.

[51] Lee E. S., Huq A., Chang H. Y. and Manthiram A., "High-voltage, high-energy layered-spinel composite cathodes with superior cycle life for lithium-ion batteries.," *Chemistry of Materials.,* vol. 24, pp. 600-612, 2012.

[52] Xia Y., Zhou Y. and Yoshio M., "Capacity fading on cycling of 4V Li/$LiMn_2O_4$ Cells.," *Journal of The Electrochemical Society.,* vol. 144, pp. 2593-2600, 1997.

[53] Liu W., Oh P., Liu X., Myeong S., Cho W. and Cho J., "Countering voltage decay and capacity fading of lithium-rich cathode material at 60 C by hybrid surface

protection layers.," *Advanced Energy Materials.,* vol. 5, pp. 1500274-1500274, 2015.

[54] Nayak P. K., Grinblat J., Levi M., Levi E., Kim S., Choi J. W. and Aurbach D., "Al doping for mitigating the capacity fading and voltage decay of layered Li and Mn-rich cathodes for Li-Ion batteries.," *Advanced Energy Materials.,* vol. 6, pp. 1502398-1502398, 2016.

[55] Liu T., Dai A., Lu J., Yuan Y., Xiao Y., Yu L., Li M., Gim J., Ma L., Liu J. and Zhan C., "Correlation between manganese dissolution and dynamic phase stability in spinel-based lithium-ion battery.," *Nature Communications.,* vol. 10, pp. 1-11, 2019.

[56] Liu C., Cao G., Wu Z., Hu J., Wang H. and Shao G., "Surficial structure retention mechanism for $LiNi_{0.8}Co_{0.15}Al_{0.05}O_2$ in a full gradient cathode.," *ACS Applied Materials and Interfaces.,* vol. 11, pp. 31991-31996, 2019.

[57] Long B. R., Croy J. R., Park J. S., Wen J., Miller D. J. and Thackeray M. M., " Advances in stabilizing 'layered-layered' $xLi_2MnO_3 \cdot (1-x)\ LiMO_2$ (M= Mn, Ni, Co) electrodes with a spinel component.," *Journal of The Electrochemical Society.,* vol. 161, pp. A2160-A2167, 2014.

[58] Kim D., Sandi G., Croy J. R., Gallagher K. G., Kang S. H., Lee E., Slater M. D., Johnson C. S. and Thackeray M. M, "Composite 'layered-layered-spinel'cathode structures for lithium-ion batteries.," *Journal of The Electrochemical Society.,* vol. 160, pp. A31-A31, 2012.

[59] Su H., Jing L., Shi K., Yao C. and Fu H., "Synthesis of large surface area $LaFeO_3$ nanoparticles by SBA-16 template method as high active visible photocatalysts.," *Journal of Nanoparticle Research.,* vol. 12, pp. 967-974, 2010.

[60] Chane-Ching J. Y., Cobo F., Aubert D., Harvey H. G., Airiau M. and Corma A., "A general method for the synthesis of nanostructured large-surface-area materials through the self-assembly of functionalized nanoparticles.," *Chemistry-A European Journal.,* vol. 11, pp. 979-987, 2005.

[61] Kim M. G. and Cho J., "Reversible and high-capacity nanostructured electrode materials for Li-ion batteries.," *Advanced Functional Materials.,* vol. 19, pp. 1497-1514, 2009.

[62] Manthiram A. V. M. A., Murugan A. V., Sarkar A. and Muraliganth T., "Nanostructured electrode materials for electrochemical energy storage and conversion.," *Energy and Environmental Science.,* vol. 1, pp. 621-638, 2008.

[63] Chadwick A. V., "Nanotechnology: Solid progress in ion conduction.," *Nature.,* vol. 408, pp. 925-925, 2000.

[64] Ngoepe P. E, Maphanga R. R and Sayle D. C., ""Towards the nanoscale," in Computational appproaches to energy materials.," *John Wiley and Sons, Ltd.,* vol. 2, pp. 264-264, 2013.

[65] Cho J. and Kim G., "Enhancement of thermal stability of $LiCoO_2$ by $LiMn_2O_4$ coating.," *Electrochemical and Solid-State Letters.,* vol. 2, pp. 253-255, 1999.

[66] Gierszal K. P., Kim T. W., Ryoo R. and Jaroniec M., "Adsorption and structural properties of ordered mesoporous carbons synthesized by using various carbon precursors and ordered siliceous p6mm and Ia3-d mesostructures as templates.," *The Journal of Physical Chemistry B.,* vol. 109, pp. 23263-23268, 2005.

[67] Kleitz F., Choi S. H. and Ryoo R., "Cubic Ia3d large mesoporous silica: synthesis and replication to platinum nanowires, carbon nanorods and carbon nanotubes.," *Chemical Communications.,* vol. 17, pp. 2136-2137, 2003.

[68] Luo J. Y., Wang Y. G., Xiong H. M. and Xia Y. Y., "Ordered mesoporous spinel $LiMn_2O_4$ by a soft-chemical process as a cathode material for lithium-ion batteries.," *Chemistry of Materials.,* vol. 19, pp. 4791-4795, 2007.

[69] Lee Y., Kim M. G. and Cho J., "Layered $Li_{0.88}[Li_{0.18}Co_{0.33}Mn_{0.49}]O_2$ nanowires for fast and high capacity Li-ion storage material.," *Nano Letters.,* vol. 8, pp. 957-961, 2008.

[70] Huang B., Zheng X. and Lu M, "Synthesis and electrochemical properties of carbon nano-tubes modified spherical Li_2FeSiO_4 cathode material for lithium-ion batteries.," *Journal of Alloys and Compounds.,* vol. 525, pp. 110-113, 2012.

[71] Sayle D. C., Seal S., Wang Z., Mangili B. C., Price D. W., Karakoti A. S., Kuchibhatla S. V., Hao Q., Mobus G., Xu X. and Sayle T. X., "Mapping nanostructure: a systematic enumeration of nanomaterials by assembling nanobuilding blocks at crystallographic positions.," *ACS Nano.,* vol. 2, pp. 1237-1237, 2008.

[72] Sayle T. X., Caddeo F., Zhang X., Sakthivel T., Das S., Seal S., Ptasinska S. and Sayle D. C., "Structure–activity map of ceria nanoparticles, nanocubes, and mesoporous architectures.," *Chemistry of Materials.,* vol. 28, pp. 7287-7287, 2016.

[73] Sayle D. C. and Johnston R. L., "Evolutionary techniques in atomistic simulation: thin films and nanoparticles.," *Current Opinion in Solid State and Materials Science.,* vol. 7, pp. 3-12, 2003.

[74] Sayle D. C. and Watson G. W., "Structural exploration of thin-film oxide interfaces via ‘simulated amorphisation and recrystallisation'.," *Surface Science.,* vol. 473, pp. 97-107, 2001.

[75] Maphanga R. R., Sayle D. C., Sayle T. X. and Ngoepe P. E., "Amorphization and recrystallization study of lithium insertion into manganese dioxide.," *Physical Chemistry Chemical Physics.,* vol. 13, pp. 1307-1313, 2011.

[76] Grechnev G. E., Ahuja R., Johansson B. and Eriksson O., "Electronic structure, magnetic, and cohesive properties of $Li_xMn_2O_4$: Theory.," *Physical Review B.,* vol. 65, pp. 174408-174408, 2002.

[77] Chevrier V. L., Ong S. P., Armiento R., Chan M. K. and Ceder G., "Hybrid density functional calculations of redox potentials and formation energies of transition metal compounds.," *Physical Review B.,* vol. 82, pp. 751-751, 2010.

[78] Nakao Y., Ozawa K., Fujii H., Mochiku T., Iwai H., Tsuchiya Y. and Igawa N., "Electrode Properties of Li_2MnO_3 (C2/m) for a Lithium-Battery Cathode in

Several Charge-Discharge Potential Ranges.," *Transactions of the Materials Research Society of Japan.,* vol. 38, pp. 229-233, 2013.

[79] Boulineau A., Croguennec L., Delmas C. and Weill F., "Structure of Li_2MnO_3 with different degrees of defects.," *Solid State Ionics.,* vol. 180, pp. 1652-1659, 2010.

[80] Liu W., Kowal K. and Farrington G. C., "Mechanism of the electrochemical Insertion of Lithium into $LiMn_2O_4$ Spinels.," *Journal of The Electrochemical Society.,* vol. 145, pp. 459-465, 1998.

[81] Liu Z., Wang H., Fang L., Lee J. Y. and Gan L. M., "Improving the high-temperature performance of $LiMn_2O_4$ spinel by micro-emulsion coating of $LiCoO_2$.," *Journal of Power Sources.,* vol. 104, pp. 101-107, 2002.

[82] Strobel P. and Lambert-Andron B, "Crystallographic and magnetic structure of Li_2MnO_3.," *Journal of Solid State Chemistry.,* vol. 75, pp. 90-98, 1988.

[83] Boulineau A., Croguennec L., Delmas C. and Weill F., "Reinvestigation of Li_2MnO_3 structure: electron diffraction and high resolution TEM.," *Chemistry of Materials.,* vol. 21, pp. 4216-4222, 2009.

[84] Amalraj S. F., Markovsky B., Sharon D., Talianker M., Zinigrad E., Persky R., Haik O., Grinblat J., Lampert J., Schulz-Dobrick M. and Garsuch A., "Study of the electrochemical behavior of the “inactive” Li_2MnO_3.," *Electrochimica Acta.,* vol. 78, pp. 32-39, 2012.

[85] Yong-Chang C., Miao H., Yang L., Tong C., Cheng-Cai L., Qiang L., Zhao-Lin S. and Li-Juan S., "Structural, electrical, and lithium Ion dynamics of Li_2MnO_3 from density functional theory.," *Chinese Physics Letters.,* vol. 32, pp. 17102-17102, 2015.

[86] Kodama K., Igawa N., Shamoto S. I., Ikeda K., Oshita H., Kaneko N., Otomo T. and Suzuya K., "Local lattice distortion caused by short range charge ordering in $LiMn_2O_4$.," *Journal of the Physical Society of Japan.,* vol. 82, pp. 94601-94601, 2013.

[87] Kubota K., Kaneko T., Hirayama M., Yonemura M., Imanari Y., Nakane K. and Kanno R., "Direct synthesis of oxygen-deficient Li_2MnO_{3-x} for high capacity lithium battery electrodes.," *Journal of Power Sources.,* vol. 216, pp. 249-255, 2012.

[88] Scrosati B., Hassoun J. and Sun Y. K., "Lithium-ion batteries. A look into the future.," *Energy and Environmental Science.,* vol. 4, pp. 3287-3295, 2011.

[89] Dillon S. J. and Sun K., "Microstructural design considerations for Li-ion battery systems.," *Current Opinion in Solid State and Materials Science.,* vol. 16, pp. 153-162, 2012.

[90] Muto S., Sasano Y., Tatsumi K., Sasaki T., Horibuchi K., Takeuchi Y. and Ukyo Y., "Capacity-fading mechanisms of $LiNiO_2$-based lithium-ion batteries II. Diagnostic analysis by electron microscopy and spectroscopy.," *Journal of The Electrochemical Society.,* vol. 156, pp. A371-A377, 2009.

[91] Shim J., Kostecki R., Richardson T., Song X. and Striebel K. A., "Electrochemical analysis for cycle performance and capacity fading of a lithium-ion battery cycled at elevated temperature.," *Journal of Power Sources.,* vol. 112, pp. 222-230, 2002.

[92] Kim J. H., Pieczonka N. P., Li Z., Wu Y., Harris S. and Powell B. R., "Understanding the capacity fading mechanism in $LiNi_{0.5}Mn_{1.5}O_4$/graphite Li-ion batteries.," *Electrochimica Acta.,* vol. 1, pp. 556-562, 2013.

[93] Ammundsen B. and Paulsen J., "Novel lithium-ion cathode materials based on layered manganese oxides.," *Advanced Materials.,* vol. 13, pp. 943-956, 2001.

[94] Zuo Y., Li B., Jiang N., Chu W., Zhang H., Zou R. and Xia D., "A high-capacity O2-type li-rich cathode material with a single-layer Li_2MnO_3 superstructure.," *Advanced Materials.,* vol. 30, pp. 1707255-1707255, 2018.

[95] Hai Y., Zhang Z., Liu H., Liao L., Fan P., Wu Y., Lv G. and Mei L., "Facile controlled synthesis of spinel $LiMn_2O_4$ porous microspheres as cathode material for lithium ion batteries.," *Frontiers in Chemistry.,* vol. 7, pp. 437-437, 2019.

[96] Veena R., Dinesh J. A., Raman S., Panigrahi P. and Subramaniam N. G., "Li and Mn-rich $Li_4Mn_5O_{12}$–Li_2MnO_3 composite cathode for next generation lithium-ion batteries.," *Journal of Energy Storage.,* vol. 24, pp. 100754-100754, 2019.

[97] Rastgoo-Deylami M., Javanbakht M. and Omidvar H., "Structural and electrochemical investigation of new integrated layered-layered-spinel composite, $Li_{1.1}Mn_{0.97}Ni_{0.265}Cr_{0.1}Co_{0.065}O_3$, as cathode material for high performance lithium ion battery.," *Ionics,* vol. 4, pp. 1-17, 2019.

[98] Jiang C., Wang S., Li Y., Zhang Z. and Tang Z., "A layered-spinel lithium manganite hydrate for high-capacity and ultrafast lithium storage.," *Journal of Power Sources.,* vol. 413, pp. 441-448, 2019.

[99] Urban A., Seo D. H. and Ceder G., "Computational understanding of Li-ion batteries.," *Computational Materials.,* vol. 2, pp. 16002-16002, 2016.

[100] Parr R. G., "Density functional theory of atoms and molecules.," *In Horizons of Quantum Chemistry.,* vol. 2, pp. 5-15, 1980.

[101] Wu C. S. and Chai J. D., "Electronic properties of zigzag graphene nanoribbons studied by TAO-DFT.," *Journal of Chemical Theory and Computation.,* vol. 11, pp. 2003-2011, 2015.

[102] Zaier R., Hajaji S., Kozaki M. and Ayachi S, "DFT and TD-DFT studies on the electronic and optical properties of linear π-conjugated cyclopentadithiophene (CPDT) dimer for efficient blue OLED.," *Optical Materials.,* vol. 91, pp. 108-114, 2019.

[103] Pashangpour M., "Electronic transport properties of partially hydrogenated and fluorinated borophene, a DFT study.," *Computational Materials Science.,* vol. 168, pp. 74-80, 2019.

[104] Seenithurai S. and Chai J. D., "Electronic and hydrogen storage properties of Li-terminated linear boron chains studied by TAO-DFT.," *Scientific Reports.,* vol. 8, pp. 13538-13538, 2018.

[105] Alder B. J. and Wainwright T. E, "Studies in molecular dynamics.," *The Journal of Chemical Physics.,* vol. 31, pp. 459-466, 1959.

[106] Fermi E., Pasta J. and Ulam S., "Los alamos report la-1940," *Collected Papers,* vol. 2, pp. 977-988, 1955.

[107] Skylaris C. K., Haynes P. D., Mostofi A. A. and Payne M. C, "Introducing ONETEP: Linear-scaling density functional simulations on parallel computers.," *The Journal of Chemical Physics.,* vol. 122, pp. 084119-084119, 2005.

[108] Shi S., Gao J., Liu Y., Zhao Y., Wu Q., Ju W., Ouyang C. and Xiao R., "Multi-scale computation methods: their applications in lithium-ion battery research and development.," *Chinese Physics B.,* vol. 25, pp. 018212-018212, 2015.

[109] Hansson T., Oostenbrink C. and van Gunsteren W., "Molecular dynamics simulations.," *Current Opinion in Structural Biology.,* vol. 12, pp. 190-196, 2002.

[110] Moyal J. E., "Quantum mechanics as a statistical theory.," *Mathematical Proceedings of the Cambridge Philosophical Society.,* vol. 45, pp. 99-124, 1949.

[111] Karplus M. and Petsko G. A., "Molecular dynamics simulations in biology.," *Nature.,* vol. 347, pp. 631-639, 1990.

[112] Hohenberg P. and Kohn W., "Inhomogeneous electron gas.," *Physical Review.,* vol. 136, pp. B864-B864, 1964.

[113] Kohn W. and Sham L. J., "Self-consistent equations including exchange and correlation effects.," *Physical review,* vol. 140, pp. A1133-A1133, 1965.

[114] Yang W., "Direct calculation of electron density in density-functional theory.," *Physical Review Letters.,* vol. 66, pp. 1438-1438, 1991.

[115] Rindt C. C. M. and Gaastra-Nedea S. V., "Modeling thermochemical reactions in thermal energy storage systems.," *InAdvances in Thermal Energy Storage Systems.,* vol. 4, pp. 375-375, 2015.

[116] Becke A. D., "A new mixing of Hartree–Fock and local density-functional theories.," *The Journal of Chemical Physics.,* vol. 98, pp. 1372-1377, 1993.

[117] Mattsson A. E., Schultz P. A., DEsjarlais M. P., Mattsson T. R. and Leung K., "Designing meaningful density functional theory calculations in material science.," *Modelling and Simulation in Materials Science and Engineering.,* vol. 13, pp. 31-31, 2005.

[118] Bassett L., "Quantum mechanics with applications to nanotechnology and information science.," *Physics Today.,* vol. 67, pp. 50-50, 2014.

[119] Polo V., Gräfenstein J., Kraka E. and Cremer D., "Long-range and short-range Coulomb correlation effects as simulated by Hartree–Fock, local density approximation, and generalized gradient approximation exchange functionals.," *Theoretical Chemistry Accounts.,* vol. 109, pp. 22-35, 2003.

[120] Zupan A. and Causà M., "Density functional lcao calculations for solids: Comparison among Hartree–Fock, dft local density approximation, and dft generalized gradient approximation structural properties.," *International Journal of Quantum Chemistry.,* vol. 56, pp. 337-344, 1995.

[121] Cortona P., "New self-interaction-corrected local-density approximation to the density-functional theory.," *Physical Review A,* vol. 34, pp. 769-769, 1986.

[122] Patterson J. D., "Density-functional theory of atoms and molecules: Robert G. Parr and Weitao Yang.," *Oxford University Press, New York, and Clarendon Press, Oxford.,* vol. 1989, pp. 611-611, 1989.

[123] Perdew J. P. and Yue W., "Accurate and simple density functional for the electronic exchange energy: Generalized gradient approximation.," *Physical Review B.,* vol. 33, pp. 8800-8800, 1986.

[124] Vosko S. H., Wilk L. and Nusair M., "Accurate spin-dependent electron liquid correlation energies for local spin density calculations: a critical analysis.," *Canadian Journal of Physics.,* vol. 58, pp. 1200-1211, 1980.

[125] Kittel C., McEuen P. and McEuen P., "Introduction to solid state physics.," *New York: Wiley.,* vol. 8, pp. 105-130, 1996.

[126] Payne M. C., Teter M. P., Allan D. C., Arias T. A. and Joannopoulos J. D., "CASTEP 4.2 Academic version, licensed under the UKCP-MSI Agreement.," *Reviews of Modern Physics.,* vol. 64, pp. 1045-1045, 1992.

[127] Rappe A. M., Rabe K. M., Kaxiras E. and Joannopoulos J. D., "Optimized pseudopotentials.," *Physical Review B.,* vol. 41, pp. 1227-1227, 1990.

[128] Chadi D. J. and Cohen M. L., "Special points in the Brillouin zone.," *Physical Review B.,* vol. 8, pp. 5747-5747, 1973.

[129] Hamann D. R., Schlüter M. and Chiang C., "Norm-conserving pseudopotentials.," *Physical Review Letters.,* vol. 43, pp. 1494-1494, 1979.

[130] Hamann D. R., Schlüter M. and Chiang C., "Norm-conserving pseudopotentials.," *Physical Review Letters.,* vol. 43, pp. 1494-1494, 1979.

[131] Kleinman L. and Bylander D. M., "Efficacious form for model pseudopotentials.," *Physical Review Letters.,* vol. 48, pp. 1425-1425, 1982.

[132] Bachelet G. B., Hamann D. R. and Schlüter M., "Pseudopotentials that work: From H to Pu.," *Physical Review B.,* vol. 26, pp. 4199-4199, 1982.

[133] Vanderbilt D., "Soft self-consistent pseudopotentials in a generalized eigenvalue formalism.," *Physical Review B.,* vol. 41, pp. 7892-7892, 1990.

[134] Segall M. D., Lindan P. J., Probert M. A., Pickard C. J., Hasnip P. J., Clark S. J. and Payne M. C., "First-principles simulation: ideas, illustrations and the CASTEP code.," *Journal of Physics: Condensed Matter.,* vol. 14, pp. 2717-2717, 2002.

[135] Payne M. C., Teter M. P., Allan D. C., Arias T. A. and Joannopoulos A. J, "Iterative minimization techniques for ab initio total-energy calculations: molecular dynamics and conjugate gradients.," *Reviews of Modern Physics.,* vol. 64, pp. 1045-1045, 1992.

[136] Zhang H. and Banfield J. F., "Aggregation, coarsening, and phase transformation in ZnS nanoparticles studied by molecular dynamics simulations.," *Nano Letters.,* vol. 4, pp. 718-718, 2004.

[137] Verlet L., "Computer" experiments" on classical fluids. I. thermodynamical properties of lennard-Jones molecules.," *Physical Review.,* vol. 159, pp. 98-98, 1967.

[138] Berhanu W. M. and Masunov A. E., "The atomic level interaction of polyphenols with the Aβ oligomer aggregate, a molecular dynamic guidance for rational drug design.," *In Polyphenols in Human Health and Disease.,* vol. 2, pp. 59-59, 2014.

[139] Pitman M. R. and Menz R. I., "Methods for protein homology modelling.," *In Applied Mycology and Biotechnology.,* vol. 6, pp. 37-37, 2006.

[140] Case D. A., Cheatham III T. E., Darden T., Gohlke H., Luo R., Merz Jr K. M., Onufriev A., Simmerling C., Wang B. and Woods R. J., "The amber biomolecular simulation programs.," *Journal of Computational Chemistry.,* vol. 26, pp. 1668-1668, 2005.

[141] MacKerell Jr A. D., Bashford D., Bellott M. L. D. R., Dunbrack Jr R. L., Evanseck J. D., Field M. J., Fischer S., Gao J., Guo H., Ha S. and Joseph-McCarthy D., "All-atom empirical potential for molecular modeling and dynamics studies of proteins.," *The Journal of Physical Chemistry B.,* vol. 102, pp. 3586-3586, 1998.

[142] Christen M., Hünenberger P. H., Bakowies D., Baron R., Bürgi R., Geerke D. P., Heinz T. N., Kastenholz M. A., Kräutler V., Oostenbrink C. and Peter C., "The GROMOS software for biomolecular simulation: GROMOS05.," *Journal of Computational Chemistry.,* vol. 26, pp. 1719-1719, 2005.

[143] Binard M., Donnay J. P. and Nadasdi I., "Transcription des usages du sol par le modèle de potentiel," *Mappemonde,* vol. 7, pp. 27-27, 3.

[144] Weber C. and Hirsch J., "Potential model application and planning issues.," *Cybergeo: European Journal of Geography.,* vol. 7, pp. 44-44, 2000.

[145] Buckingham R. A., "The classical equation of state of gaseous helium, neon and argon.," *Proceedings of the Royal Society of London.,* vol. 168, pp. 264-283, 1938.

[146] Reines F. and Sobel H. W., "Test of the Pauli exclusion principle for atomic electrons.," *Physical Review Letters.,* vol. 32, pp. 954-954, 1974.

[147] Smith W., and Todorov T. I., "A short description of DL_POLY.," *Molecular Simulation.,* vol. 32, pp. 943-943, 2006.

[148] Born M., "Quantum mechanics of the collision processes.," *Journal of Physics.,* vol. 38, pp. 803-827, 1926.

[149] Khanna R. and Sahajwalla V., "Atomistic simulations of properties and phenomena at high temperatures.," *In Treatise on Process Metallurgy.,* vol. 3, pp. 287-287, 2014.

[150] Sayle D. C, "The predicted 3-D atomistic structure of an interfacial screw-edge dislocation.," *Journal of Materials Chemistry.,* vol. 3, pp. 2961-2961, 1999.

[151] Cao Q., Gunawan O., Copel M., Reuter K. B., Chey S. J., Deline V. R. and Mitzi D. B., "Defects in Cu (In, Ga) Se_2 chalcopyrite semiconductors: a comparative study of material properties, defect states, and photovoltaic performance.," *Advanced Energy Materials.,* vol. 1, pp. 845-853, 2011.

[152] Dominguez J. E., Fu L. and Pan X. Q., "Effect of crystal defects on the electrical properties in epitaxial tin dioxide thin films.," *Applied Physics Letters.,* vol. 81, pp. 5168-5170, 2002.

[153] Burt H. M. and Mitchell A. G., "Crystal defects and dissolution.," *International Journal of Pharmaceutics.,* vol. 9, pp. 137-152, 1981.

[154] Casey W. H., Carr M. J. and Graham R. A., "Crystal defects and the dissolution kinetics of rutile.," *Geochimica et Cosmochimica Acta.,* vol. 52, pp. 1545-1556, 1998.

[155] Rashid M. S., Kim C., Ryntz E. F., Saunders F. I., Verma R. and Kim S., "Quick plastic forming of aluminum alloy sheet metal.," *United States Patent US.,* vol. 253, pp. 588-588, 2001.

[156] Krajewski P. E. and Schroth J. G, "Overview of quick plastic forming technology.," *Materials Science Forum.,* vol. 551, pp. 12-12, 2007.

[157] Mouritz A. P., Introduction to aerospace materials, Elsevier, 2012.

[158] De Rosa C. and Auriemma F., "The deformability of polymers: the role of disordered mesomorphic crystals and stress-induced phase transformations.," *Angewandte Chemie International Edition.,* vol. 51, pp. 1207-1211, 2012.

[159] Kröner E., "The differential geometry of elementary point and line defects in Bravais crystals.," *International Journal of Theoretical Physics.,* vol. 29, pp. 1219-1237, 1990.

[160] Yan Q., Zhou Z., Zhao X. S. and Chua S. J., "Line defects embedded in three-dimensional photonic crystals.," *Advanced Materials.,* vol. 17, pp. 1917-1920, 2005.

[161] Van Swygenhoven H., "Grain boundaries and dislocations.," *Science.,* vol. 296, pp. 66-67, 2002.

[162] Read W. T. and Shockley W., "Dislocation models of crystal grain boundaries.," *Physical Review.,* vol. 78, pp. 275-275, 1950.

[163] Brandon D. G., "The structure of high-angle grain boundaries.," *Acta metallurgica.,* vol. 14, pp. 1479-1484, 1966.

[164] Gurevich A. and Pashitskii E. A., "Current transport through low-angle grain boundaries in high-temperature superconductors.," *Physical Review B.,* vol. 57, pp. 13878-13878, 1998.

[165] Yarnell J. L., Katz M. J., Wenzel R. G. and Koenig S. H., "Structure factor and radial distribution function for liquid argon at 85 K.," *Physical Review A.,* vol. 7, pp. 2130-2130, 1973.

[166] Li F. and Lannin J. S., "Radial distribution function of amorphous carbon.," *Physical Review Letters.,* vol. 65, pp. 1905-1905, 1990.

[167] Giessen B. C. and Gordon G. E., "X-ray diffraction: new high-speed technique based on X-ray spectrography.," *Science.,* vol. 159, pp. 973-975, 1968.

[168] Chatterjee A. K., "X-ray Diffraction.," *Handbook of Analytical Techniques in Concrete Science and Technology.,* vol. 1, pp. 275-332, 2001.

[169] Holzwarth U. and Gibson N., "The Scherrer equation versus the'Debye-Scherrer equation'.," *Nature Nanotechnology.,* vol. 6, pp. 534-534, 2011.

[170] Park Y. J., Kim J. G., Kim M. K., Kim H. G., Chung H. T. and Park Y., "Electrochemical properties of $LiMn_2O_4$ thin films: suggestion of factors for excellent rechargeability.," *Journal of Power Sources.,* vol. 87, pp. 69-77, 2000.

[171] Zhu J., Zeng K. and Lu L., "Cycling effects on surface morphology, nanomechanical and interfacial reliability of $LiMn_2O_4$ cathode in thin film lithium ion batteries.," *Electrochimica acta.,* vol. 68, pp. 52-59, 2012.

[172] Kuriyama K., Onoue A., Yuasa Y. and Kushida K., "Atomic force microscopy study of surface morphology change in spinel $LiMn_2O_4$: possibility of direct observation of Jahn–Teller instability.," *Surface Science.,* vol. 601, pp. 2256-2259, 2007.

[173] Hunter J. C., "Preparation of a new crystal form of manganese dioxide: λ-MnO_2.," *Journal of Solid State Chemistry.,* vol. 39, pp. 142-142, 1981.

[174] Strobel P., Le Cras F. and Anne M., "Composition-valence diagrams: A new representation of topotactic reactions in ternary transition metal oxide systems. Application to lithium intercalation.," *Journal of Solid State Chemistry.,* vol. 124, pp. 83-94, 1996.

[175] David W. I . F., Thackeray M. M., De Picciotto L. A. and Goodenough J. B., "Structure refinement of the spinel-related phases $Li_2Mn_2O_4$ and $Li_{0.2}Mn_2O_4$.," *Journal of Solid State Chemistry.,* vol. 67, pp. 316-323, 1987.

[176] Dittrich G. and Hoppe R., "The crystal structure of $LiMnO_2$.," *Journal of Inorganic and General Chemistry.,* vol. 368, pp. 262-270, 1969.

[177] Berg H. and Thomas J. O., "Neutron diffraction study of electrochemically delithiated $LiMn_2O_4$ spinel.," *Solid State Ionics.,* vol. 126, pp. 227-234, 1999.

[178] Verhoeven V. W. J., De Schepper I. M., Nachtegaal G., Kentgens A. P. M., Kelder E. M., Schoonman J. and Mulder F. M., "Lithium dynamics in $LiMn_2O_4$ probed directly by two-dimensional 7LiNMR.," *Physical Review Letters.,* vol. 86, pp. 4314-4314, 2001.

[179] Perdew J. P., Burke K. and Ernzerhof M., "Generalized gradient approximation made simple.," *Physical Review Letters.,* vol. 77, pp. 3865-3865, 1996.

[180] Fang C. M. and De Wijs G. A., "Local structure and chemical bonding of protonated $Li_xMn_2O_4$ spinels from first principles.," *Chemistry of Materials.,* vol. 18, pp. 116-116, 2006.

[181] Monge M. Á., Amarilla J. M., Gutiérrez-Puebla E., Campa J. A. and Rasines I., "Atomic level study of $LiMn_2O_4$ as electrode in lithium batteries.," *ChemPhysChem.,* vol. 3, pp. 367-367, 2002.

[182] Rousse G., Masquelier C., Rodriguez-Carvajal J., Elkaim E., Lauriat J. P. and Martinez J. L., "X-ray study of the spinel $LiMn_2O_4$ at low temperatures.," *Chemistry of Materials.,* vol. 11, pp. 3629-3629, 1999.

[183] Akimoto J., Takahashi Y., Gotoh Y. and Mizuta S., "Single crystal growth of the spinel-type $LiMn_2O_4$.," *Journal of Crystal Growth.,* vol. 229, pp. 405-405, 2001.

[184] Mishra S. K. and Ceder G., "Structural stability of lithium manganese oxides.," *Physical Review B.,* vol. 59, pp. 6120-6120, 1999.

[185] Yoo K. S., Cho N. W. and Oh Y. J., "Structural and electrical characterization of Li $(Mn_{1-\delta}Ti_\delta)_2O_4$ electrode materials.," *Solid State Ionics.,* vol. 113, pp. 43-43, 1998.

[186] Berg H., Göransson K., Noläng B. and Thomas J. O., "Electronic structure and stability of the $Li_xMn_2O_4$ (0 < x < 2) system.," *Journal of Materials Chemistry.,* vol. 9, pp. 2813-2813, 1999.

[187] Ouyang C. Y., Shi S. Q. and Lei M. S., "Jahn–Teller distortion and electronic structure of $LiMn_2O_4$.," *Journal of Alloys and Compounds.,* vol. 474, pp. 370-370, 2009.

[188] Xu B. and Meng S., "Factors affecting Li mobility in spinel $LiMn_2O_{4-A}$ first-principles study by GGA and GGA+U methods.," *Journal of Power Sources.,* vol. 195, pp. 4971-4971, 2010.

[189] Smith W. and Forester T. R., "DL_POLY_2. 0: A general-purpose parallel molecular dynamics simulation package.," *Journal of Molecular Graphics.,* vol. 14, pp. 136-141, 1996.

[190] Born M. and Huang K., "Dynamical theory of crystal lattices.," *Clarendon Press.,* vol. 5, pp. 32-32, 1954.

[191] Kellerman D. G. and Gorshkov V. S., "Structure, properties, and application of lithium–manganese spinels.," *Russian Journal of Electrochemistry.,* vol. 37, pp. 1227-1227, 2001.

[192] Christensen J. M., Deiana D., Grunwaldt J. D. and Jensen A. D., "Ceria prepared by flame spray pyrolysis as an efficient catalyst for oxidation of diesel soot.," *Catalysis Letters.,* vol. 144, pp. 1661-1661, 2014.

[193] Li S., Ren Y., Biswas P. and Stephen D. T., "Flame aerosol synthesis of nanostructured materials and functional devices: Processing, modeling, and diagnostics.," *Progress in Energy and Combustion Science.,* vol. 55, pp. 59-59, 2016.

[194] Sadeghi B., Sarraf-Mamoory R. and Shahverdi H. R., "Surface modification of $LiMn_2O_4$ for lithium batteries by nanostructured $LiFePO_4$ phosphate.," *Journal of Nanomaterials.,* vol. 2012, pp. 130-130, 2012.

[195] Gao Y., Ma J., Wang X., Lu X., Bai Y., Wang Z. and Chen L., "Improved electron/Li-ion transport and oxygen stability of Mo-doped Li_2MnO_3.," *Journal of Materials Chemistry A.,* vol. 2, pp. 4811-4811, 2014.

[196] Ullah A. A., Kibria A. F., Akter M., Khan M. N. I., Tareq A. R. M. and Firoz S. H., "Oxidative degradation of methylene blue using Mn_3O_4 nanoparticles," *Water Conservation Science and Engineering.,* vol. 1, pp. 249-256, 2017.

[197] Oikawa K., Kamiyama T., Izumi F., Chakoumakos B. C., Ikuta H., Wakihara M., Li J. and Matsui Y., "Structural phase transition of the spinel-type oxide $LiMn_2O_4$.," *Solid State Ionics.,* vol. 109, pp. 35-41, 1998.

[198] Masquelier C., Tabuchi M., Ado K., Kanno R., Kobayashi Y., Maki Y., Nakamura O. and Goodenough J. B., "Chemical and magnetic characterization of spinel materials in the $LiMn_2O_4$-$Li_2Mn_4O_9$–$Li_4Mn_5O_{12}$ System.," *Journal of Solid State Chemistry.,* vol. 123, pp. 255-266, 1996.

[199] Tsai Y. W., Santhanam R., Hwang B. J., Hu S. K. and Sheu H. S., "Structure stabilization of $LiMn_2O_4$ cathode material by bimetal dopants.," *Journal of Power Sources.,* vol. 119, pp. 701-705, 2003.

[200] Gummow R. J., De Kock A. and Thackeray M. M., "Improved capacity retention in rechargeable 4V lithium/lithium-manganese oxide (spinel) cells.," *Solid State Ionics.,* vol. 69, pp. 59-67, 1994.

[201] Uchiyama T., Nishizawa M., Itoh T. and Uchida I., "Electrochemical quartz crystal microbalance investigations of $LiMn_2O_4$ thin films at elevated temperatures.," *Journal of The Electrochemical Society.,* vol. 147, pp. 2057-2060, 2000.

[202] Komaba S., Kumagai N., Sasaki T. and Miki Y., "Manganese dissolution from lithium doped Li-Mn-O spinel cathode materials into electrolyte solution.," *Electrochemistry.,* vol. 69, pp. 784-787, 2001.

APPENDIX A

PUBLICATIONS AND CONFERENCE PRESENTATIONS

Presentations

1. **Hlungwani D**, Ledwaba R.S and Ngoepe P.E, Computer simulation of layered-spinel composite materials (ORAL), Faculty of Science and Agriculture Research day, Fusion Boutique, Polokwane, 2018.
2. **Hlungwani D**, Ledwaba R.S and Ngoepe P.E, Investigation of operating voltage during electrochemical lithiation of $Li_xMn_2O_4$ ($1 \leq x \leq 2$) cathode material (POSTER), Centre for High Performance Computing (CHPC) Conference, Century City Hotel, Cape Town, 2018.
3. **Hlungwani D**, Ledwaba R.S and Ngoepe P.E, Simulated synthesis of Li-intercalated layered (Li_2MnO_3)-spinel ($LiMn_2O_4$) composite nanoarchitectures, South African Institute of Physics (SAIP) Conference (ORAL), Protea Hotel The Ranch Resort, Polokwane, 2019.
4. **Hlungwani D**, Ledwaba R.S and Ngoepe P.E, Probing the discharge process of a lithium-ion battery via the simulated synthesis of Li-Mn-O layered-spinel composite nanoarchitectures (ORAL), Protea Hotel The Ranch Resort, Polokwane, 2019.
5. **Hlungwani D**, Ledwaba R.S and Ngoepe P.E, First principles study on the effect of lithiation on the spinel $Li_xMn_2O_4$ structure using CASTEP and ONETEP codes, Centre for High Performance Computing (CHPC) Conference, Birchwood Hotel, Johannesburg, 2019.

Publications

1. Hlungwani D, Ledwaba R.S. and Ngoepe P.E, Computational Modelling Studies of Structural Transition in $LiMn_2O_4$ ($1 \leq x \leq 2$) Nanoparticles, The Electrochemical Society